



HAL
open science

Synthèse et caractérisation de différentes nanoparticules up-conversion à base de fluorures cubiques dopées Yb/Er dans le NIR au VIS

Zhenyu Yang

► **To cite this version:**

Zhenyu Yang. Synthèse et caractérisation de différentes nanoparticules up-conversion à base de fluorures cubiques dopées Yb/Er dans le NIR au VIS. Matériaux. Université Paris sciences et lettres, 2019. Français. NNT : 2019PSLECO31 . tel-03200594

HAL Id: tel-03200594

<https://pastel.hal.science/tel-03200594>

Submitted on 16 Apr 2021

HAL is a multi-disciplinary open access archive for the deposit and dissemination of scientific research documents, whether they are published or not. The documents may come from teaching and research institutions in France or abroad, or from public or private research centers.

L'archive ouverte pluridisciplinaire **HAL**, est destinée au dépôt et à la diffusion de documents scientifiques de niveau recherche, publiés ou non, émanant des établissements d'enseignement et de recherche français ou étrangers, des laboratoires publics ou privés.

THÈSE DE DOCTORAT

DE L'UNIVERSITÉ PSL

Préparée à Chimie ParisTech

**Synthèse et Caractérisation de Différentes
Nanoparticules Up-conversion à Base de Fluorures
Cubiques Dopées Yb/Er dans le NIR au VIS**

Soutenue par

Zhenyu YANG

Le 17 décembre 2019

Ecole doctorale n° 397

**Physique et Chimie des
Matériaux**

Spécialité

Chimie Physique

Composition du jury :

Géraldine, DANTELLE
CR, INSTITUT NEEL, CNRS *Rapporteur*

Nathalie, DUPONT
PR, CSPBAT, Université Paris Nord *Rapporteur*

Souad, AMMAR
PR, ITODYS, Université Paris Diderot *Président*

Patrick, GREDIN
MCF, CNRS, ENSCP, Université PSL *Examineur*

Michel, MORTIER
DR, CNRS, ENSCP, Université PSL *Directeur de thèse*

Acknowledgement

Synthesis and characterization of Yb/Er co-doped different cubic fluoride-based NIR to VIS up-conversion nanoparticles

Acknowledgement

This work was carried out in the Institut de Recherche de Chimie Paris (IRCP), Chimie-Paristech CNRS of Paris-Sciences-et-Lettres (PSL) University, supervised by Prof. Michel Mortier and Prof. Patrick Gredin. The financial support is from the China Scholar Council (CSC).

First of all, I would like to express my deep and sincere thanks to my supervisors Prof. Michel Mortier and Prof. Patrick Gredin for their continuous guidance and help. Thanks for sharing of immense knowledge and endless help on all aspects of this work. Their encouragement helped me to pass through the hard times in process of pursuing the PhD degree.

Besides, I also want to express my sincere thanks to Prof. G eraldine Dantelle and Prof. Nathalie Dupon for reviewing the thesis and for the valuable insightful comments.

I would like to thank Karmel de Oliveira Lima for her help and advice for this thesis work. I wish to thank Prof. Gerard Aka for his care and help.

Thank Patrick Aschehoung for his help in photoluminescence spectra and luminescence lifetime characterization. I express my gratitude to Patricia Beaunier and Philippe Vermaut for their help in the measurement of transmission electron microscope (TEM). Thanks Prof. Zhuoying Chen and Dr. Hengyang Xiang from

Acknowledgement

ESPCI for their help in the measurement of the internal quantum yield.

I express my thanks to the colleagues and staffs in IRCP for the good working atmosphere. It is impressed that some of you gave me assistance in my characterization experiment.

Thank China Scholar Council for providing the founding and support in this thesis work for the whole three years.

I also want to express great thanks to my parents for their never-ending support and encouragement through the work.

Content

Acknowledgement	I
Content.....	i
Introduction.....	1
Chapter 1 State-of-the-art of up-conversion in RE-doped solids.....	5
1.1 Historical background and development of up-conversion in RE-doped solids	5
1.2 The mechanisms of up-conversion process	6
1.2.1 Excited-state absorption.....	7
1.2.2 Energy-transfer up-conversion.....	7
1.2.3 Photon avalanche	8
1.2.4 The efficiency of different mechanisms.....	9
1.3 The constitution of up-conversion nanoparticles	9
1.3.1 Host materials	10
1.3.2 Activators	15
1.3.3 Sensitizers	20
1.4 Fluoride-based up-conversion nanoparticles	21
1.5 Applications of up-conversion nanoparticles.....	23
1.5.1 Biology analytical applications.....	23
1.5.1.1 Biology assays	23
1.5.1.2 Chemical sensors	24
1.5.1.3 Biological imaging.....	24
1.5.2 Lasers	25
1.5.3 Diodes	25
1.5.4 Displays.....	26
1.5.5 Inks for security printing.....	26
1.5.6 Solar cells.....	27

Content

1.6 Conclusion	28
Chapter 2 Experimental section	31
2.1 Reagents and materials	31
2.1.1 Precursors utilising in KYF ₄ :10% Yb/5%Er UCNs.....	31
2.1.2 Precursors utilising in BiF ₃ :10% Yb/5%Er UCNs.....	31
2.1.3 Precursors utilising in K _{0.3} Bi _{0.7} F _{2.4} :10% Yb/5%Er UCNs.....	31
2.1.4 Precursors utilizing in BaYF ₅ :20% Yb/2%Er coated with BaYF ₅ UCNs.....	32
2.2 Synthesis procedure	32
2.2.1 Synthesis method of KYF ₄ :10% Yb/5%Er	32
2.2.2 Synthesis method of BiF ₃ :10% Yb/5%Er	33
2.2.3 Synthesis method of K _{0.3} Bi _{0.7} F _{2.4} :10% Yb/5%Er	34
2.2.4 Synthesis method of BaYF ₅ :20% Yb/2%Er@ BaYF ₅	35
2.3 Characterization experiment	36
Chapter 3 Results and discussion.....	41
3.1 KYF ₄ :10% Yb/5%Er.....	41
3.1.1 Structure	42
3.1.2 Morphology.....	49
3.1.3 Photoluminescence properties	52
3.1.4 Conclusion	65
3.2 BiF ₃ :10% Yb/5%Er.....	67
3.2.1 Structure	68
3.2.2 Morphology.....	78
3.2.3 Photoluminescence properties	81
3.2.4 Conclusion	90
3.3 K _{0.3} Bi _{0.7} F _{2.4} :10% Yb/5%Er	91
3.3.1 Structure	91
3.3.2 Morphology.....	98

Content

3.3.3 Photoluminescence properties	101
3.3.4 Conclusion	110
3.4 BaYF ₅ :20% Yb/2%Er coated with BaYF ₅	111
3.4.1 Structure	111
3.4.2 Morphology.....	115
3.4.3 Photoluminescence properties	118
3.4.4 Conclusion	124
Chapter 4 General conclusion and perspective of UCNs.....	125
4.1 General conclusion.....	125
4.2 Perspective of UCNs.....	127
Bibliography	129
Appendix.....	153

Content

Introduction

Up-conversion is an anti-Stokes type emission process where the doped activator ions absorb two or more photons from a low energy source to emit a high energy light.¹⁻¹⁴ It was discovered and developed by Dr. Auzel in 1966. And then, he presented the principles and application of up-conversion independently.^{8,13} A normal schematic diagram of Yb/Er co-doped NaYF₄ nanoparticle model was shown in Figure 1.¹⁵

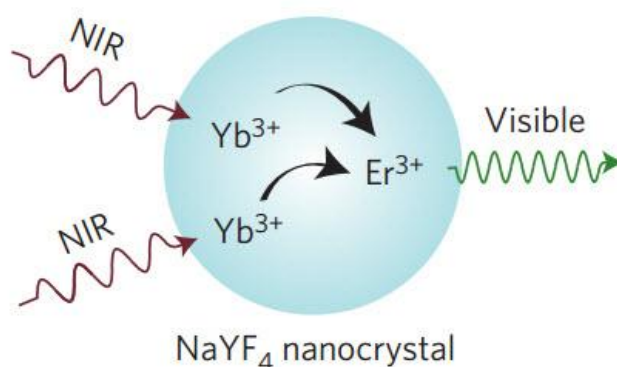


Figure 1 The schematic diagram of the up-conversion process in Yb/Er co-doped NaYF₄ nanoparticles model.¹⁵

Up-conversion nanoparticles (UCNs) have achieved considerable attentions in recent years owing to many advantages. For instance, low autofluorescence background, the absence of blinking and photobleaching, superior photostability, tunable and sharp-band emission, long lifetimes, and large anti-Stokes shifts.¹⁶⁻²¹

Among the multitude of reported host materials, the fluoride nanoparticles especially get increasing attentions mainly for their low lattice phonon energy that can reduce non-radiative losses and therefore enhance photoluminescence efficiency.²² In

Introduction

combination with its high chemical and thermal stability, it is particularly suitable for NIR to visible conversion.^{19,23}

Though many efforts have been devoted to studying up-conversion materials, it is still far from deep applications for the following several reasons. Firstly, the current widely-used synthesis approaches are cumbersome and stringent.^{4,24} The stringent conditions lead to the high cost and low repeatability. Secondly, the employ of complex frequently-used organic solvent may have potential hazards when using at high temperature.²⁰ Furthermore, the biggest obstacle of current UCNs is the quite low quantum yield. For example, 100 nm β -NaYF₄:20% Yb³⁺, 2% Er³⁺ shows $0.3 \pm 0.1\%$ internal quantum yield at 540 nm emission under 980 nm excitation with 150 W/cm² irradiance.²⁵ It is the most efficient UCNs with the optimum doping concentration of Yb and Er so far. Even so, many published works are far from efficient ones.

The first aim of this thesis is to synthesize and characterize some novel fluoride-based UCNs co-doped with Yb/Er pairs to realize the near-infrared to visible light conversion. This research can enrich the kinds of fluoride-based host materials of UCNs. Additionally, it features simple methods and environment-friendly reagents and solvents. Based on completing the first aim, the second aim is to pick some optimal UCNs from the prepared compounds, which should possess strong emission, long luminescence lifetime, and high up-conversion quantum yield. Such UCNs have potential applications in biological imaging, which needs small nanoparticles, and in solar cells, which needs a long lifetime.

This thesis was organized as follows: After an introduction, Chapter 1 summarized the development and state-of-the-art of up-conversion in RE-doped solids. The

Introduction

historical background and development of up-conversion were exhibited. The three normal classic mechanisms of ESA (excited-state absorption), ETU (energy-transfer up-conversion), and PA (Photon avalanche) were presented. The constitution of normal up-conversion materials, including host materials, activators, and sensitizers were introduced, respectively. Meanwhile, some potential applications of UCNs were given.

Chapter 2 described the details of the utilized reagents and materials, synthesis methods and experimental characterization approaches in this thesis work.

Chapter 3 made a specific discussion on the results of the four series of the prepared UCNs, including $\text{KYF}_4:\text{Yb/Er}$, $\text{BiF}_3:\text{Yb/Er}$, $\text{K}_{0.3}\text{Bi}_{0.7}\text{F}_{2.4}:\text{Yb/Er}$, and $\text{BaYF}_5:\text{Yb/Er}@\text{BaYF}_5$. The nanocrystal phase structure, calculated average crystallite size, morphology, nanoparticle size distribution, absorption spectra, internal quantum yield, emission spectra, and the decay times were analyzed and discussed. Meanwhile, the effects of nanoparticles size on photoluminescence were analyzed.

Chapter 4 gives a general conclusion about the whole work and perspective of UC.

Introduction

Chapter 1 State-of-the-art of up-conversion in RE-doped solids

1.1 Historical background and development of up-conversion in RE-doped solids

For fluorescence light emitters, rare-earth-doped solids usually follow the well-known principle of the Stokes law that simply states excitation photons are at higher energy than the emitted ones.²⁶ For example, down-conversion process is one traditional type of the Stokes emission.²⁷

Nevertheless, up-conversion is an anti-Stokes type emission process in which the emitted photons are at higher energy than the exciting ones.^{6,10-12} Actually, the anti-Stokes type emission was known to exist before the 1960s at the earliest. For instance, fluorescence anti-Stokes emission (that is so-called thermal bands), or in Raman Effect for the well-known anti-Stokes bands, or “super-excitation” which is raising an already excited electron to a still higher level but with very weak emissions. Unfortunately, the differences of emission energies above the excitation energies in these processes are not higher than about kT .

The concept of up-conversion emission started from an idea that infrared (IR) photons could be detected and counted through sequential absorption within the given ion energy levels by Bloembergen in 1959.²⁸ The initial idea started in a short proposal for an infrared quantum counter (IRQC) detector. However, it was quite difficult to realize sequential photons absorption within the same single doping ion during the limited lifetime of the first excited state.^{12,13}

Chapter 1 State-of-the-art of up-conversion on RE-doped solids

In 1966, Auzel found that the luminescence intensity of Er^{3+} , Ho^{3+} , and Tm^{3+} ions was almost enhanced by two orders of magnitude when doping Yb^{3+} into the host material under near-infrared light excitation.¹²⁻¹⁴ Until then, Auzel proposed that the energy transfer could happen between two ions and made the role of energy transfer recognized. In 1973,⁸ he presented the principles and application of up-conversion accompany with some later reviews by Mita and Nagazawa in 1974,^{29,30} by Garlick in 1976,³¹ and by Wright in 1976.³² The emitted energies are found to exceed excitation energies by 10 to 100 times kT in the up-conversion process.

1.2 The mechanisms of up-conversion process

There are many processes that could result in photons conversion from a long wavelength into the shorter ones.³³ Among them, only several mechanisms result in up-conversion process and they can be roughly classified into three classes: APTE effect (for “addition de photons par transferts d’energie”) later also named ETU for energy-transfer up-conversion,³² excited-state absorption (ESA), and photon avalanche (PA).^{33,34} They are collected and reported in several review articles.^{11,12,35} The Figure 1.1 (a), (b), and (c) shows the ESA, ETU, and PA conversion process occurring in up-conversion, respectively.

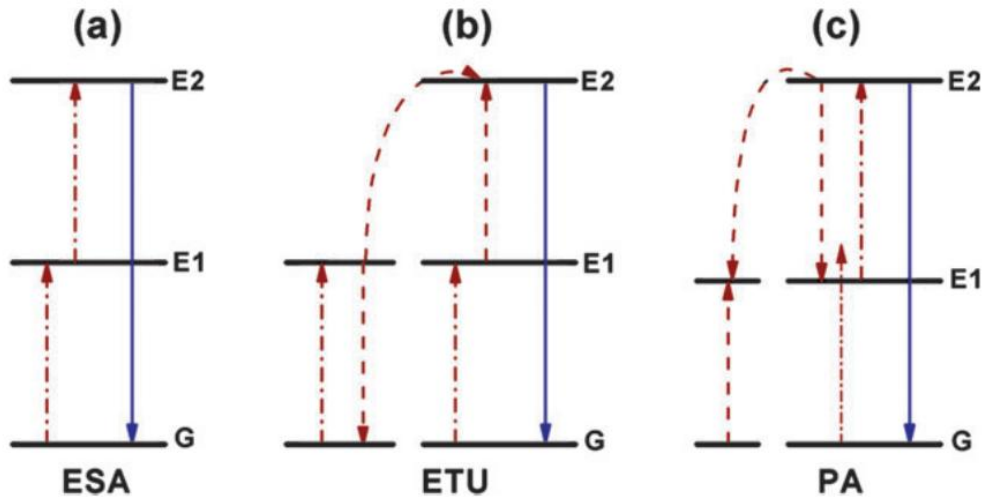


Figure 1.1 The schematic of common mechanisms in up-conversion processes: (a) excited-state absorption (ESA); (b) energy-transfer up-conversion (ETU); and (c) photon avalanche (PA).³⁵

1.2.1 Excited-state absorption

In the case of the ESA process, two pump photons from the excitation laser are successively absorbed by a single ion (Figure 1.1 (a)). Firstly, if the excitation energy is resonant with the transition energy gap value that between the level G and the first-excited metastable level E_1 , the ion populating on G level will absorb the excitation energy and populate on E_1 level. Afterward, a second absorption occurs which excites the ion from E_1 to the higher level E_2 with another pump photon absorption during the lifetime of this ion on E_1 level. Finally, the ion radiatively decays from E_2 to ground state G with up-conversion emission.

1.2.2 Energy-transfer up-conversion

The ETU process is similar to the ESA in that they all utilize successive absorption of at least two pump photons to excite the ions from the ground state to the first-excited

Chapter 1 State-of-the-art of up-conversion on RE-doped solids

state E_1 and then E_2 . The difference is the source of the second absorption photon which excites the ion from E_1 to E_2 state. In ETU, two different ions participate in the process. In this case, two neighboring ions absorb the excited photons and populate on E_1 state. Then the left ion (Figure 1.1 (b)) non-radiatively relaxes from its excited level E_1 to G state and transfers the energy to the neighboring right ion to promote it from E_1 to the higher E_2 state. The following UC process is the same as that of ESA (Figure 1.1 (a)). In this case, the doping concentration has a strong influence on the up-conversion efficiency as it determines the average distance between the neighboring doping ions.³⁵ Too high doping levels can lead to cross-relaxation between the neighboring ions, resulting in quenching of the excitation energy.

1.2.3 Photon avalanche

Photon avalanche (PA) phenomenon was first discovered in an investigation of the infrared quantum-counter (IRQC) process in Pr^{3+} doping LaCl_3 and LaBr_3 crystal by Chivan et al in 1979.³⁶ PA-induced UC features an unusual pump mechanism (Figure 1.1 (c)). It requires the intensity of the pump is above a certain threshold value. The PA process starts with populating the level E_1 by non-resonant weak ground state absorption. It is followed by resonant ESA to populate upper visible-emitting level E_2 . After that, cross-relaxation energy transfer (or ion pair relaxation) occurs between the excited ion and a neighboring ground-state ion, resulting in both ions occupying the intermediate level E_1 . Finally, the two ions populating on E_1 level are further excited to populate on E_2 level by ESA, producing strong UC emission with the avalanche process.³⁵

Chapter 1 State-of-the-art of up-conversion on RE-doped solids

1.2.4 The efficiency of different mechanisms

Up-conversion process involves the sequential absorption of two or more photons (Figure 1.1). It is especially different from the multi-photon process where the absorption of photons occurs simultaneously.

Actually, the different mechanisms in up-conversion processes have been recognized to be worked either alone or in combination.¹² Different mechanisms, ESA, ETU, and PA, result in different photoluminescence efficiency. The ESA is the least efficient up-conversion process. It requires the excited ion on E_1 level to possess enough long lifetime, which ensures the ion to absorb another photon and to be excited to populate on a higher energy state. However, it was difficult to acquire successive photons absorption for the same single doping ion during the limited lifetime of the first-excited state.^{12,13} The PA should have the highest efficiency among them. However, the PA depends on pump power and has a long response time (up to several seconds) to excitation due to numerous looping cycles of ESA and cross-relaxation process. In contrast, ETU has a quick response and be independent of the source laser. Therefore, it has been widely used to produce high efficient UC over the past decades. The up-conversion efficiency of ETU is two orders of magnitude higher than that of ESA.¹²

1.3 The constitution of up-conversion nanoparticles

The up-conversion nanoparticles are usually composed of two sets of elements: host materials which constitute the matrix, and activators which participate in the up-conversion process. The host materials provide the ambient environment and

Chapter 1 State-of-the-art of up-conversion on RE-doped solids

determine the average distance between activators in combination with doping levels.³³ The activators absorb sequential photons to stimulate from ground state to high emitting-level state and then radiatively decay to ground state.

However, in the case of Er^{3+} , Tm^{3+} , or Ho^{3+} single-doped UCNs, it is quite difficult to successively absorb another photon after the first absorption for the same ion during the limited first-excited state lifetime.²⁶ In other words, the single-doped UCNs belong to the ESA mechanism whose efficiency is very low owing to only one ion participating in completing up-conversion process. In 1966, Auzel presented that the energy transfer could occur between the two RE ions.⁸ Afterward, the status of sensitizers was noticed and he presented the ETU mechanism. The sensitizer (e.g. Yb^{3+}) is excited to populate on exciting-level by absorbing the photon and then non-radiatively relaxes back to ground state. Meanwhile, the energy is transferred to the neighboring activators ion (e.g. Er^{3+}), which populates on the first-excited state, to continue populating on a higher emitting-level state.

1.3.1 Host materials

The host materials are quite significant for the activators to generate emission light by absorbing the phonons and radiatively decaying to the ground state. It provides the ambient circumstance for the activators and sensitizers. Among the numerous groups of chemical materials, many of them are all found to have the up-conversion phenomena when doped with suitable activators, such as the frequently-used lanthanide (Ln) ions (Table 1.1). Additionally, the Pr^{3+} and Ce^{3+} could also induce a luminescence up-conversion process when doping them into suitable host materials.

^{37,38} Furthermore, very few reports involved Mo^{3+} ,³⁹ Ni^{2+} ,⁴⁰ and U^{4+} ,⁴¹. However, the

Chapter 1 State-of-the-art of up-conversion on RE-doped solids

utilizing of lanthanides as activators is well-known suitable activators.

Table 1.1 Several kinds of host materials from researches of recent decades.

Materials	References
Oxides	Y_2O_3 ; ⁴²⁻⁴⁴ Gd_2O_3 ; ^{45,46} TiO_2 ; ⁴⁷⁻⁴⁹ Al_2O_3 ; ⁵⁰ ZrO_2 ; ⁵¹ $\text{PbO-Bi}_2\text{O}_3\text{-Al}_2\text{O}_3\text{-B}_2\text{O}_3$; ⁵² CaWO_4 ; ⁵³ $\text{Y}_3\text{Al}_5\text{O}_{12}$ (YAG); ^{37,54-57} $\text{Y}_3\text{Ga}_5\text{O}_{12}$ (YGG); ^{38,58}
Fluorides	NaREF_4 (RE:La-Lu); ^{12,16,18,23,39,59-63,64-68,} LiYF_4 ; ^{37,69-71} KYF_4 ; ⁷²⁻⁷⁴ KY_3F_{10} ; ⁷⁵⁻⁷⁷ YF_3 ; ^{78,79} LaF_3 ; ⁸⁰⁻⁸² CaF_2 ; ^{83,84} SrF_2 ; ^{85,86}
Chlorides	NaCl ; ^{40,87} BaCl_2 ; ^{88,89} SrCl_2 ; ⁹⁰ CaCl_2 ; ⁹¹ ThCl_4 ; ⁴¹ CsCdCl_3 ; ⁴⁰ CsCaCl_3 ; ⁹² RbMnCl_3 ; ⁹³
Bromides	ThBr_4 ; ⁴¹ CsCaBr_3 ; ⁹²
Iodides	CsCaI_3 ; ⁹² RbCaI_3 ; ⁹⁴
Oxysulfides	$\text{Y}_2\text{O}_2\text{S}$; ^{95,96} $\text{Gd}_2\text{O}_2\text{S}$; ^{97,98} $\text{La}_2\text{O}_2\text{S}$; ⁹⁹⁻¹⁰¹
Oxyfluorides	YOF ; ¹⁰²⁻¹⁰⁴ GdOF ; ^{104,105} LaOF ; ^{104,106}
Phosphates	YbPO_4 ; ¹⁰⁷⁻¹¹⁰ LuPO_4 ; ¹¹⁰⁻¹¹² LaPO_4 ; ^{113,114}

Table 1.1 gives some kinds of host materials, including oxide, fluoride, chlorides, bromides, iodides, oxysulfide, oxyfluorides, and phosphate. It indicates that many materials could be utilized as host materials. The trivalent rare-earth ions (Ln^{3+}) have similar ionic size and chemical properties. So, the inorganic compounds are ideal host materials for Ln^{3+} doping up-conversion materials.³⁵ In addition, alkaline earth ions (Ba^{2+} , Sr^{2+} , and Ca^{2+}) and some transition metal ions, such as Zr, also exhibit close ionic size with lanthanide ions.¹¹⁵ Thus, their inorganic compounds, such as SrF_2 ,

Chapter 1 State-of-the-art of up-conversion on RE-doped solids

CaF₂, ZrO₂, and CaCl₂, could also be used as host materials. Besides, rare-earth oxysulfides (e.g. Y₂O₂S, Gd₂O₂S, and La₂O₂S) have been known for a long time as excellent phosphor host materials and used in cathode ray tubes, emission displays, and X-ray luminescent screens field. The up-conversion oxysulfide phosphor has higher up-conversion efficiency when compared to the respective oxide. The enhancement in the visible up-conversion efficiency is owing to the lower phonon energy in yttrium oxysulfide when compared to yttrium oxide.

Up to now, the main attention on up-conversion materials is to get high efficiency UCNs. In terms of host materials, the most significant factor affecting the up-conversion efficiency is indeed phonon energy of the host materials. The phonon energy of host materials should be low enough compared with the gap energy between the E₁ and the G energy state of activators and sensitizers. It reduces the non-radiatively relaxation by host lattice and guarantees the doping maximize the radiative up-conversion emission.¹¹⁶

Chapter 1 State-of-the-art of up-conversion on RE-doped solids

Table 1.2 Highest lattice phonon energy of commonly used Ln³⁺ doped materials.^{11,117}

Materials	Highest Phonon Energy (cm ⁻¹)
Phosphate glass	1200
Silica glass	1100
Fluoride glass	550
Chalcogenide glass	400
LaPO ₄	1050
YAG	860
YVO ₄	600
LaF ₃	300
LaCl ₃	240

Table 1.2 exhibits the highest lattice phonon energy of some common compounds. Heavy halides like chlorides, bromides, and iodides generally exhibit low phonon energies of less than 300 cm⁻¹. However, their utilizing is limited owing to hygroscopic property. The sulfide, oxide, and phosphide have high phonon energy. In comparison, fluoride have lower phonon energy that ranges in 300 to 400 cm⁻¹.^{11,118} The usually used pump laser is ~ 980 nm pulsed laser whose energy is similar to the ²F_{5/2} - ²F_{7/2} level of Yb³⁺ around 10,000 cm⁻¹ from Figure 1.3. The host lattice, with lower phonon energy, has the smaller probability to participate in non-radiative relaxation process. Therefore, the rare-earth doped fluoride UCNs have got numerous and increasing interests in recent decades.

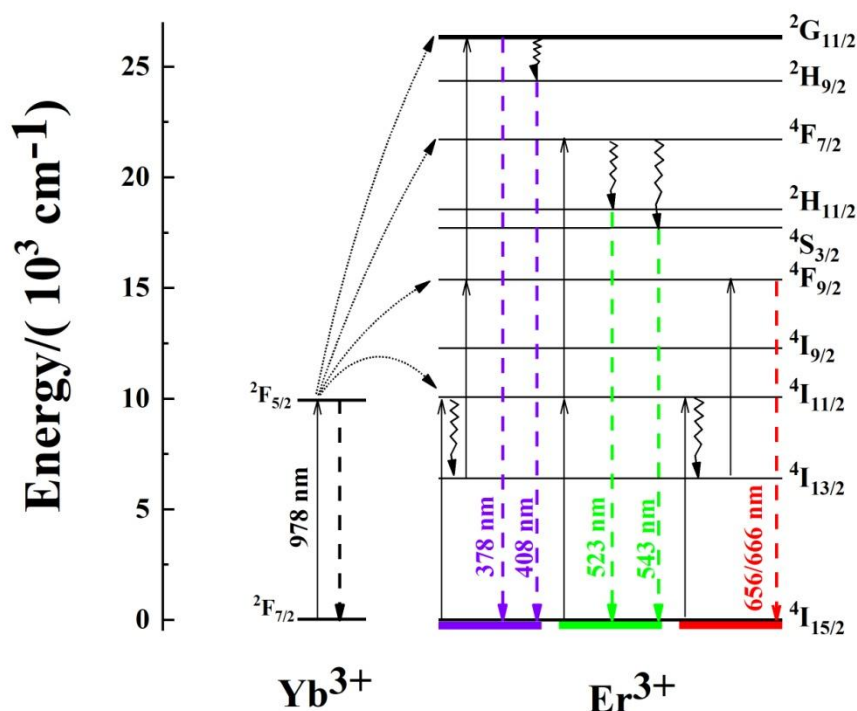


Figure 1.3 The excitation and decay ways in 4f energy levels of Yb and Er.

The current works on UCNs are done to explore novel host materials with high efficiency that mainly depends on synthesizing well-dispersed and shape-controlled nanoparticles with uniform particle size for a given host lattice. These several factors are known to favor up-conversion efficiency until now but still need more studies to be extended and perfected.^{5,10,20,119}

In addition, crystal structure exhibits significant influences on the photoluminescence properties. For example, the most efficient UCNs, Yb/Er co-doped hexagonal NaYF₄, exhibits about one order of magnitude enhancement of up-conversion efficiency compared with cubic counterparts.^{120,121} It demonstrates that the crystal structure of the phase is also a significant fact.^{3,23,65,121–123} The variation of

Chapter 1 State-of-the-art of up-conversion on RE-doped solids

the crystal structure in the host materials can significantly affect the optical properties of the nanocrystals. The phase-dependent optical property can be ascribed directly to the different crystal fields around the trivalent lanthanide ions in matrices of various symmetries. Low symmetry hosts typically exert a crystal field containing more uneven components around the doped ions compared to the high symmetry counterparts. The uneven components enhance the electronic coupling between the 4f energy levels and higher electronic configuration and subsequently increase f–f transition probabilities of the doping ions. In addition, the decrease in the cation size (or unit-cell volume) of the host can result in an increase in the crystal field strength around the doping ions and lead to the enhanced up-conversion efficiency.³⁴

Besides, the shape and size of nanoparticles also show great impacts on the photoluminescence efficiency. In this case, the important factor is the quenching ways from some high-frequency ligands onto the surface of the particles, such as NO_3^- , OH^- , CH_3 , and so on. These high-frequency modes of ligands onto the nanocrystal surface could activate many non-radiative channels to decrease the UC efficiency.² Sphere nanoparticles have smaller surface-to-volume ratios than nanoparticles with random morphology. Large size particles have smaller surface-to-volume ratios in comparison to small size. The smaller surface-to-volume ratios could result in fewer ligands onto the surface, that subsequently reduce the probability of the non-radiative relaxation to enhance the UC efficiency.

1.3.2 Activators

The activators are the key factor in the whole up-conversion process. They determine the choice of the excitation laser, the emission spectra, and the photoluminescence

Chapter 1 State-of-the-art of up-conversion on RE-doped solids

lifetime in combination with host materials. The activators, used in up-conversion nanoparticles, are mostly Ln^{3+} ions. In very few reports, the Pr^{3+} and Ce^{3+} were also adopted as activators when doping in suitable host materials.³⁷⁻⁴¹

However, the features of multiple energy levels distribution of lanthanide ions make them well-suited for utilizing in up-conversion (Figure 1.4). The lanthanides, starting from lanthanum to lutetium, are associated with the filling of the 4f-shell. The trivalent ions Ln^{3+} is the most stable oxidation state and main existing substance. The completely filled $5s^2$ and $5p^6$ sub-shells act as the shield of the 4f electron of Ln^{3+} . This particular electron structure leads to some important phenomenon such as sharp and narrow f-f transition bands. Moreover, the Laporte forbidden f-f transition results in low transition probabilities and substantially long-lived (up to 0.1s) excited states.³⁵ The common lanthanide ions have more than one exciting 4f energy level except for La^{3+} , Ce^{3+} , Yb^{3+} , and Lu^{3+} . (Figure 1.4)

Chapter 1 State-of-the-art of up-conversion on RE-doped solids

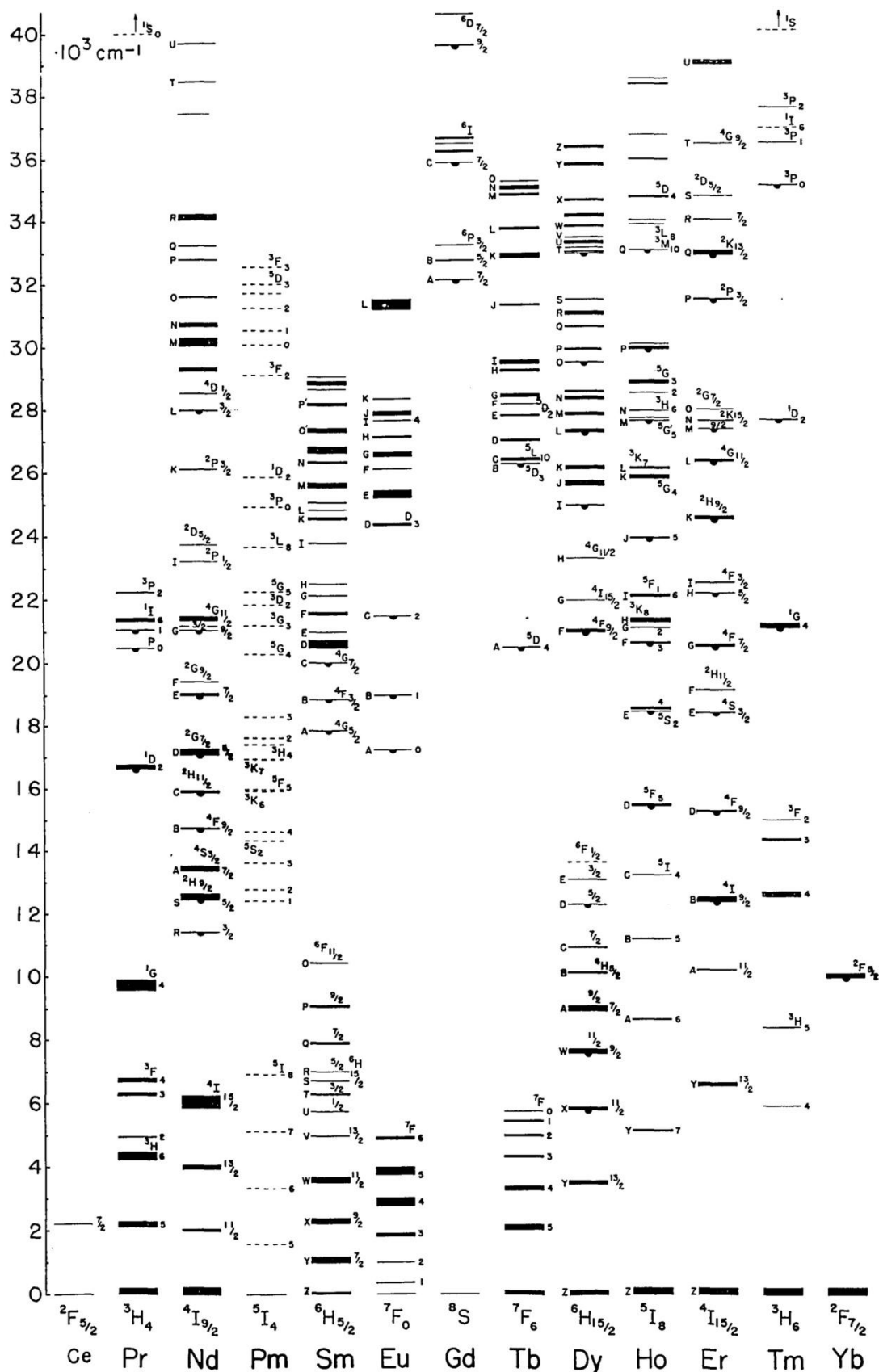


Figure 1.4 The energy levels of trivalent rare-earth ions by Dieke.¹²⁴

Chapter 1 State-of-the-art of up-conversion on RE-doped solids

As a result, most lanthanide ions could be used into up-conversion emission theoretically. Nevertheless, to generate substantively useful UC emission, the energy difference between each exciting level and its ground level should be close enough to facilitate photon absorption and energy transfer steps involved in UC processes. Concerning this requirement, only Er^{3+} , Tm^{3+} , and Ho^{3+} typically possess such ladder-like arranged energy levels (Figure 1.5). Therefore, they are frequently-used activators.

In the ETU process, the two main factors that affect the up-conversion processes are the distance between the two neighboring doped ions and the absorption cross-section of the ions.¹²⁵ Too high doping levels can lead to deleterious cross-relaxation, resulting in quenching of the excitation energy. The concentration of the activator ions should be kept low and precisely adjusted to avoid the quenching phenomenon. For up-conversion process, the internal quantum yield is limited to less than 50% owing to at least two low energy photons were absorbed to generate one high energy photon. In addition, most lanthanide activator ions exhibit low absorption cross-sections, leading to the low pump efficiency.

Another important factor is the non-radiative multi-phonon relaxation rate between the activators energy levels. This rate dictates the population of intermediate and emitting levels and subsequently determines the efficiency of the UC process. The multi-phonon relaxation rate constant k_{nr} for 4f levels of lanthanide ions^{35,86,126} is given as follows:

$$k_{nr} \propto \exp\left(-\beta \frac{\Delta E}{\hbar\omega_{max}}\right)$$

Where β is an empirical constant of the host, ΔE is the energy gap between the populated level and the next lower-lying energy level of a lanthanide ion, and $\hbar\omega_{max}$ is

Chapter 1 State-of-the-art of up-conversion on RE-doped solids

the highest-energy vibrational mode of the host lattice. The energy gap law implies that the multi-phonons relaxation rate constant decreases exponentially with increasing energy gap. As shown in Figure 1.5, Er^{3+} and Tm^{3+} have a relatively large energy gap, which means low probabilities of non-radiative transitions among various excited levels of the ions. According to this energy gap law, the known most efficient UC nanocrystals to date are acquired from Er^{3+} and Tm^{3+} activators.

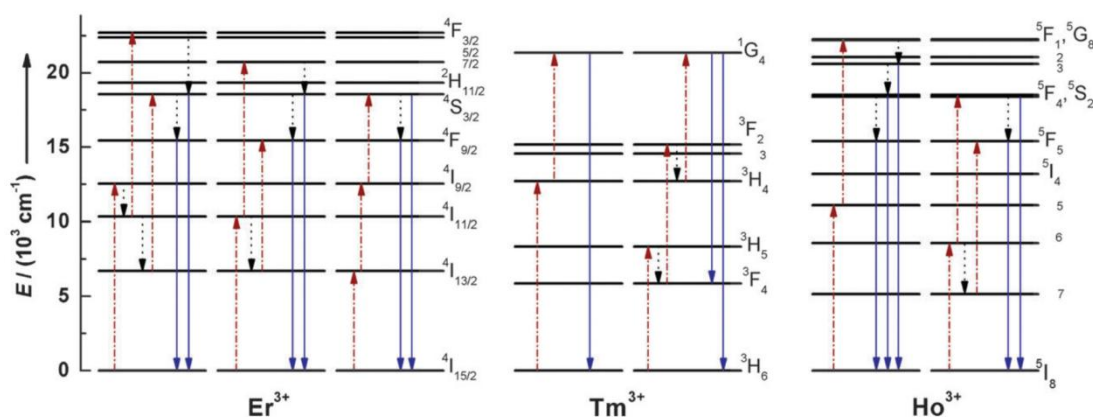


Figure 1.5 Schematic energy level diagrams of typical UC processes for Er^{3+} , Tm^{3+} , and Ho^{3+} . The dashed-dotted, dotted, and full arrows stand for excitation, multi-phonon relaxation, and emission processes, respectively.³⁵

The above lanthanide activators, Er^{3+} , Tm^{3+} , and Ho^{3+} , are always co-doped with sensitizer Yb^{3+} and excited by a ~ 980 nm pulsed laser. For example, in the case of Er^{3+} activator, the energy difference between the $^4\text{I}_{11/2}$ and $^4\text{I}_{15/2}$ levels ($\sim 10,350$ cm^{-1}) is similar to that ($\sim 10,370$ cm^{-1}) between the $^4\text{F}_{7/2}$ and $^4\text{I}_{11/2}$ levels. Therefore, the ~ 980 nm ($\sim 10,204$ cm^{-1}) was used to excite the ion which populates from $^4\text{I}_{15/2}$ to $^4\text{I}_{11/2}$ energy level and then from $^4\text{I}_{11/2}$ to $^4\text{F}_{7/2}$ level to generate green emission light. The first excited of Tm^{3+} and Ho^{3+} is corresponding to $^3\text{H}_5 \rightarrow ^3\text{H}_6$ excitation,^{63,127,128} and $^5\text{I}_6$

Chapter 1 State-of-the-art of up-conversion on RE-doped solids

→ 5I_8 excitation, respectively (Figure 1.6). The necessary energy of the first excited transition from Er^{3+} , Tm^{3+} , and 3H_6 are all close to the energy of ~ 980 nm laser.

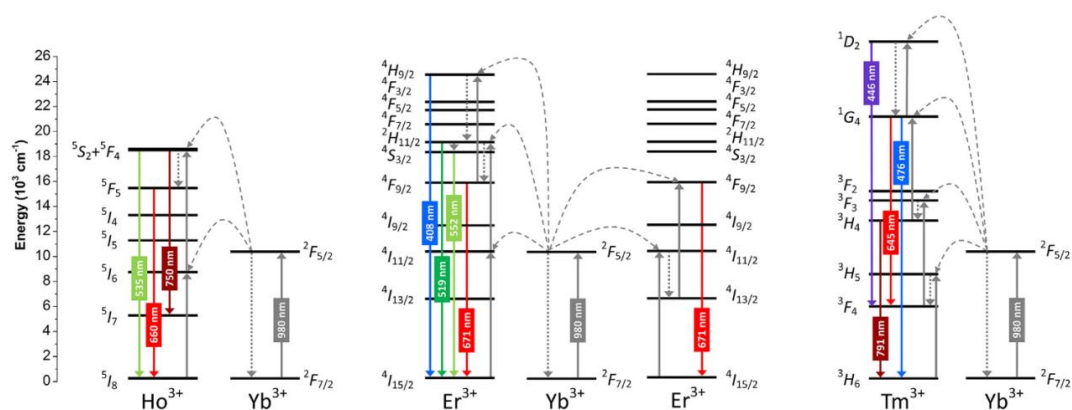


Figure 1.6 Photon energy state levels of Yb/Ho, Yb/Er and Yb/Tm.¹⁰⁵

1.3.3 Sensitizers

In lanthanide single-doped nanocrystals, such as Er^{3+} and Tm^{3+} , it is very difficult for the same ion on the first-excited level to continue absorbing the second photon to populate on a higher emitting-level in the limited lifetimes of the first-excited level. Therefore, the overall up-conversion efficiency of single-doped nanocrystals is quite low.

In 1966, Auzel found that the luminescence intensity of Er^{3+} , Ho^{3+} , and Tm^{3+} ions was almost enhanced by two orders of magnitude when doping Yb^{3+} into the host material under near-infrared light excitation.^{8,12} The Yb^{3+} was used as frequent sensitizers from then on. Yb^{3+} , with a sufficient absorption cross-section in the NIR region, is usually co-doped with the activator to take advantage of the efficient ETU process between the sensitizer and activator. Trivalent ytterbium possesses an extremely simple energy level scheme including only one 4f exciting-level of $^2F_{5/2}$.

Chapter 1 State-of-the-art of up-conversion on RE-doped solids

The absorption band of Yb^{3+} , that is located around 980 nm due to the ${}^2\text{F}_{7/2} \rightarrow {}^2\text{F}_{5/2}$ transition, has a high absorption cross-section ($11.7 \pm 1.0 \times 10^{-21} \text{ cm}^2$).¹²⁹ The absorption cross-section of Yb^{3+} at 980 nm is larger than other lanthanide ions. For example, it is one order of magnitude higher than that of the Er^{3+} . Additionally, the ${}^2\text{F}_{7/2} \rightarrow {}^2\text{F}_{5/2}$ transition of Yb^{3+} is well resonant with many f–f transitions of typical up-conversion lanthanide ions (e.g. Er^{3+} , Tm^{3+} , and Ho^{3+}), thus facilitating efficient energy transfer from Yb^{3+} to other ions. Thereby, these optical characteristics make Yb^{3+} particularly suitable as an up-conversion sensitizer.

The Dy^{3+} ion can act as a sensitizer in a $\text{YBr}_3:\text{Dy}^{3+}/\text{Er}^{3+}$ co-doped materials and $\text{BaCl}_2:\text{Dy}^{3+}/\text{Er}^{3+}$ UCNs.^{130,131} To be specific, the Dy^{3+} ion has an absorption band (${}^6\text{H}_{9/2}$) around $7,700 \text{ cm}^{-1}$ (1,300 nm) higher than the ground state (${}^6\text{H}_{15/2}$). The energy can then transfer to the ${}^4\text{F}_{9/2}$ level of Er^{3+} and finally cause a radiative transition from the ${}^4\text{F}_{9/2}$ to the ${}^4\text{I}_{15/2}$ ground level causing luminescence at around 660 nm. However, there are two energy levels (${}^6\text{H}_{11/2}$ and ${}^6\text{H}_{13/2}$) between the ground state ${}^6\text{H}_{15/2}$ and emitting-level ${}^6\text{H}_{9/2}$, which may cause the non-radiative relaxation to quench the UC process.

1.4 Fluoride-based up-conversion nanoparticles

In comparison with sulfide, oxide, and phosphide, the fluoride nanoparticles especially get considerable interest owing to the low phonon energy of fluoride which ranges in 300 to 400 cm^{-1} .^{11,118} The low lattice phonon energy of fluoride can reduce non-radiative losses and therefore enhance luminescence efficiency.²² In combination with high chemical and thermal stability and narrow emission lines, fluorides are particularly suitable for NIR conversion.

Chapter 1 State-of-the-art of up-conversion on RE-doped solids

Many kinds of fluoride-based up-conversion nanoparticles have been developed, such as NaREF₄ (RE: La-Lu),^{12,16,18,23,37,54-58,59-63} LiYF₄,^{37,69-71} KYF₄,⁷²⁻⁷⁴ KY₃F₁₀,⁷⁵⁻⁷⁷ YF₃,^{78,79} LaF₃,⁸⁰⁻⁸² CaF₂,^{83,84} and SrF₂.^{85,86} NaREF₄ type fluoride nanoparticle has got the most researches and Yb/Er co-doped hexagonal NaYF₄ is found to be the most efficient UC material up to now.^{23,61} Even so, the up-conversion nanoparticles are still far from deep application due to the low up-conversion efficiency. For example, the internal up-conversion quantum yield of the most efficient β-NaYF₄:20%Yb/2%Er nanoparticles at 540 nm is 0.3 % under a 980 nm of excitation laser according to a review paper.²⁵ At present, low efficiency is the biggest obstacle in practical applications for up-conversion phosphors.^{132,133}

Therefore, the up-conversion nanoparticles need more and deep studies to optimize the photoluminescence properties such as increasing the luminescence lifetime and enhancing the conversion efficiency. As we discussed in chapter 1.3, the suitable kinds of activators and sensitizers are always picked from the frequently used activators Er³⁺, Yb³⁺, or Ho³⁺ and sensitizers Yb³⁺. The doping concentrations of them are recommended to such as ~ 20% Yb and ~ 2% Er.³⁵ However, the kinds of the candidate host materials are numerous and various even in terms of fluoride-based materials. Therefore, more researches should be focused on synthesizing and developing more novel host materials. This may help to overcome the current limitation faced by UCNs and accelerate the development to obtain ideal host materials.

In very recent years, many novel host materials have been researched and reported. For example, NaBiF₄,²⁰ which was prepared via an ultrafast room temperature co-precipitation methods; BiF₃,^{134,135} whose host materials is economic

Chapter 1 State-of-the-art of up-conversion on RE-doped solids

non-lanthanide and “green” bismuth element; $\text{La}_{0.45}\text{Yb}_{0.50}\text{Er}_{0.05}\text{F}_3$,¹³² which developed a novel hetero-looping-enhanced-energy-transfer (hetero-LEET) up-conversion process; and BaY_2F_8 ,¹³⁶ which have been reported as a good candidate host material in crystal field with high quantum yields values. Therefore, the first goal of this thesis is to prepare several novel host materials. KYF_4 , BiF_3 , $\text{K}_{0.3}\text{Bi}_{0.7}\text{F}_{2.4}$, and BaYF_5 based up-conversion nanoparticles co-doped with Yb and Er will be synthesized in this thesis.

1.5 Applications of up-conversion nanoparticles

1.5.1 Biology analytical applications

1.5.1.1 Biology assays

Up-conversion phosphors are available to be utilized in various ligand binding assays. The narrow photoluminescence emission bands at 520 – 550 nm and at 650 – 670 nm are at shorter wavelengths. They are totally discriminated from autofluorescence and scattered excitation light even without temporal resolution. The transparent solution of colloidal bead-milled up-converting phosphor nanoparticles provides intense green emission visible to the human bare eye under illumination by an infrared laser pointer.^{137,138} Therefore, up-conversion materials have been devised for detection of cell and tissue surface antigens as luminescence bioassays.^{138–141}

The inorganic lanthanide-doped crystals have been proven to be useful in bioaffinity assays. About the immunoassays, up-conversion nanoparticles have been used, for example, in enzyme activity assays and DNA-hybridization assays taking advantage of the up-conversion phenomenon.^{34,139}

Chapter 1 State-of-the-art of up-conversion on RE-doped solids

1.5.1.2 Chemical sensors

The chemical sensors are small instruments that were used to detect the presence of certain analytes by producing a signal that can be measured. They usually include two connected units: a chemical receptor for analyte recognition and a physicochemical transducer for producing a signal proportional to the concentration of the analytes. The analyte objects are oxygen, carbon dioxide, hydrogen peroxide, glucose, proteins, nucleic acids, anions, metal ions, cofactors, and coenzymes.³⁴

Traditionally, chemical sensors have contained organic dye molecules, such as rhodamine, that was utilized as luminescent compounds. Currently, there has been increasing interest in using NIR emitting lanthanide ions and up-conversion nanoparticles for better tissue penetration. For example, up-converting nanoparticles have been applied in sensor systems to detect pH, temperature,¹⁴² NH_3 ,¹⁴³ and O_2 .¹⁴⁴

1.5.1.3 Biological imaging

The NIR excitation takes advantages of deep tissue penetration with minimized photodamage, eliminating autofluorescence and increasing the detection sensitivity. In addition, up-conversion nanoparticles are readily internalized by many cell types and in the imaging of blood vessels. As a result, the non-toxic up-conversion nanoparticles are very promising application in biologic imaging fields.¹³⁹ For example, $\text{Gd}^{3+}/\text{Yb}^{3+}/\text{Er}^{3+}$ co-doped NaYF_4 nanophosphors have been used in vivo combining luminescence imaging with PET (positron emission tomography) and UCL (up-conversion luminescence) imaging.¹⁴⁵ Currently, there is an increasing interest towards dual-mode down- and up-conversion in imaging.

Chapter 1 State-of-the-art of up-conversion on RE-doped solids

1.5.2 Lasers

The optically pumped lasers are originally based on a Stokes pumping process. One basic problem is how to obtain a high-density pumping source at a shorter wavelength than their emitting wavelength.¹⁴⁶ One research about this up-conversion laser is $\text{LiYF}_4:\text{Er}^{3+}$ where green (551 nm) and red (619 nm, 669 nm and 702 nm) lasing has been demonstrated by pumping into either $^4\text{I}_{9/2}$ level with wavelengths around 800 nm or the $^4\text{I}_{11/2}$ level with wavelengths around 970 nm.¹⁴⁷

1.5.3 Diodes

Laser diodes (LD) and light-emitting diodes (LEDs) have got fruitful results with many kinds of researches. Infrared up-conversion devices were once extensively investigated since the devices were considered to be candidates for green and blue display devices. Infrared up-conversion devices generally consisted of Yb^{3+} -sensitized and Er^{3+} - or Tm^{3+} -activated fluoride phosphors and GaAs:Si light-emitting diodes (LEDs) as excitation sources.¹⁴⁸ A 980 nm emitting LD has been developed for pumping an Er^{3+} -doped fiber amplifier for optical communication systems. The LD has a higher output (over 50 mW) and good reliability. Since the LD output light can be finely focused, adoption of LD has pronouncedly increased the infrared excitation density and also made it possible to accomplish effective optical confinement.¹⁴⁸

However, the subsequent researches about this application are rare since the overall efficiency of the up-conversion display devices were generally low and inferior to green emitting GaP LEDs. The promising applications count on the enhanced efficiency of up-conversion materials.

Chapter 1 State-of-the-art of up-conversion on RE-doped solids

1.5.4 Displays

A three-color, solid-state, volumetric display based on two-step, two-frequency up-conversion in rare-earth-doped heavy metal fluoride glass is designed.¹⁴⁹ This device uses infrared laser beams that intersect inside a transparent volume of active optical material to address red, green and blue voxels by sequential two-step resonant absorption. Three-dimensional wire-frame images, surface areas, and solids are drawn by scanning the point of intersection of the lasers around inside of the material. The prototype device is driven with laser diodes, uses conventional focusing optics and mechanical scanners, and is bright enough to be seen in ambient room lighting conditions.

1.5.5 Inks for security printing

Security inks are specialized inks used for authentication, anti-counterfeiting, and loss or theft prevention³⁴. Up-conversion phosphors are suitable for various kinds of printing application and can be mixed with several types of inks. These security inks can be added e.g. in plastics, papers, cloths, ceramics, glasses or solutions. Invisible inks contain unconventional dyes or pigments which become visible when exposed to an excitation light source which causes luminescence. Invisible inks are a subcategory of a class of security inks. Such inks are widely used in banknotes or currency as an anti-counterfeiting measurement.

A mono-dispersed dumbbell-shaped lanthanide-doped up- and down-conversion $\text{NaYF}_4:\text{Ln}^{3+}@\text{NaGdF}_4:\text{Ln}^{3+}$ core-shell nanocrystals (CSNPs) were successfully synthesized.¹⁵⁰ These hydrophilic CSNPs are further fabricated into “green”

Chapter 1 State-of-the-art of up-conversion on RE-doped solids

luminescent inks for inkjet printing to create a variety of dual-mode fluorescence patterns (peacock, temple, and logo) on different paper-based substrates (A₄ paper, envelope, and postcard). Primary additive coloured red-green-blue β -NaYF₄:17%Yb³⁺/3%Er³⁺ UCNPs inks were successfully synthesized to do red-green-blue printing.¹⁵¹ These up-conversion based inks provide promising materials and technique for anti-counterfeiting applications.

1.5.6 Solar cells

The efficiency of current photovoltaics is significantly impeded by the transmission loss of sub-band-gap photons. Photon up-conversion is a promising route to circumvent this problem by converting these transmitted sub-band-gap photons into above-band-gap light, where solar cells typically have high quantum efficiency (Figure 1.7).¹⁵²

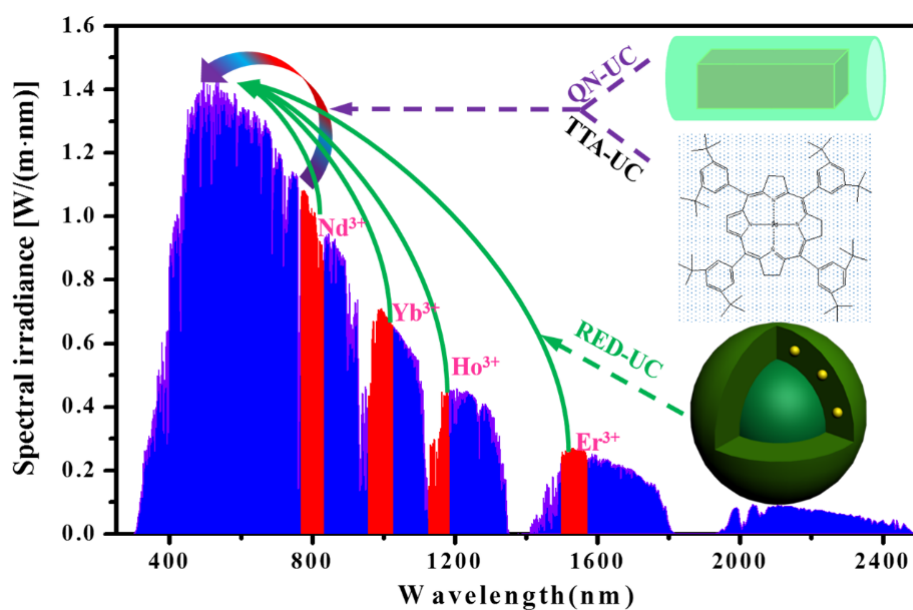


Figure 1.7 The absorption and emission range of three types of up-conversion

Chapter 1 State-of-the-art of up-conversion on RE-doped solids

materials. QN-UC (purple): up-conversion in quantum nanostructures; TTA-UC (purple): triplet-triplet annihilation up-conversion; and RED-UC (green): Rare-earth-doped up-conversion materials.¹⁵²

The inability to absorb infrared (IR) light (700 – 2500 nm), which constitutes 52 % of the energy of the entire solar spectrum, forms the major energy loss mechanism of conventional solar cells. Crystalline silicon (c-Si) photovoltaic (PV) cells are the most used among all types of solar cells on the market.¹⁵³ However, even for single crystalline silicon (Si) PV cells with a rather small semiconductor band-gap (1.12 eV, corresponding to a wavelength of ~1100 nm), the transmission loss of sub-band-gap photons can still amount to about 20% of the sun's energy irradiated onto the Earth's surface.¹⁵⁴

Some related application has been reported.^{25,152,155–158} For example, the NIR to red/green or blue up-conversion lattice NaYF₄ co-doped with Er³⁺, Yb³⁺/Er³⁺ or Yb³⁺/Tm³⁺. It was demonstrated that as much as 50% of the NIR excitation photons contribute to the up-conversion emission.¹⁵⁹

1.6 Conclusion

Chapter 1 gives a general introduction about the state-of-the-art of RE-doped up-conversion. Brief historical background and development of up-conversion have been presented. Three main mechanisms of up-conversion, including excited-state absorption, energy-transfer up-conversion, and photo avalanche have been exhibited. A description of the up-conversion materials constitution, including host materials, activators, and sensitizers has been presented, respectively. A particular introduction

Chapter 1 State-of-the-art of up-conversion on RE-doped solids

about fluoride-based up-conversion nanoparticles has been illustrated. Some obstacles that limit the UCNs development have been analyzed. Finally, some related and promising applications about up-conversion materials have been presented, such as utilizing in biology analytical, lasers, diodes, displays, inks for security printing, and solar cells.

Chapter 2 Experimental section

2.1 Reagents and materials

The purity of $\text{KNO}_3 \cdot 6\text{H}_2\text{O}$, $\text{Y}(\text{NO}_3)_3 \cdot 6\text{H}_2\text{O}$, $\text{Er}(\text{NO}_3)_3 \cdot 6\text{H}_2\text{O}$, $\text{Yb}(\text{NO}_3)_3 \cdot 6\text{H}_2\text{O}$, $\text{Bi}(\text{NO}_3)_3 \cdot 6\text{H}_2\text{O}$, and NH_4F reagents are all 99.99 %. The $\text{Ba}(\text{NO}_3)_2 \cdot 6\text{H}_2\text{O}$ has a purity of 99.999 %. The purity of ethanol is ≥ 99 %. The assay of ethylene glycol is 99 %. The assay of oleic acid is 90 %. The cyclohexane has a 100 % assay on anhydrous substance. The assay of absolute anhydrous pure ethanol is 99.9%.

2.1.1 Precursors utilising in $\text{KYF}_4:10\% \text{Yb}/5\% \text{Er}$ UCNs

In synthesis procedure of $\text{KYF}_4:10\% \text{Yb}/5\% \text{Er}$ samples, all reagents, including $\text{KNO}_3 \cdot 6\text{H}_2\text{O}$, $\text{Y}(\text{NO}_3)_3 \cdot 6\text{H}_2\text{O}$, $\text{Er}(\text{NO}_3)_3 \cdot 6\text{H}_2\text{O}$, $\text{Yb}(\text{NO}_3)_3 \cdot 6\text{H}_2\text{O}$, and NH_4F , were purchased from Aldrich and used as received without further purification or modification. The absolute anhydrous pure ethanol was purchased from CARLO ERBA Reagents and used as received without purification or modification.

2.1.2 Precursors utilising in $\text{BiF}_3:10\% \text{Yb}/5\% \text{Er}$ UCNs

The reactants $\text{Bi}(\text{NO}_3)_3 \cdot 6\text{H}_2\text{O}$, $\text{Er}(\text{NO}_3)_3 \cdot 6\text{H}_2\text{O}$, $\text{Yb}(\text{NO}_3)_3 \cdot 6\text{H}_2\text{O}$, and NH_4F were all purchased from Aldrich and used as received without further purification or modification. The ethylene glycol for dissolving $\text{Bi}(\text{NO}_3)_3 \cdot 6\text{H}_2\text{O}$ was purchased from Sigma-Aldrich and used as received without further purification.

2.1.3 Precursors utilising in $\text{K}_{0.3}\text{Bi}_{0.7}\text{F}_{2.4}:10\% \text{Yb}/5\% \text{Er}$ UCNs

All reagents, including $\text{KNO}_3 \cdot 6\text{H}_2\text{O}$, $\text{Bi}(\text{NO}_3)_3 \cdot 6\text{H}_2\text{O}$, $\text{Er}(\text{NO}_3)_3 \cdot 6\text{H}_2\text{O}$, $\text{Yb}(\text{NO}_3)_3 \cdot 6\text{H}_2\text{O}$,

Chapter 2 Experimental section

and NH_4F , were all purchased from Aldrich and used as received without further purification or modification. The ethylene glycol for dissolving $\text{Bi}(\text{NO}_3)_3 \cdot 6\text{H}_2\text{O}$ was purchased from Sigma-Aldrich and used as received without further purification.

2.1.4 Precursors utilizing in $\text{BaYF}_5:20\%\text{Yb}/2\%\text{Er}$ coated with BaYF_5 UCNs

The precursors, including $\text{Ba}(\text{NO}_3)_2 \cdot 6\text{H}_2\text{O}$, $\text{Y}(\text{NO}_3)_3 \cdot 6\text{H}_2\text{O}$, $\text{Er}(\text{NO}_3)_3 \cdot 6\text{H}_2\text{O}$, $\text{Yb}(\text{NO}_3)_3 \cdot 6\text{H}_2\text{O}$, and NH_4F , were all purchased from Aldrich and used as received without further purification or modification. The ethylene glycol, oleic acid, and cyclohexane were purchased from Sigma-Aldrich, Alfa Aesar, and VWR, respectively. They are all used as received without further purification.

2.2 Synthesis procedure

2.2.1 Synthesis method of $\text{KYF}_4:10\%\text{Yb}/5\%\text{Er}$

For comparison, three different initial K/Y/F ratios (Table 2.1) were designed, including K/Y/F=2/1/5 (A_1 and B_1), K/Y/F=2/1/7 (A_2 and B_2), and K/Y/F=2/1/9 (A_3 and B_3). Moreover, two different reaction conditions A and B at each ratio were designed. The capital letter A stands for the samples prepared only in deionized water while letter B stands for samples prepared in a mixed medium of deionized water and ethanol. The utilizing of mixed deionized water and ethanol could reduce the number of introduced ligands, which populate onto nanoparticles surface to quench the UC process compared with other widely used complicated organic solvents. They are safer, more economical, and more accessible than the complex organic solvents.

Chapter 2 Experimental section

Table 2.1 Specifications of the samples composition synthesized with different initial K/Y/F ratios and reaction solvents.

Samples	Deionized water	Mixed deionized water-ethanol solution
K/Y/F=2/1/5	A ₁	B ₁
K/Y/F=2/1/7	A ₂	B ₂
K/Y/F=2/1/9	A ₃	B ₃

In a typical procedure, 2 mmol $\text{KNO}_3 \cdot 6\text{H}_2\text{O}$, 0.85 mmol $\text{Y}(\text{NO}_3)_3 \cdot 6\text{H}_2\text{O}$, 0.05 mmol $\text{Er}(\text{NO}_3)_3 \cdot 6\text{H}_2\text{O}$, and 0.1 mmol $\text{Yb}(\text{NO}_3)_3 \cdot 6\text{H}_2\text{O}$ were added into 15 ml deionized water and stirring for 5-10 minutes. m (5/7/9) mmol NH_4F was added into 20 ml deionized water (A_1 , A_2 , and A_3) or the mixture of 10 ml ethanol and 10 ml deionized water (B_1 , B_2 , and B_3) and stirring for 5-10 minutes. Then the first solution was added dropwise into the second solution to form white precipitation in the final solution. After stirring the above mixture solution for only 2 minutes, the final solution was washed and dispersed with deionized water and ethanol several times, respectively. The final obtained white samples were dried for 12 h in the dried oven at 90 °C. The samples were annealed at 400 °C for 4 h in a furnace under an argon stream. Not any surfactant, chelator or capping reagents were used.

In addition, other samples synthesized with different initial K/Y/F ratios were also prepared in a similar way except for the different adding amount of the reagents.

2.2.2 Synthesis method of BiF_3 :10%Yb/5%Er

Three different initial Bi/F ratios, including $\text{Bi}/\text{F}=1/3$, $\text{Bi}/\text{F}=1/5$, and $\text{Bi}/\text{F}=1/7$, were designed. At each ratio, undoped samples and 10 mol% Yb and 5 mol% Er co-doped

Chapter 2 Experimental section

samples were prepared. Otherwise, Bi/F=1/9 Yb/Er co-doped BiF₃ sample has also been prepared.

In the procedure of preparing undoped samples, 1 mmol Bi(NO₃)₃·6H₂O was dissolved into 15 ml ethylene glycol (EG) and stirring for 5-10 minutes. Then, *m* (3/5/7; marked with A, B, and C, respectively) mmol NH₄F was dissolved into 15 ml deionized water (DW) and also stirring for 5-10 minutes. Afterward, the above solution dissolved with nitrate was added dropwise into the solution with ammonium fluoride to form white precipitation in the mixed solution. After stirring the solution for only 2 minutes, the final solution was successfully obtained. The products are then washed and dispersed in deionized water and ethanol several times. The white products were dried for 12 h in a dried oven at 90 °C. Not any surfactant, chelators or capping reagents were used.

For synthesizing Yb/Er co-doped samples, 0.85 mmol Bi(NO₃)₃·6H₂O, 0.05 mmol Er(NO₃)₃·6H₂O, and 0.1 mmol Yb(NO₃)₃·6H₂O were dissolved into 15 ml deionized water and stirring for 5-10 minutes. *m* (3/5/7; marked with D, E, and F) mmol NH₄F was added into 15ml deionized water and stirring for 5-10 minutes. The following processes are similar to that of the undoped samples. Besides, in a furnace under an argon stream, the sample E, the Yb/Er doped BiF₃ prepared with Bi/F = 1/5, was annealed at 400 °C for 4 h.

The sample marked with G, which has a similar synthesis process with A except for using ethylene glycol to dissolve NH₄F instead of deionized water, was also prepared

2.2.3 Synthesis method of K_{0.3}Bi_{0.7}F_{2.4}:10%Yb/5%Er

In a typical procedure of preparing Yb/Er co-doped K_{0.7}Bi_{0.3}F_{2.4} nanoparticles, *m*

Chapter 2 Experimental section

(1/2/3) mmol $\text{KNO}_3 \cdot 6\text{H}_2\text{O}$, 0.85 mmol $\text{Bi}(\text{NO}_3)_3 \cdot 6\text{H}_2\text{O}$, 0.05 mmol $\text{Er}(\text{NO}_3)_3 \cdot 6\text{H}_2\text{O}$ and 0.1 mmol $\text{Yb}(\text{NO}_3)_3 \cdot 6\text{H}_2\text{O}$ were added into 15 ml ethylene glycol and stirring for 5-10 minutes. Afterward, 7 mmol NH_4F was dissolved into 15 ml deionized water and stirring for 5-10 minutes. Afterward, the first solution was added dropwise into the solution dissolved with NH_4F to form white precipitation in the final solution. After stirring the solution for only 2 minutes, the compounds were obtained. The compounds were washed and dispersed with deionized water and ethanol several times. The obtained white samples were then dried for 12 h in a drying oven at 90 °C. The samples were annealed at 400 °C for 4 h in a furnace under an argon stream. Not any surfactant, chelator or capping reagents were used.

In the procedure of synthesizing undoped $\text{K}_{0.3}\text{Bi}_{0.7}\text{F}_{2.4}$ nanoparticles, m (1/2/3) mmol $\text{KNO}_3 \cdot 6\text{H}_2\text{O}$ and 1 mmol $\text{Bi}(\text{NO}_3)_3 \cdot 6\text{H}_2\text{O}$ were dissolved into 15 ml ethylene glycol and stirring for 5-10 minutes. The following processes are the same as that of the Yb/Er co-doped samples.

2.2.4 Synthesis method of $\text{BaYF}_5:20\%\text{Yb}/2\%\text{Er}@ \text{BaYF}_5$

In a typical procedure of preparing $\text{BaYF}_5:20\%\text{Yb}/2\%\text{Er}$ nanoparticles: 1 mmol $\text{Ba}(\text{NO}_3)_2 \cdot 6\text{H}_2\text{O}$, 0.78 mmol $\text{Y}(\text{NO}_3)_3 \cdot 6\text{H}_2\text{O}$, 0.02 mmol $\text{Er}(\text{NO}_3)_3 \cdot 6\text{H}_2\text{O}$, and 0.2 mmol $\text{Yb}(\text{NO}_3)_3 \cdot 6\text{H}_2\text{O}$ were dissolved into the mixed solution of 5 ml deionized water, 5 ml oleic acid, and 10 ml ethylene glycol to stirring for 5-10 minutes. Afterward, 5 mmol NH_4F was dissolved into 5 ml deionized water and 5 ml ethylene glycol after 5-10 minutes stirring. Then the first solution was added dropwise into the solution dissolved with NH_4F and stirred for 5-10 minutes. The obtained solution was moved into a sealed autoclave to react at 200 °C for 12 hours. When cooling down to room

Chapter 2 Experimental section

temperature, the compounds were separated by centrifugation. Then 1:4 volume mixed cyclohexane and ethanol were used to wash the compounds several times. Afterward, ethanol was still used to wash the compounds several times. The final obtained white samples were dried for 12 h in a drying oven at 90 °C.

In a typical procedure of synthesizing BaYF₅:20%Yb/2%Er coated with BaYF₅ nanoparticles: 1 mmol Ba(NO₃)₂·6H₂O, 0.78 mmol Y(NO₃)₃·6H₂O, 0.02 mmol Er(NO₃)₃·6H₂O, and 0.2 mmol Yb(NO₃)₃·6H₂O were dissolved into the mixed solution of 5 ml deionized water, 5 ml oleic acid, and 10 ml ethylene glycol to stirring for 5-10 minutes. 12 mmol NH₄F was dissolved into 5 ml deionized water and 5 ml ethylene glycol for 5-10 minutes stirring. Then the first solution was dropwised into the second solution and stirred for 5-10 minutes. The final solution was moved into a sealed autoclave to react at 200 °C for 12 hours. When cooling down to room temperature, 5 ml deionized water with 1 mmol Y(NO₃)₃·6H₂O and 1 mmol Ba(NO₃)₂·6H₂O was added into the prepared solution with BaYF₅:20%Yb/2%Er compound and stirred for 5-10 minutes. The solution was resealed in an autoclave to react at 180 °C for 4 h. After cooling down to room temperature, the compounds were collected by centrifugation. The mixed cyclohexane and ethanol with 1:4 volume were used to wash the compounds several times. Then, the ethanol was used to wash the compounds several times. The obtained white samples were dried for 12 h in a drying oven at 90 °C.

2.3 Characterization experiment

The powders X-ray diffraction (XRD) data were measured on an X'Pert Pro Diffractometer (Panalytical) with Cu K α ($\lambda = 1.5406 \text{ \AA}$) radiation (40 kV, 45 mA).

Chapter 2 Experimental section

The program Fullprof Suite was used to do the profile refinement of XRD patterns.

Williamson-Hall method was adopted to calculate the average crystallite sizes.¹⁶⁰ Based on the XRD data, crystallite sizes were acquired from full-widths at half-maximum (FWHM) of the given peaks. The Bragg peak breadth $B_{measurement}$ is the squares sum of sample B_{sample} and instrumental contributions $B_{instrument}$:

$$B_{sample} = \sqrt{B_{measurement}^2 - B_{instrument}^2} \quad (1)$$

Standard LaB₆ was used to determine the instrumental broadening $B_{instrument}$ allowing calculating B_{sample} using Equation (1).

Actually, microstrains are very common in nanoparticle materials and therefore the peak broadening B_{sample} is due to both microstrains, $B_{microstrains} = 4\varepsilon \sin(\theta)/\cos(\theta)$, and crystallite size, $B_{size} = K\lambda/D\cos(\theta)$ (Scherrer Formula). The Equation (2) is given as follow:

$$B_{sample} = 4\varepsilon \frac{\sin(\theta)}{\cos(\theta)} + \frac{K\lambda}{D\cos(\theta)} \quad (2)$$

Where θ is the diffraction angle, K is Scherrer constant, ε is the microstrain coefficient, λ is X-ray wavelength ($\lambda = 0.15046$ nm), and D is crystallite size. The Scherrer constant K depends on the crystal shape, size distribution and particular the method used to estimate the broadening of the peaks. For spherical particles, a cubic symmetry and a full width at half maximum method was used to estimate the broadening, the K is taken as 0.94. ε is the microstrain coefficient, which is mainly caused by no-uniform lattice distortions, dislocations, antiphase domain boundaries,

Chapter 2 Experimental section

grain surface relaxation, and so on.

Rearranging Equation (2) gives:

$$B_{\text{sample}} \cos(\theta) = 4\varepsilon \sin(\theta) + \frac{K\lambda}{D} \quad (3)$$

Then $B_{\text{sample}} \cos(\theta)$ was plotted as function of $4 \sin(\theta)$. The slope and y-intercept of the linear regression lines stand for strain effect and size effect, respectively. Once the y-intercept was acquired from the fitting lines, substituting it into $y\text{-intercept} = K\lambda/D$ equation to calculate crystallite size D .

Transmission electron microscope (TEM) images were captured on a JEOL JEM 2100Plus (equipped with a LaB₆ filament) microscope operating at 200 kV. The images were collected with a 4008 × 2672 pixel CCD camera (Gatan Orius SC1000). The size distribution histogram was draw from the TEM images with ImageJ software.

The absorption spectra were measured with the Cary 6000i UV-Vis-NIR Spectrophotometer.

The internal quantum yields (QY) of the prepared powders were calculated by the emission spectra, which were collected by an integrating sphere. The integrating sphere is shown in Figure 2.1. The ~ 974 nm excitation laser source with 1080 mA power was from a laser diode & temperature controller of Unique-Mode laser technology. The Ocean Optics HR 4000 spectrometer (200 – 1100 nm) was used to collect the emission spectrum.

For an internal quantum yield measurement, two experiments are necessary. The first experiment was done only with a transparent glass slide in the sphere. The

Chapter 2 Experimental section

second experiment measured the samples onto the glass slide, which was put into the integrating sphere. The emission spectra of these two experiments were obtained. After calculating the difference of the emission peaks area near 974 nm of these two experiments, the absorption was obtained. Afterward, the area at red and green emission light was calculated from the spectrum of the second experiment. Finally, internal UCQY was obtained. The configurations of the experimental instrument and the detailed processes are similar to a measurement of external quantum yield by Prof. R. H. Friend.¹⁶¹



Figure 2.1 The integrating sphere that was used in the measurement of internal UCQY.

The emission spectra and fluorescence decay time measurement were all excited under a tunable Ekspla NT342B OPO laser with 7 ns pulsed duration. A CCD camera (Princeton Instruments) equipped with a monochromator (Acton Research, 300 lines/mm) was used to measure the fluorescence spectra. An RCA 8850

Chapter 2 Experimental section

photomultiplier was used to detect the decay curves. All measurements were performed at room temperature.

Chapter 3 Results and discussion

3.1 KYF₄:10%Yb/5%Er

KYF₄ melts non-congruently, which makes crystal growth rather critical. It is a good optical quality crystal. The KYF₄ has low phonon energy and shows a similar structure with NaYF₄.

The crystal structure of KYF₄ has been determined by single-crystal X-ray analysis.¹⁶² Tetragonal KYF₄ is recognized as a fluorite-related superstructure and hexagonal KYF₄ is distorted fluoride structure.¹⁶³ However, we do not find the cubic phase information in the current database of XRD patterns as far as we know. There are only a few articles reporting the cubic KYF₄-based UCNs.^{162,164–166}

Chapter 3 Results and discussion

3.1.1 Structure

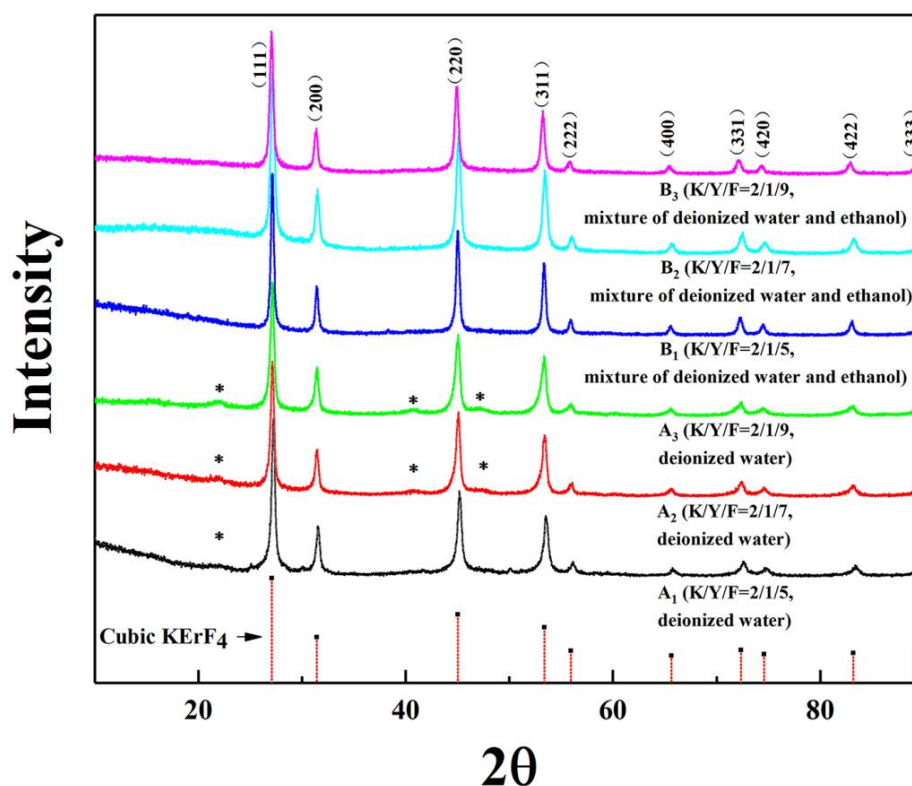


Figure 3.1.1 X-ray powders diffraction patterns of cubic $\text{KYF}_4:10\% \text{Yb}/5\% \text{Er}$ compounds with different K/Y/F ratios.

Figure 3.1.1 shows X-ray diffraction (XRD) patterns of the as-prepared powders and this of the cubic KErF_4 (space group Fm-3m , PDF 00-065-0575) for comparison. Indeed, XRD patterns of $\text{KYF}_4:10\% \text{Yb}/5\% \text{Er}$ showed in Figure 3.1.1 is unmatched with the XRD patterns of hexagonal or tetragonal KYF_4 compounds recorded in the databases while they are in good accordance with that of cubic KErF_4 . This result is in agreement with previous works. For example, Schafer et al.¹⁶² firstly reported in 2008, cubic $\text{KYF}_4:\text{Yb}/\text{Er}$ nanoparticles with a mean size of 13 nm that were synthesized in the high boiling organic solvent N-(2-hydroxyethyl) ethylenediamine (HEEDA) at

Chapter 3 Results and discussion

200 °C. They used cubic α -NaYF₄ as a structural model and explained that the two patterns had similar diffraction intensity and all peaks of the α -NaYF₄ shift towards high angle compared with their samples.¹⁶² Later, several articles reported cubic KYF₄ UC nanocrystal including KYF₄:Nd³⁺ by microwave-hydrothermal crystallization,¹⁶⁴ KYF₄:Eu³⁺ by hydrothermal method,¹⁶⁵ and KYF₄:Eu³⁺ by modified thermal decomposition method.¹⁶⁶

As a result, it was demonstrated that pure cubic KYF₄ nanoparticles were synthesized by co-precipitation method at room temperature in a deionized water-ethanol solvent (B₁, B₂, and B₃), which is an extremely facile and fast method compared with other ones.^{162,164–166} To our knowledge, it is the first time at room temperature that Yb/Er co-doped KYF₄ UCNs are prepared in the water-ethanol medium.

However, some very weak diffraction peaks are found and marked with the asterisk in the XRD patterns of KYF₄:10%Yb/5%Er prepared only in deionized water (A₁, A₂, and A₃) in Figure 3.1.1. In previous works,^{162,164} similar weak diffraction peaks were observed in the XRD patterns of KYF₄ compounds synthesized with an analogous method, but the phases due to these peaks were not discussed and identified. After a careful analysis of the positions and intensities of these diffraction lines, it appears that these ones may belong to another potassium yttrium fluoride compounds cubic KY₃F₁₀ (PDF-01-084-5197).

In conclusion, the use of the mixed ethanol-water medium for syntheses of KYF₄ compounds at RT leads to the systematic presence of impurities in the samples synthesized in deionized water only, while they are absent in the ones synthesized in a mixed ethanol-water medium.

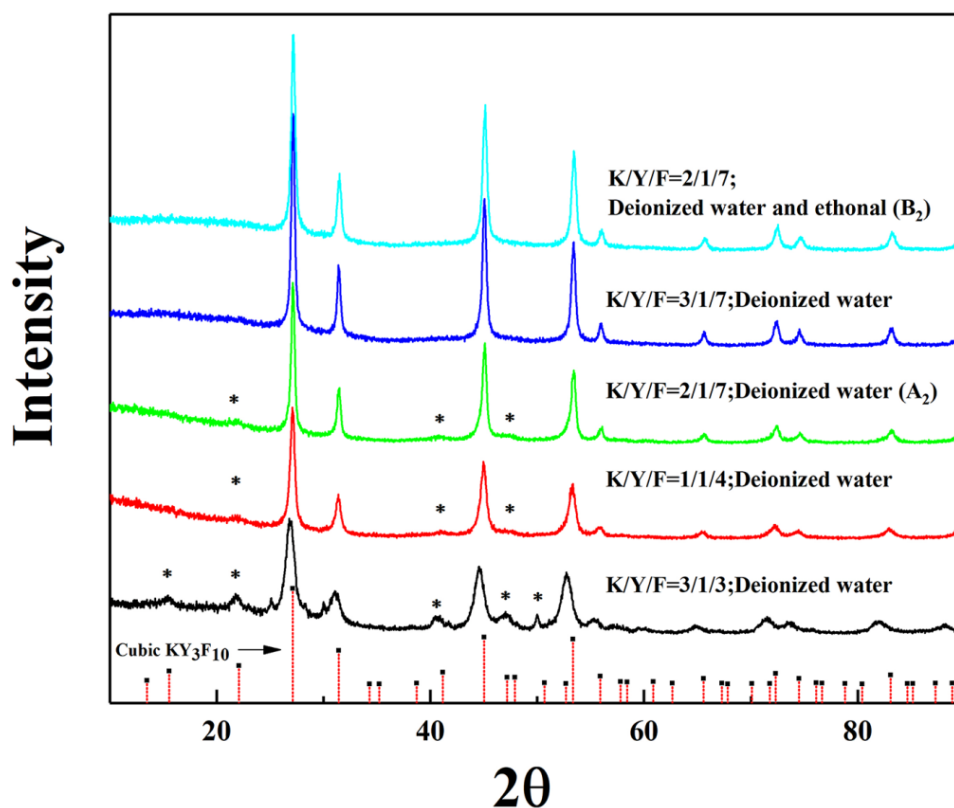


Figure 3.1.2 X-ray powder patterns of the cubic KYF_4 with different initial K/Y/F ratios for comparison.

Meanwhile, in the following experiments, we found that the peaks due to impurities disappear if the quantity of potassium is increased in the K/Y ratio (from 2/1 to 3/1) in the samples prepared only in deionized water. The result is shown in Figure 3.1.2. This result indicates clearly that it is necessary to work in a large excess of potassium when only deionized water is used. Otherwise, the large F/K ratio is also essential. For example in $\text{K/Y/F} = 3/1/3$ XRD pattern, the situation is worse compared with $\text{K/Y/F} = 3/1/7$. So, the impurity peaks are due to low amounts of initial adding K^+ and F^- that are not sufficient to form pure cubic KYF_4 . Apart from enhancing the amounts

Chapter 3 Results and discussion

of K^+ and especial F^- , the previous statements about the use of mixed ethanol-water medium rather than, which changes the reaction equilibrium constants, can also promote the expected reaction and acquire pure cubic KYF_4 phase.

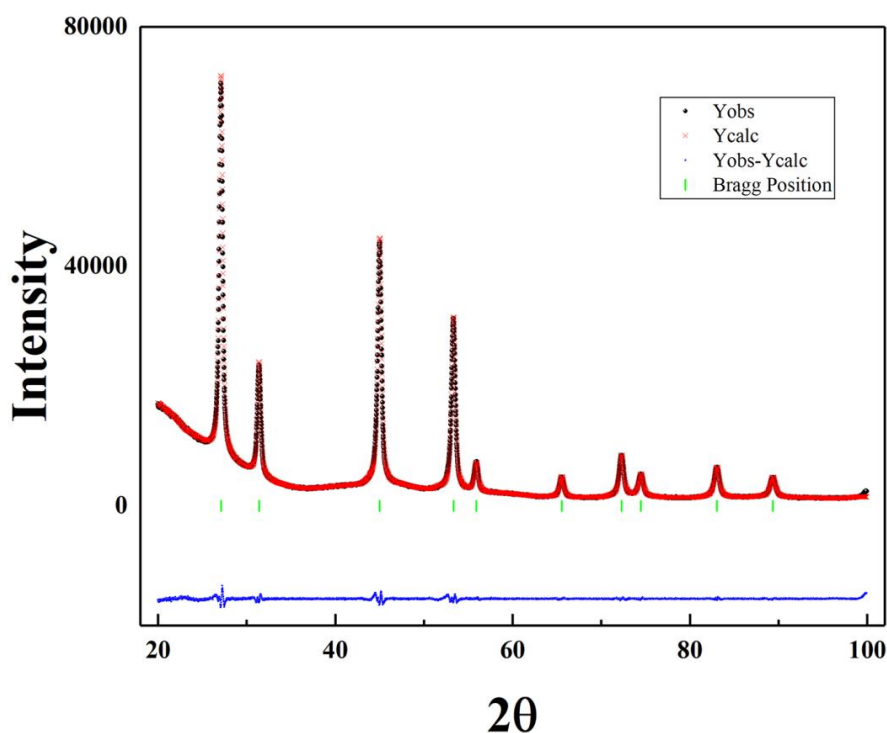


Figure 3.1.3 Refinement of XRD pattern of B_3 sample.

Figure 3.1.3 exhibits the XRD profile refinement of the sample B_3 recorded with a slow scanning speed. The calculated profile fits well with the observed XRD pattern. Cubic Yb/Er co-doped KYF_4 crystallizes in a fluorite-like crystal structure in which cations sites are statically occupied by Y^{3+} , Yb^{3+} , and Er^{3+} cations. The refined lattice parameter of the cubic unit cell is $a = 5.6926 \text{ \AA}$. It is larger than that of $KErF_4$ whose is 5.6862 \AA .¹⁶⁷ The Shannon ionic radius of Y^{3+} , Yb^{3+} , and Er^{3+} with VIII coordination number is 1.159 \AA , 1.125 \AA , and 1.144 \AA , respectively.^{115,168} The Y^{3+} has a bigger Shannon ionic radius than Er^{3+} , it is the reason why $KYF_4:10\%Yb/5\%Er$

Chapter 3 Results and discussion

nanoparticles have a larger lattice parameter than KerF_4 .

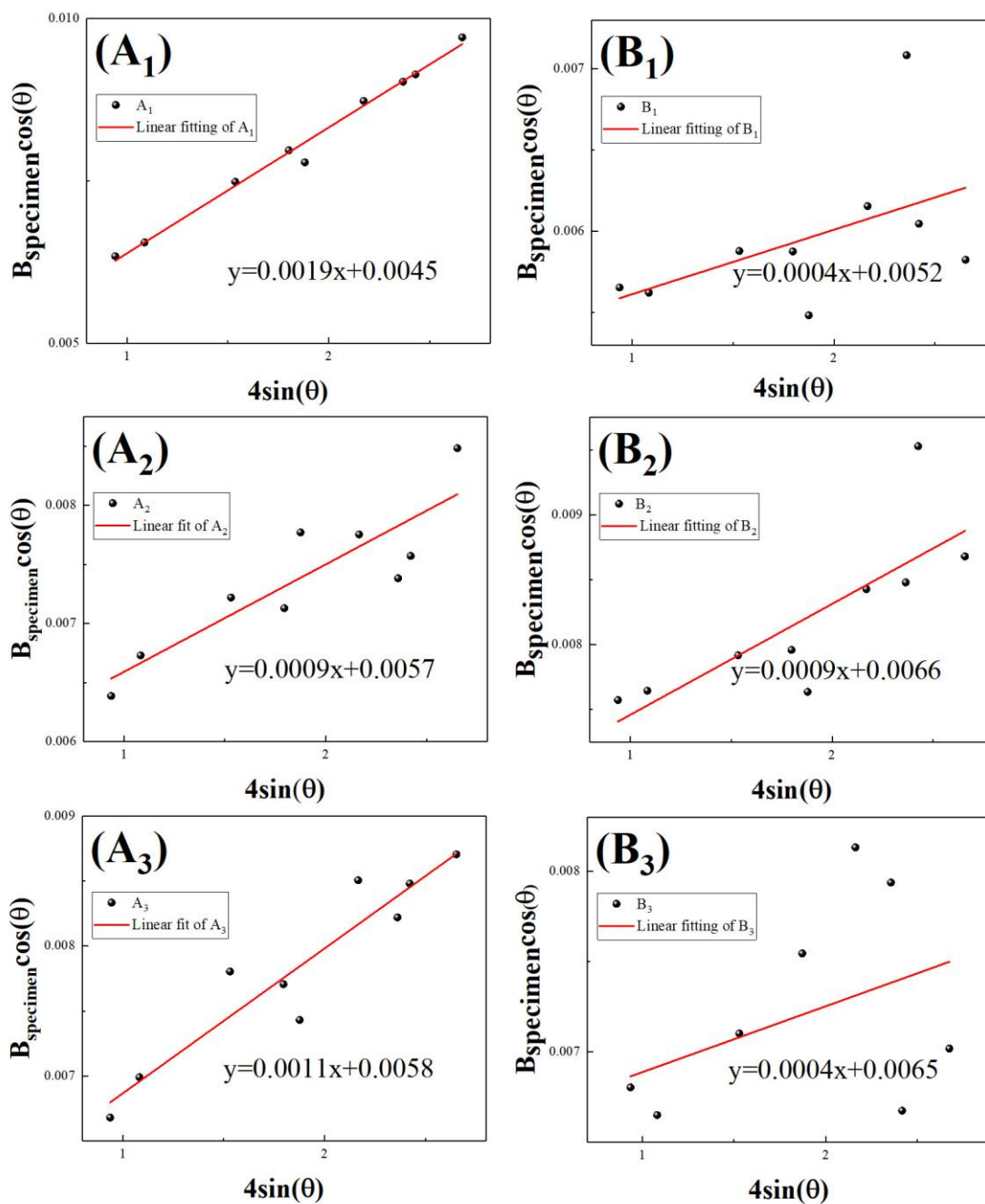


Figure 3.1 4 Linear fitting $B_{\text{sample}} \cos(\theta)$ versus $4\sin(\theta)$ of the sample A₁, A₂, A₃, B₁, B₂, and B₃.

Williamson-Hall method was adopted to calculate the average crystallite sizes.

According to the XRD data, crystallite sizes were obtained from full-widths at

Chapter 3 Results and discussion

half-maximum (FWHM) of the peaks (111), (200), (220), (311), (222), (400), (331), (420), and (422). Figure 3.1.4 shows the linear regression line of sample A₁, A₂, A₃, B₁, B₂, and B₃ while Figure 3.1.5 (A) and (B) gives a schematic representation of the calculated crystallite size D and microstrain coefficient ε of A₁, A₂, A₃, B₁, B₂, and B₃, respectively.

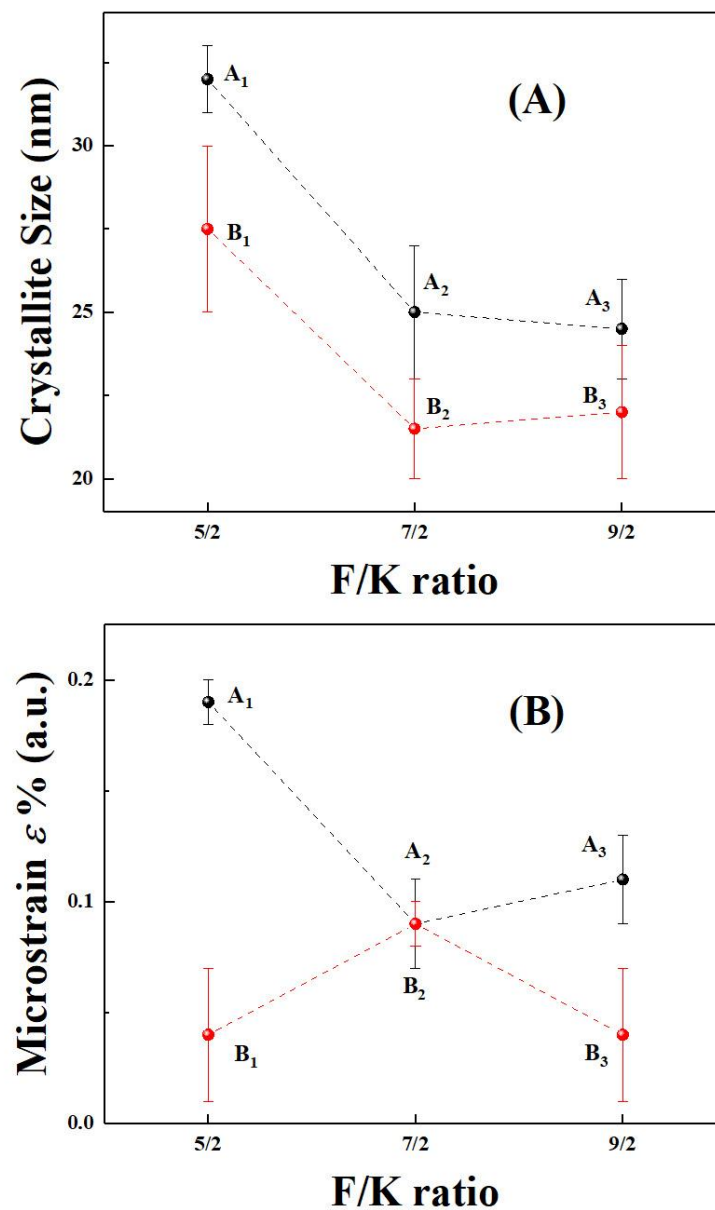


Figure 3.1.5 The photograph of variation trend of: A) the calculated crystallite size D ; and B) microstrain coefficient ε , with different K/Y/F ratios.

Chapter 3 Results and discussion

In comparison of the size D in Figure 3.1.5(A), it indicates that the crystallite size reduces when increasing the initial addition of F^- amounts for both A series samples. Large F^- concentration slightly restrains the crystallite growth. B series samples indicated overall low microstrain when compared with A series samples.

Table 3.1.1. The calculated mean crystallite size D and microstrain ε .

Samples	$Y_{\text{intercept}} (\times 10^{-3})$	Mean crystallite size	ε (%)
A ₁	4.5 ± 0.2	32 ± 1 nm	0.19 ± 0.01
A ₂	5.7 ± 0.4	25 ± 2 nm	0.09 ± 0.02
A ₃	5.8 ± 0.3	25 ± 2 nm	0.11 ± 0.02
B ₁	5.2 ± 0.5	27 ± 2 nm	0.04 ± 0.03
B ₂	6.6 ± 0.5	21 ± 1 nm	0.09 ± 0.02
B ₃	6.5 ± 0.6	22 ± 2 nm	0.04 ± 0.03

Table 3.1.1 collected the values of the calculated mean crystallite sizes D and microstrain ε of all the samples. A₁ sample shows the largest calculated crystallite size 32 nm while B₂ sample shows the smallest crystallite size 21 nm. Large amounts of F^- indeed mildly restrain the growth of the crystallite.

3.1.2 Morphology

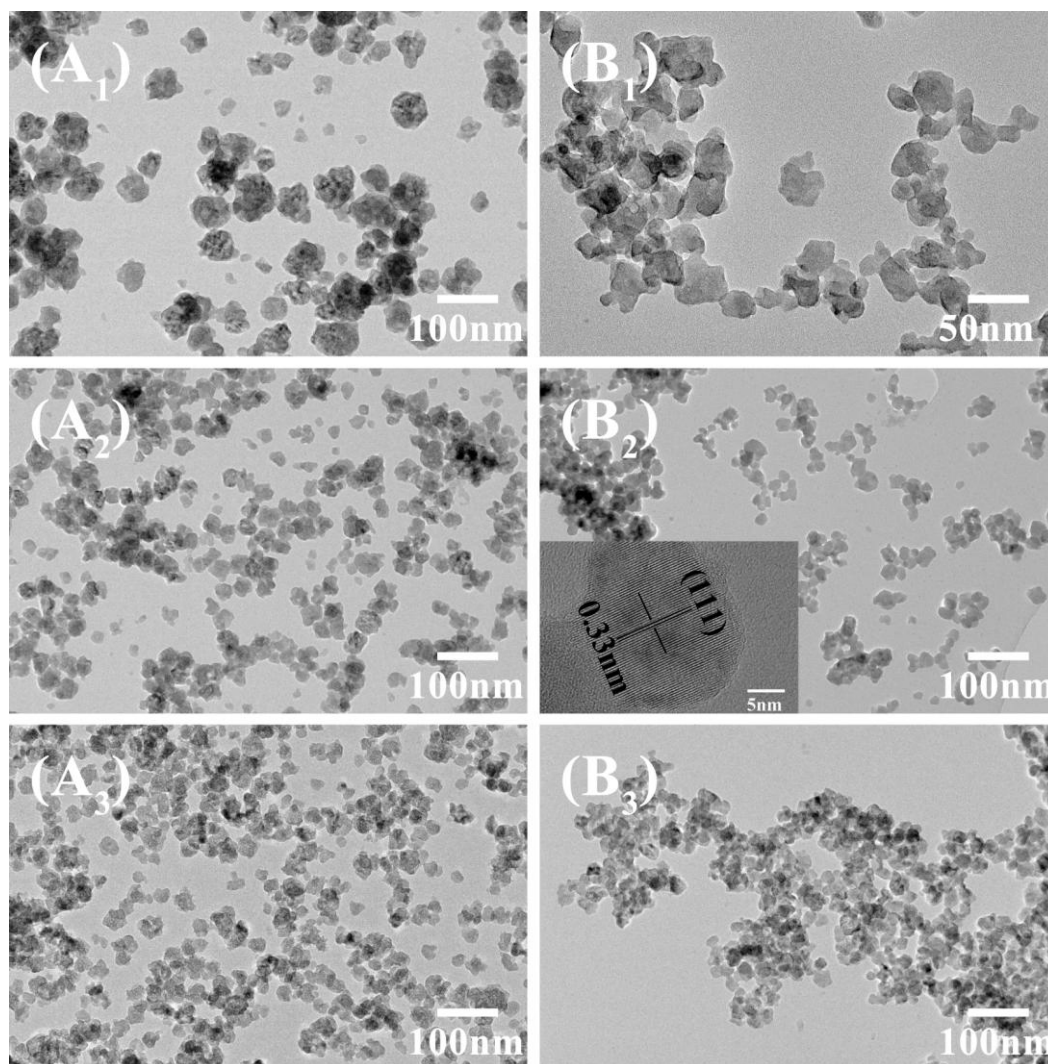


Figure 3.1.6 Transmission electron microscope (TEM) photographs of the synthesized A₁, A₂, A₃, B₁, B₂, and B₃ nanoparticles.

Chapter 3 Results and discussion

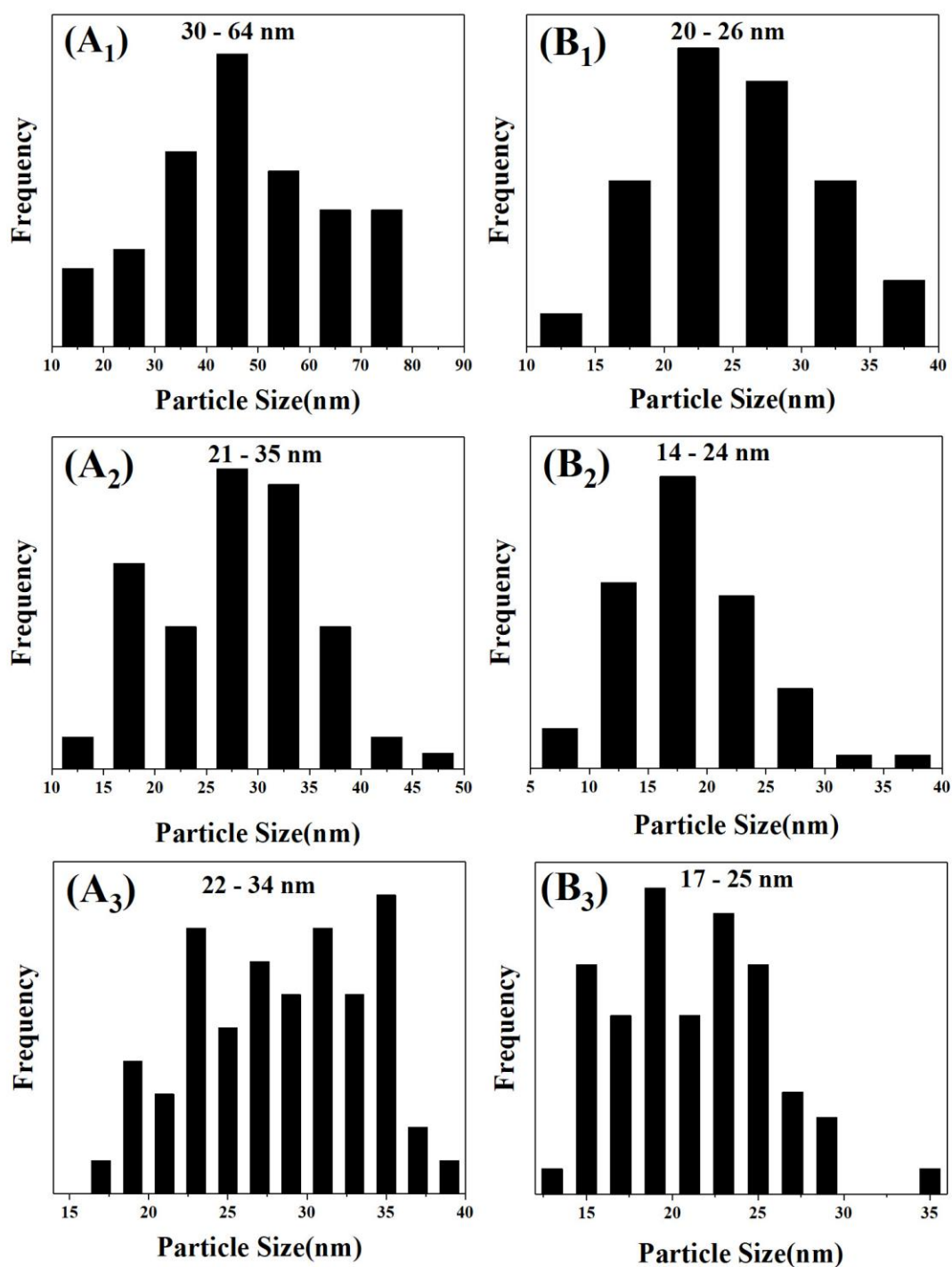


Figure 3.1.7 Size distribution histogram of: (A₁) A₁ sample; (A₂) A₂ sample; (A₃) A₃ sample; (B₁) B₁ sample; (B₂) B₂ sample; and (B₃) B₃ sample.

Chapter 3 Results and discussion

Table 3.1.2. The comparison of nanoparticle size distribution from HRTEM and calculated mean crystallite size D from XRD patterns.

Samples	Nanoparticle size distribution from TEM	Mean crystallite size from XRD
A ₁	30 - 64 nm	32 ± 1 nm
A ₂	21 - 35 nm	25 ± 2 nm
A ₃	22 - 34 nm	25 ± 2 nm
B ₁	20 - 26 nm	27 ± 2 nm
B ₂	14 - 24 nm	21 ± 1 nm
B ₃	17 - 25 nm	22 ± 2 nm

Figure 3.1.6 illustrates the transmission electron microscope (TEM) images of the prepared nanoparticles. Figure 3.1.7 gives the size distribution histogram of the prepared samples based on the TEM images. Table 3.1.2 collected the comparison of the size distribution and calculated mean crystallite size obtained by XRD patterns.

The nanoparticle size distribution of A₁, 30 - 64 nm is larger than the calculated 32 nm mean crystallite size. Except for the nanoparticles of A₁ sample, the nanoparticle sizes of the rest of the samples are in good accordance with the calculated mean crystallite sizes and each particle corresponds to only one single nanocrystal. The inset of Figure 3.1.6 (B₂) shows a set of parallel lattice fringes and the observed 0.33 nm d-spacing is in good agreement with cubic (111) lattice plane of KYF₄.¹⁶⁶ It is also a piece of evidence that the prepared samples indeed belong to cubic KYF₄ phase structure.

Though morphology is difficult to control under co-precipitation methods, B series

Chapter 3 Results and discussion

samples show well-dispersed nanoparticles with a homogeneous morphology. The uniformity and sphere morphology are favourable for the photoluminescence properties. The nanoparticles, less than 50 nm diameter, are suitable for bioimaging due to the reason that they have high cellular uptake and desirable clearance rate.¹⁶⁴ In addition, the deionized water-ethanol reaction solvent reduces the complicated organic solvent residual, makes the nanoparticles safe to be used in vivo biological cells.

3.1.3 Photoluminescence properties

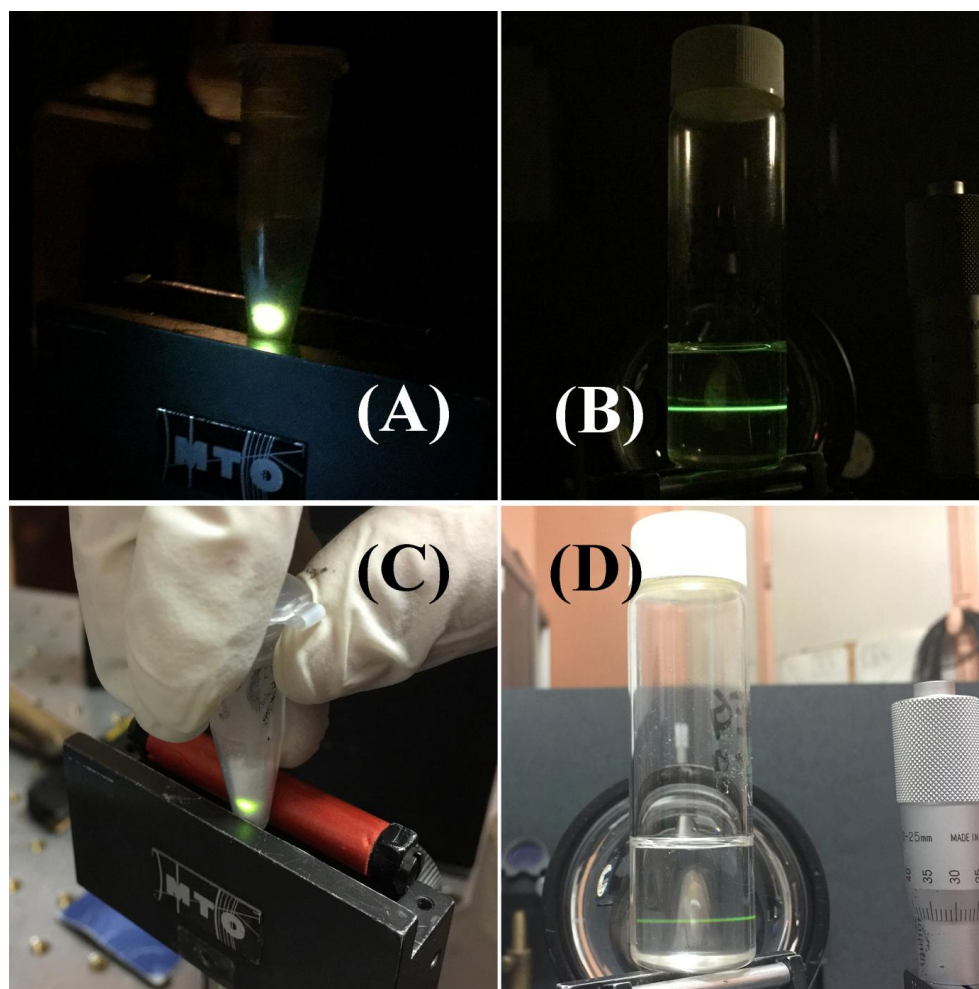


Figure 3.1.8 Emission light photographs of annealed B₁ sample under 974 nm pulsed laser excitation: (A) powders in dark; (B) 0.05 g/L colloidal solution in (ethylene

Chapter 3 Results and discussion

glycol) EG in dark; (C) powders under the lamp; and D) colloidal solution under the lamp.

Figure 3.1.8 shows photographs of annealed powder and colloidal solution of annealed B₁ sample under excitation of a 974 nm pulsed laser. Figure 8(A) and Figure 8(B) illustrate visible and strong green emission light in a darkroom from nanoparticle powder and 0.05 g/L colloidal solution in ethylene glycol, respectively. In comparison, Figure 8(C) and Figure 8(D) show emission under fluorescent lamps and also exhibit an easily observable green emission. The strong emission green light indicates that the prepared sample really possesses good photoluminescence properties.

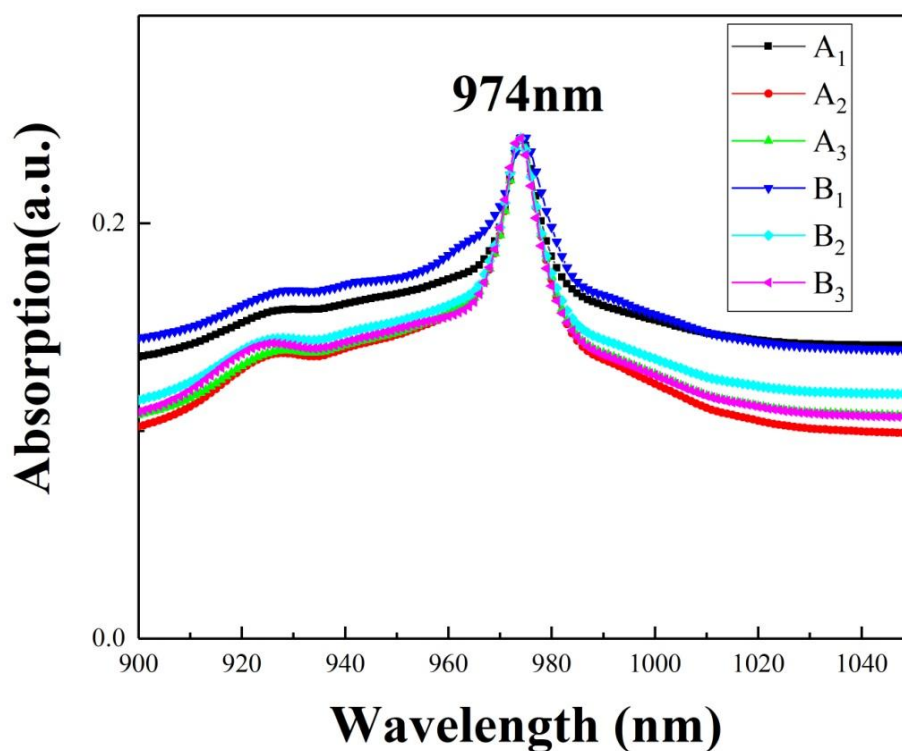


Figure 3.1.9 Absolute absorption spectra of prepared KYF₄ samples from 900 nm to 1050 nm.

Chapter 3 Results and discussion

Figure 3.1.9 illustrates the absorption spectra of the prepared samples from 900 nm to 1050 nm. For each sample, the absorption spectra show a very obvious emission peak at 974 nm. It is due to the co-doping of Yb/Er into the KYF₄ matrix. It is also an evidence for choosing 974 nm laser as the exciting laser.

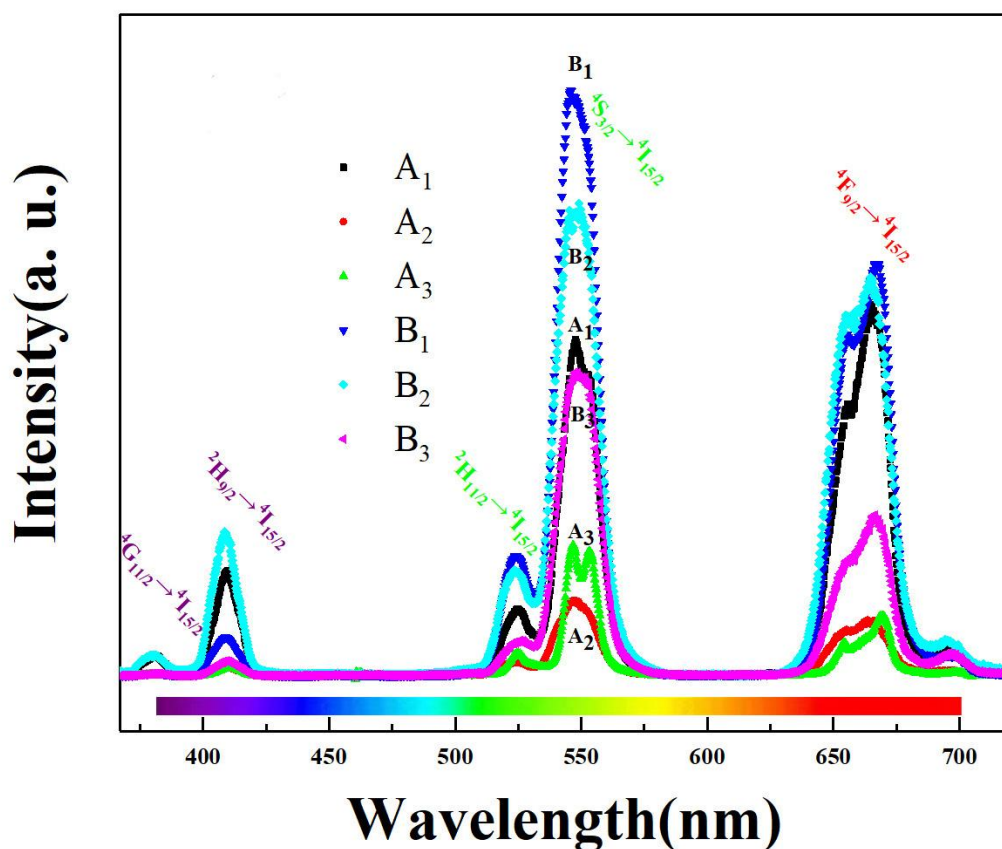


Figure 3.1.10 The emission spectra of as-prepared KYF₄ nanocrystals.

Figure 3.1.10(A) gives the emission spectra of the as-prepared nanocrystal under 974 nm pulsed laser excitation. The prepared nanoparticles exhibit intense characteristic emission peaks at 543 nm and 656/666 nm, weak peaks at 378 nm, 410 nm, and 523 nm. The peaks at 378 nm, 410 nm, 523 nm, 543 nm, and 656/666 nm are ascribed to the $^4G_{11/2} \rightarrow ^4I_{15/2}$, $^2H_{9/2} \rightarrow ^4I_{15/2}$, $^2H_{11/2} \rightarrow ^4I_{15/2}$, $^4S_{3/2} \rightarrow ^4I_{15/2}$, and $^4F_{9/2} \rightarrow ^4I_{15/2}$

Chapter 3 Results and discussion

transitions of Er^{3+} , respectively.^{18,64,123} It demonstrates that the activators Er^{3+} were successfully inserted into the host lattice. As predicted, B series samples have a high luminescent intensity than counterpart A series samples, which are associated with the pure phase, high crystallinity, uniform nanoparticles morphology and low strain effect. The enhancement of crystallinity and phase purity, uniform and sphere-like morphology provide a homogeneous and stable chemical constitution circumstance that is in favour of the Er^{3+} transition and further reinforce the photoluminescence intensity.

Chapter 3 Results and discussion

Table 3.1.3 The relative emitting intensity of the prepared samples at 543 and 666 nm.

Samples	Relative Emitting Intensity at 543 nm (a. u.)	Relative Emitting Intensity at 666 nm (a. u.)
A₁	2.1	3.3
A₂	0.6	0.5
A₃	0.6	0.4
A₃-T	4.4	3.3
B₁	4.7	3.7
B₂	3.7	3.5
B₃	2.2	1.4

Note: A₃-T stands for the annealed sample A₃.

Table 3.1.3 collected the overall data of relative emitting intensity at 543 nm and at 666 nm from the prepared KYF₄ samples. B series samples show overall obviously higher emitting intensity than counterpart of A series samples at both 543 nm and 666 nm. Especially, B₁ sample exhibits the largest relative emitting intensity.

Table 3.1.4 The internal quantum yield of the annealed B₁ sample at 543 nm and 666 nm, measured by a integrating sphere.

Sample	Internal quantum yield of green emission light (centred at 543 nm)(%)	Internal quantum yield of red emission light (centred at 666 nm)(%)
B₁-T	0.20	0.14

Chapter 3 Results and discussion

Meanwhile, the internal QY of the annealed sample B₁, 0.20 % at 543 nm and 0.14 % at 666 nm, is collected in Table 3.1.4. The internal QY of different UCNs is very difficult to accurately compare owing to the utilizing of different laser power and different measurement methods. Currently, the internal QY of the reported β -NaYF₄:20%Yb³⁺, 2% Er³⁺ ranged from 0.005 - 0.3 % with 8 nm - 100 nm nanoparticles at green emission light under a 980 nm excitation laser.²⁵

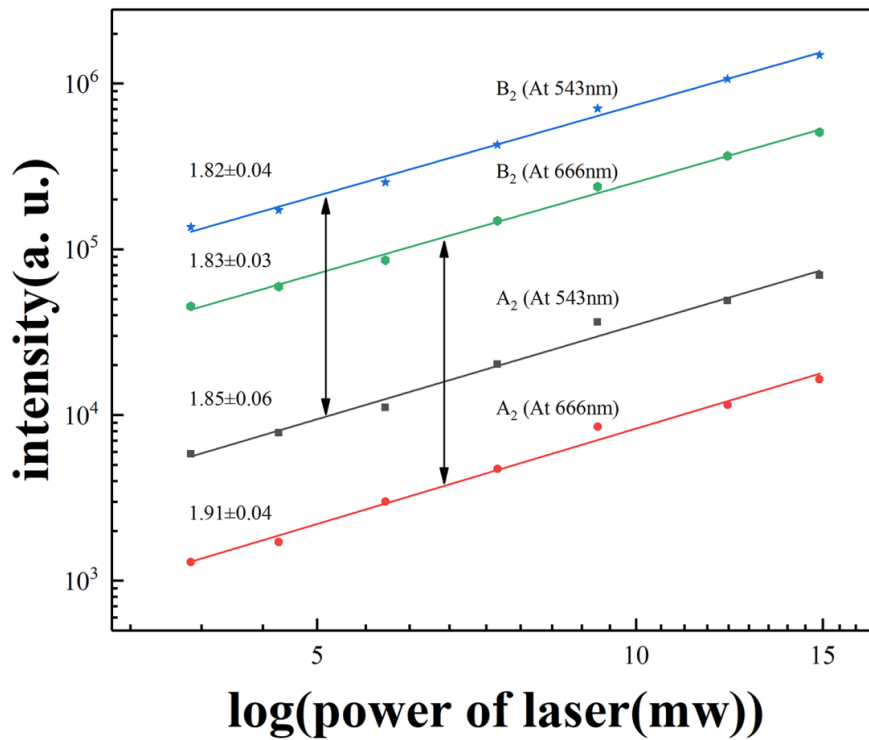


Figure 3.1.11 Log - log plots of emission intensity versus exciting laser power.

In general, the relationship between the UC emission intensity (I_{UC}) and excitation pump power (P) can be defined as:

$$I_{UC} \propto P^n \text{ or } \log(I_{UC}) \propto n \log(P), \quad (1)$$

where n is the number of absorption photons, which populate the ion from ground state to the upper excited level.¹³⁴ According to the red (${}^4S_{3/2} \rightarrow {}^4I_{15/2}$ transitions of Er³⁺)

Chapter 3 Results and discussion

and green (${}^4F_{9/2} \rightarrow {}^4I_{15/2}$ transitions of Er^{3+}) emission, two photons are essential to complete the UC process. Therefore, the theoretical values at red and green emission are all 2.¹⁶² The fitted slope 1.82, 1.83, 1.85, and 1.91 (Figure 3.1.11) are near to the theoretical value of 2, which means the excited state actually absorb two photons. The gap is resulted from the competing decay processes depleting the Er^{3+} -state after the first photon absorption in the $\text{Yb}^{3+}/\text{Er}^{3+}$ couple situation.¹⁴⁶

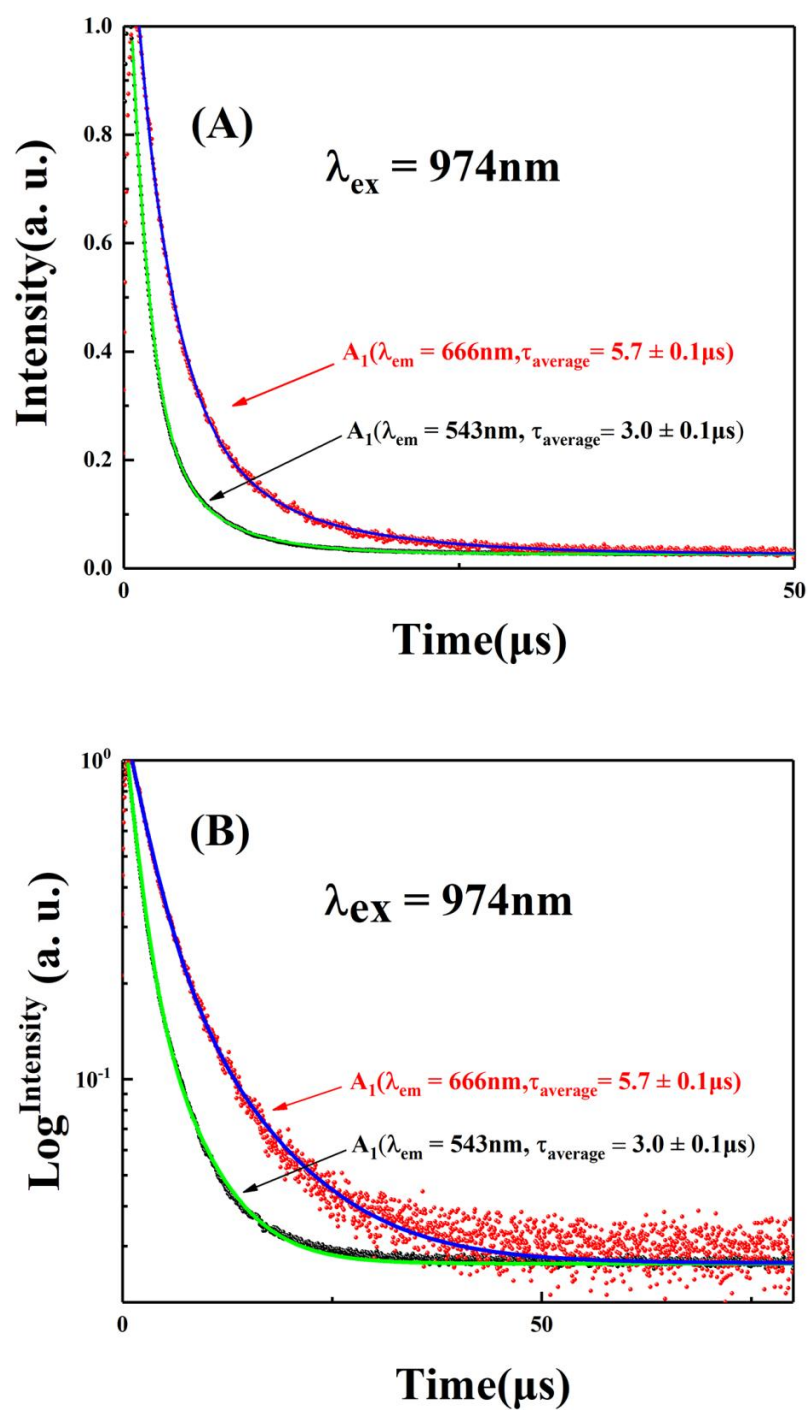


Figure 3.1.12 The decay curve of A_1 with (A) linear y-axis and (B) logarithmic y-axis, at 543 nm (${}^4S_{3/2} \rightarrow {}^4I_{15/2}$) and 666 nm (${}^4F_{9/2} \rightarrow {}^4I_{15/2}$) under 974 nm pulsed excitation laser.

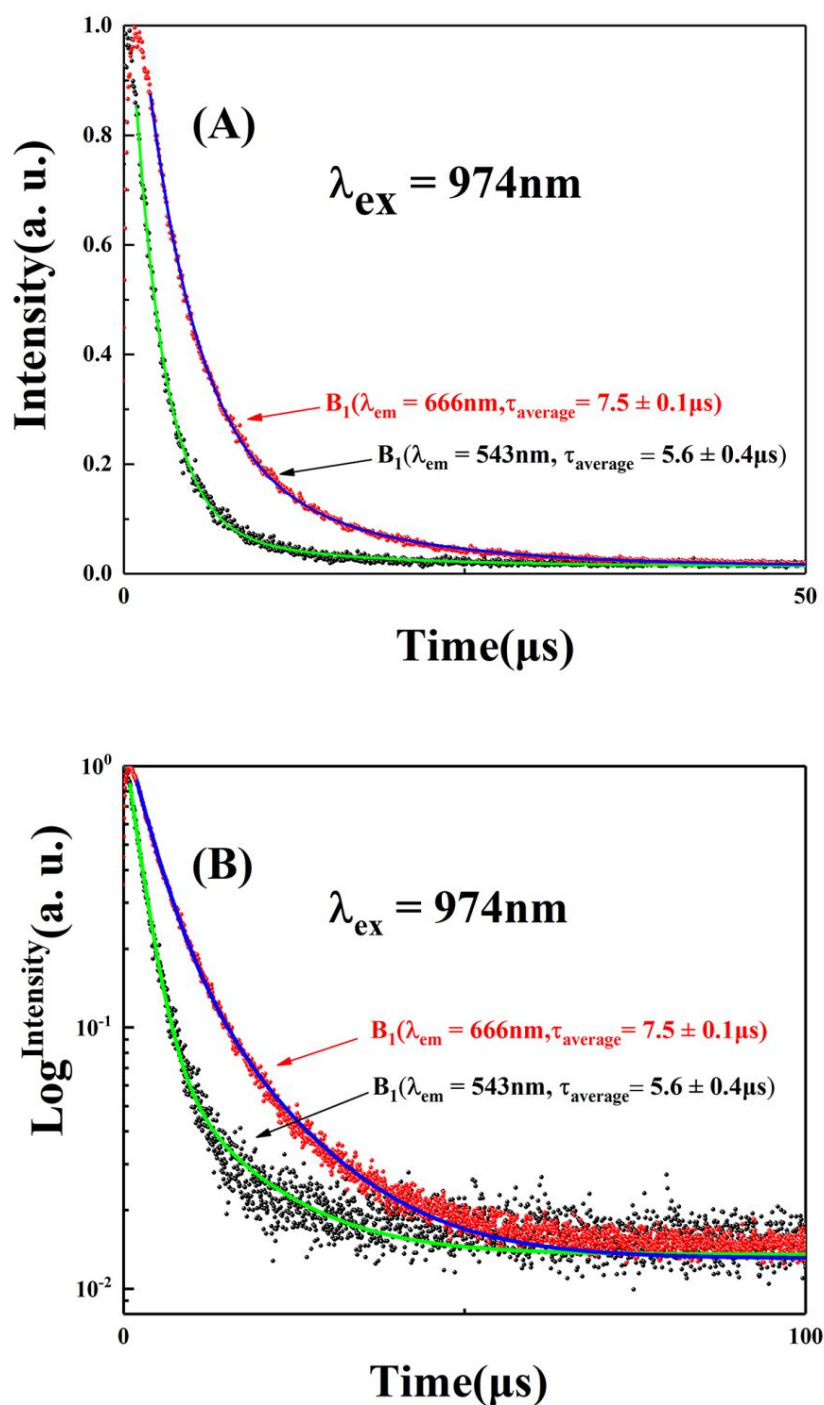


Figure 3.1.13 The decay curve of B_1 at 543 nm (${}^4S_{3/2} \rightarrow {}^4I_{15/2}$) and 666 nm (${}^4F_{9/2} \rightarrow {}^4I_{15/2}$) under 974 nm pulsed excitation laser with different y-axis (A) linear y-axis and (B) logarithmic y-axis.

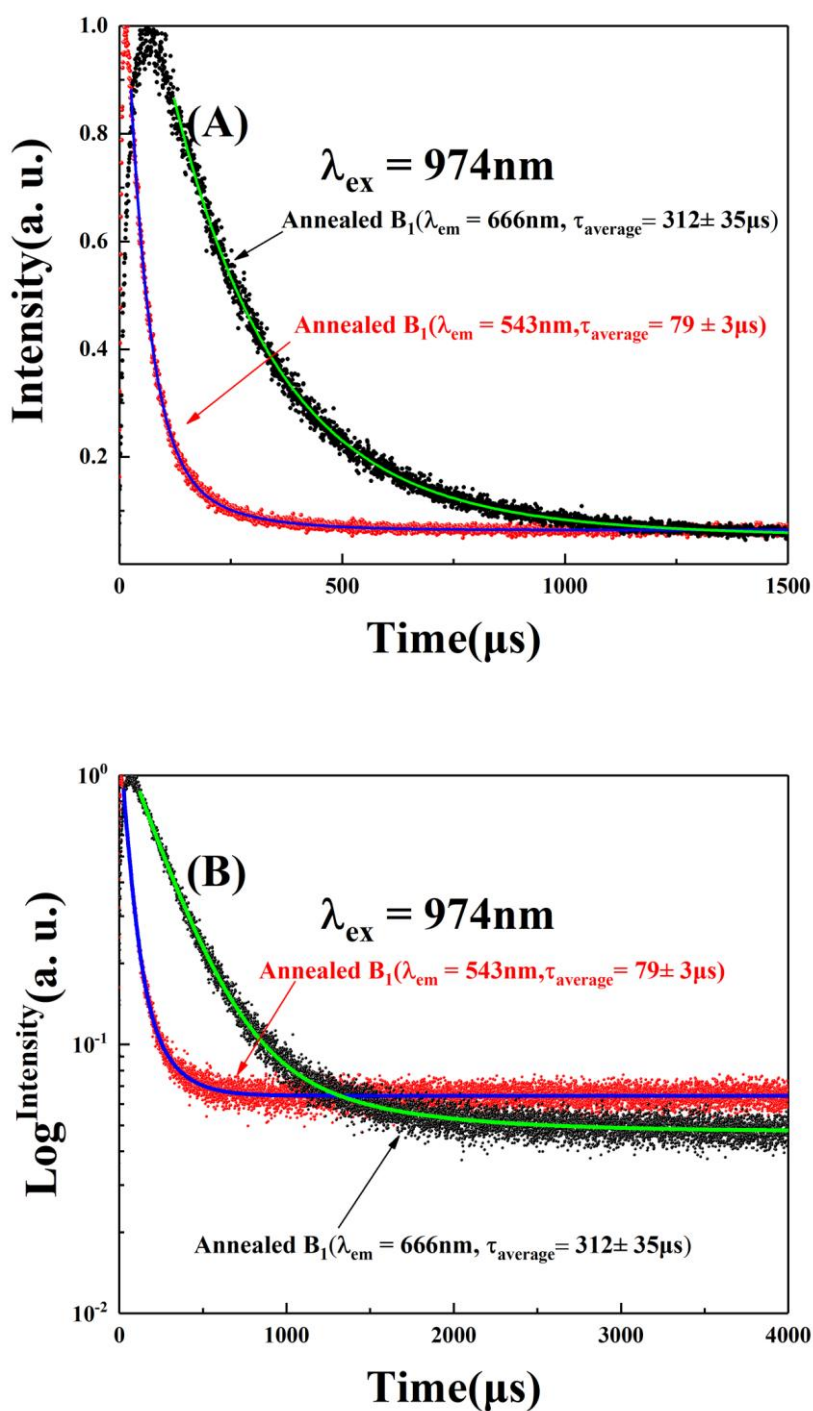


Figure 3.1.14 The decay curve of annealed B₁ at 543 nm (⁴S_{3/2} → ⁴I_{15/2}) and 666 nm (⁴F_{9/2} → ⁴I_{15/2}) under 974 nm pulsed excitation laser with different y-axis (A) linear y-axis and (B) logarithmic y-axis.

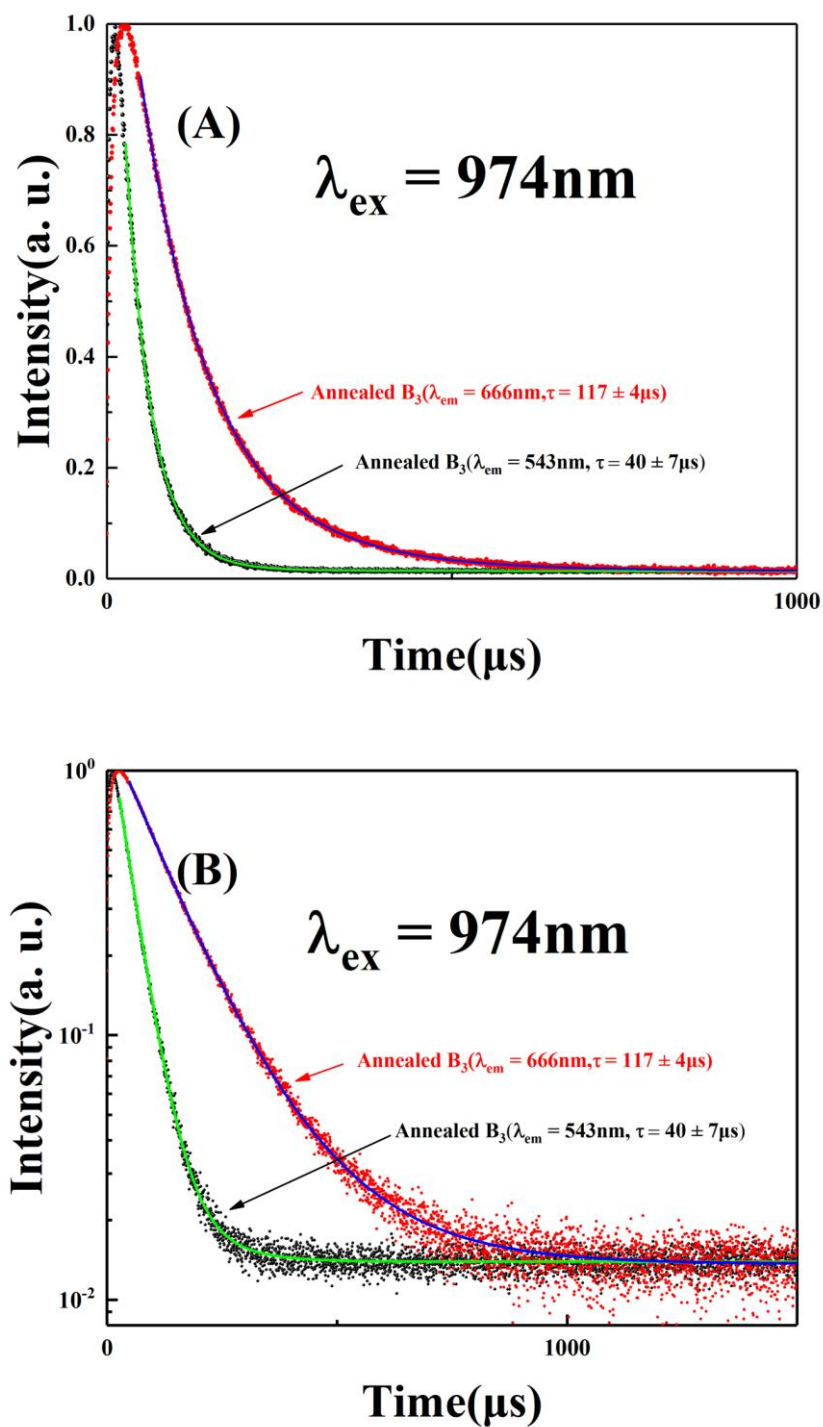


Figure 3.1.15 The decay curve of annealed B_3 at 543 nm (${}^4\text{S}_{3/2} \rightarrow {}^4\text{I}_{15/2}$) and 666 nm (${}^4\text{F}_{9/2} \rightarrow {}^4\text{I}_{15/2}$) under 974 nm pulsed excitation laser with different y-axis (A) linear y-axis and (B) logarithmic y-axis.

Chapter 3 Results and discussion

Figure 3.1.12 displays the decay curve of sample A₁ at 543 nm ($^4S_{3/2} \rightarrow ^4I_{15/2}$) and 666 nm ($^4F_{9/2} \rightarrow ^4I_{15/2}$) under a 974 nm excitation laser. Figure 3.1.13 and Figure 3.1.14 illustrate the decay curves of sample B₁ before annealing and after annealing treatment, respectively. Figure 3.1.15 shows the decay curves of the annealed B₃. In addition, only the decay curves of annealed B₃ are fitted well with single exponential function and others are well fitted with double exponential function. The decay times of A₁ and B₁ at 543 nm are 3 μ s and 6 μ s, respectively. The decay times of A₁ and B₁ at 666 nm are 6 μ s and 8 μ s, respectively. The B₁ compound shows a slightly longer lifetime than the A₁ sample.

For sample B₁, the annealing treatment shows a remarkable effect to increase the lifetime from 6 μ s to 79 μ s at 543 nm and 8 μ s to 312 μ s at 666 nm. Such large enhancement is due to the annealing process that removes the residual ligands onto the particles (such as NO³⁻ and OH⁻ groups sourced from reagents) which are known to quench the radiative procedure of Yb³⁺/Er³⁺ to decrease the up-conversion efficiency.⁶⁰ A few works in the literature reported the lifetime of KYF₄-based up-conversion nanocrystal, such as KYF₄:Nd,¹⁶⁴ KYF₄:Eu,¹⁶⁵ and KYF₄:Eu.¹⁶⁶ Here, we example hexagonal NaYF₄:Yb³⁺/Er³⁺,^{18,23,63,170} which has been recognized to own the highest efficiency currently, to compare. The lifetimes of hexagonal NaYF₄:Yb³⁺/Er³⁺ (29 -32 nm) are $\tau = 81 \mu$ s for the green wavelengths and $\tau = 296 \mu$ s for the red wavelengths.⁶³ The details are collected in Table 3.1.5.

Chapter 3 Results and discussion

Table 3.1.5 The photoluminescence decay times from prepared KYF₄-based samples and reported NaYF₄-based samples.⁶³

Samples	Decay time at 543 nm (μ s)	Decay time at 666nm (μ s)
A₁	3.0 \pm 0.1	5.7 \pm 0.1
A₂	3.5 \pm 0.1	3.6 \pm 0.1
A₃	2.2 \pm 0.1	3.1 \pm 0.9
B₁	5.6 \pm 0.4	7.5 \pm 0.1
B₁-T	79 \pm 3	312 \pm 35
B₂	2.5 \pm 0.1	3.8 \pm 0.1
B₃	NG	1.8 \pm 0.4
B₃-T	40 \pm 7	117 \pm 4.
β-NaYF₄:Yb³⁺/Er³⁺	81	296

Note: B₁-T stands for the annealed sample B₁ and B₃-T stands for the annealed sample B₃.

Table 3.1.5 gives the decay times of the prepared samples and literature. It is obvious that the B₁-T sample possesses the longest photoluminescence lifetimes at both 543 nm and 666 nm in prepared compounds. After annealing treatment, the lifetime of B₁ get a very large improvement, which is comparable with literature β -NaYF₄:Yb³⁺/Er³⁺.²³ It is also a shred of evidence that B₁ sample has high up-conversion efficiency.

In addition, the effect of nanoparticle size on the lifetimes can be analyzed from Table 3.1.1 and Table 3.1.5. For B series samples, the B₁ sample has relatively larger nanoparticles compared with that of B₂ and B₃. It possesses the longest lifetime as

Chapter 3 Results and discussion

well. The large nanoparticles for the same UCNs indeed have longer lifetime.

3.1.4 Conclusion

In this part, the results and discussion of Yb/Er co-doped KYF₄ UCNs have been presented. At first, the water-ethanol mixture solvent was found to be necessary for obtaining the pure cubic KYF₄ phase. The calculated mean crystallite sizes are in good accordance with the size distribution from TEM images. The B series samples, especial B₁, show good morphology. The B₁ sample was found to possess the highest photoluminescence intensity at both green or red light. The excellent long lifetimes, 79 μ s at 543 nm and 312 μ s at 666 nm, belonged to the annealed B₁ sample. These desirable properties make B₁ compound has promising potential in application candidate. The internal QY of B₁ samples is 0.20 % at 543 nm and is 0.14 % at 666 nm. The effects of nanoparticle size on lifetime has also been discussed.

Chapter 3 Results and discussion

3.2 BiF₃:10%Yb/5%Er

Most of the reported fluoride hosts include lanthanide ions, which leads to the high cost and limitation of application in vivo. Therefore, novel fluoride-based matrices, which are cheap and non-toxic, are imperative. Among the heavy metal like fluorides, BiF₃ is the only one that is environmental-friendly. Meanwhile, BiF₃ features good substitution by trivalent lanthanide ions.¹³⁴ Because the Shannon ionic radius of Bi³⁺ is close to many lanthanide ions. Bismuth fluoride has two different phase structure including cubic α -BiF₃ fluorite-based structure (space group Fm-3m) and β -BiF₃ with orthorhombic (space group Pnma) structure.

The bismuth fluoride UCNs take advantages of non-toxicity, low cost, and easy substitution by lanthanide ions, which make it have potential applications in drug delivery and bioimaging. However, only very few reports concerning bismuth fluorides.^{134,135,171,172} In this chapter, the undoped and Yb/Er co-doped BiF₃ will be prepared and characterised. The related results will be discussed.

3.2.1 Structure

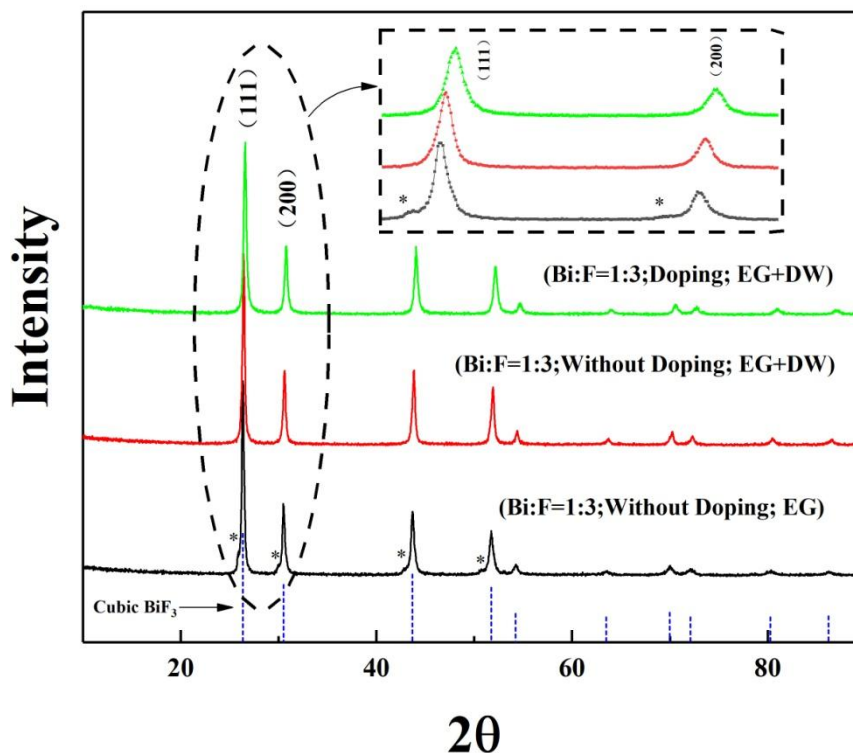


Figure 3.2.1 The X-ray powder diffraction patterns in black curve, BiF₃ compounds prepared in ethylene glycol under initial Bi/F=1/3 ratio; red curve, BiF₃ compounds prepared in a mixture of ethylene glycol and deionized water under initial Bi/F=1/3 ratio; and green curve, Yb/Er co-doped BiF₃ compounds synthesized in ethylene glycol and deionized water under initial Bi/F=1/3 ratio. The dotted lines stand for the cubic BiF₃ of literature (space group Fm-3m, PDF 00-051-0944).

Figure 3.2.1 illustrates XRD patterns of three BiF₃ compounds that were synthesized under the same initial Bi/F=1/3 ratio in ethylene glycol (black curve), in the mixture of ethylene glycol and deionized water (red curve), and Yb/Er co-doped BiF₃ in the mixture of ethylene glycol and deionized water (green curve). The vertical dotted line represents the cubic BiF₃ structure (space group Fm-3m, PDF 00-051-0944) of

Chapter 3 Results and discussion

literature. The phase of all the prepared samples is in good agreement with the cubic BiF_3 phase structure of literature.

However, the BiF_3 compounds synthesized in only ethylene glycol solvent (black curve) display some impure peaks marked by asterisks in Figure 3.2.1. The compounds, plotted by the red curve, prepared in the mixture of ethylene glycol and deionized water exhibits pure cubic phase of BiF_3 compound without any impure peaks. The difference results from the use of different solvents. $\text{Bi}(\text{NO}_3)_3 \cdot 6\text{H}_2\text{O}$ is insoluble in deionized water and ethanol at RT, but can easily dissolve into ethylene glycol at RT. Therefore, the ethylene glycol was used as the solvent to dissolve the nitrate reactants. NH_4F , which provides the source of F^- anion, easily dissolves into deionized water but hardly into ethylene glycol at room temperature. The impurity peaks may result from the bad solubility of NH_4F in the ethylene glycol. After analysis of XRD patterns of these two compounds, it is noteworthy that the mixed medium of ethylene glycol (dissolving nitrate) and deionized water (dissolving NH_4F) are essential to avoid introducing miscellaneous in present work.

After careful comparison of X-ray diffraction patterns of undoped (drawn with red curve) and Yb/Er co-doped (drawn with green curve) compounds, the peaks position move to high angle after co-doping Yb/Er into BiF_3 compounds. For effortless discrimination, the inset of the enlarged first two peaks (111) and (200) are plotted in the top of Figure 3.2.1. The observed peak position of (111) and (200) indeed move to large angle, which indicates at least one of the smaller Yb^{3+} or Er^{3+} or both of them have been introduced into BiF_3 matrix lattice successfully. Because Shannon ionic radius of Bi^{3+} , Yb^{3+} , and Er^{3+} with VIII coordination is 1.31 Å, 1.125 Å, and 1.144 Å, respectively.^{115,168} Shannon ionic radius of Yb^{3+} and Er^{3+} are smaller than that of Bi^{3+} .

Chapter 3 Results and discussion

On condition that Yb^{3+} and Er^{3+} ions were introduced into the BiF_3 lattice successfully, the parameter of the matrix will become smaller. It implies the position of the peaks should move to high angle.

Figure 3.2.2 gives the XRD patterns of BiF_3 samples prepared under different Bi/F ratios of initial addition, including 1/3 (marked with A), 1/5 (marked with B), and 1/7 (marked with C). Figure 3.2.3 exhibits the XRD patterns of Yb/Er co-doped BiF_3 compounds synthesized under different initial Bi/F ratios, including 1/3 (marked with D), 1/5 (marked with E), and 1/7 (marked with F). All the compounds are in good accordance with the cubic BiF_3 without any trace of impurity phase. It has no doubts that the BiF_3 compounds have been successfully synthesized at room temperature via co-precipitation approach in the mixture of ethylene glycol and deionized water solvents.

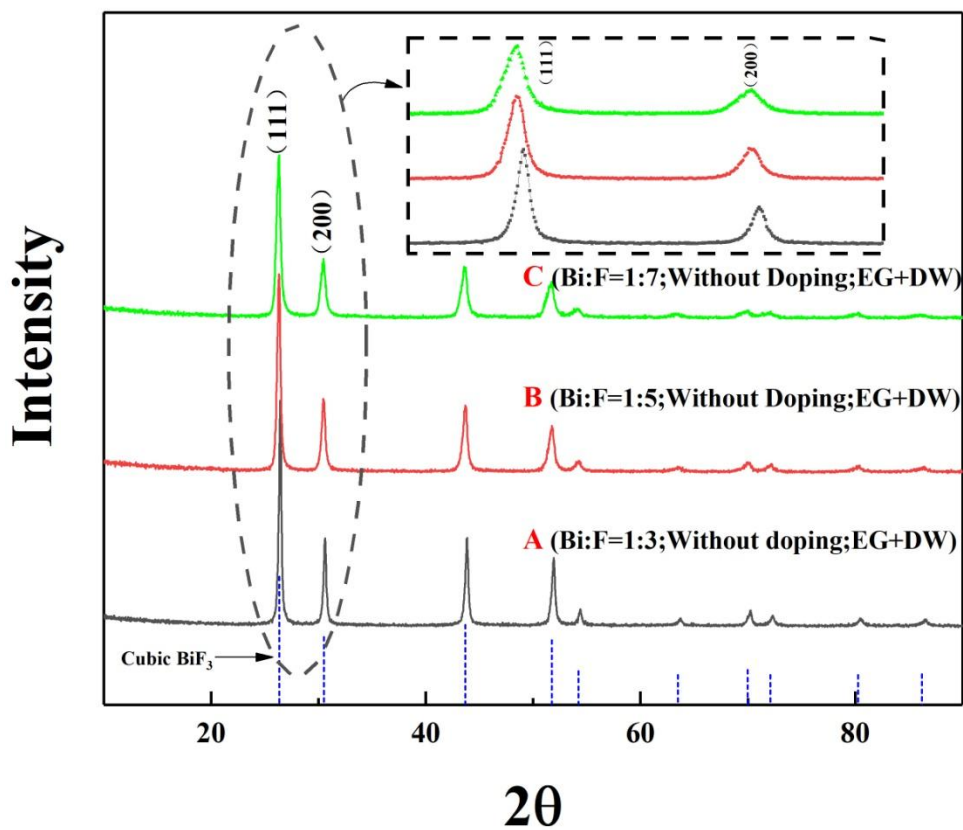


Figure 3.2.2 X-ray powder diffractions of BiF₃ compounds prepared with different initial Bi/F ratios, including A (black curve): Bi/F= 1/3; B (red curve): Bi/F=1/5 and C (green curve): Bi/F=1/7. The dotted lines stand for the cubic BiF₃ of literature (space group Fm-3m, PDF 00-051-0944).

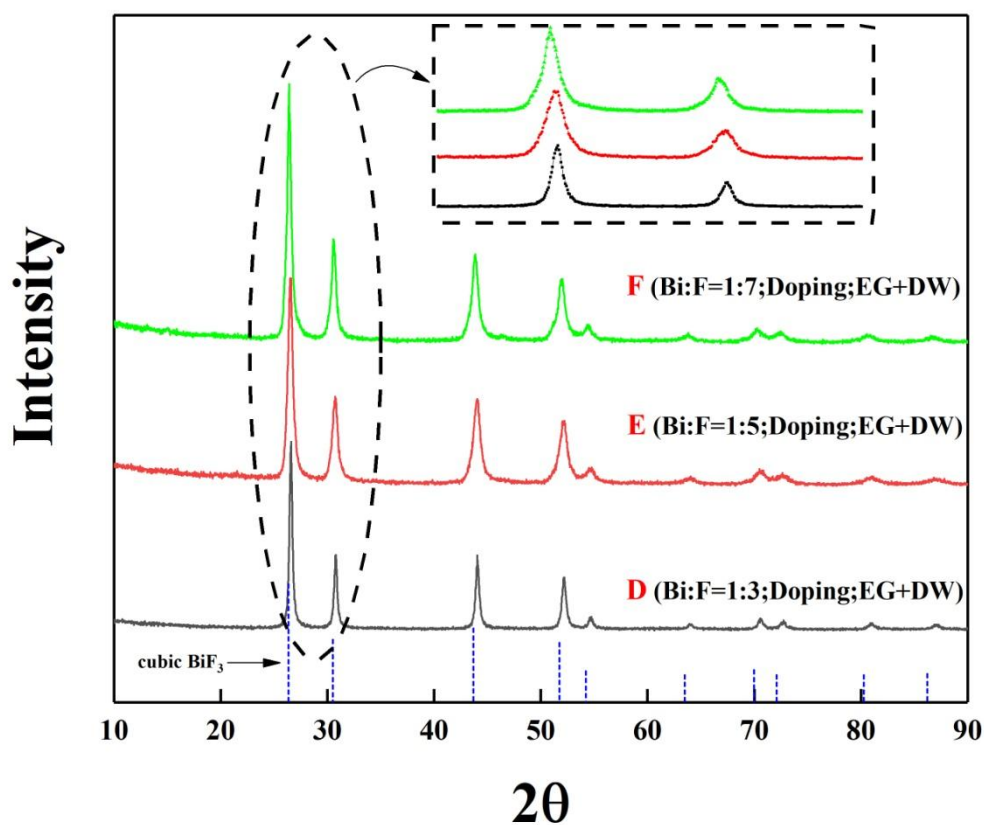


Figure 3.2.3 X-ray powder diffractions of prepared Yb/Er co-doped BiF_3 compounds with different initial Bi/F ratios, including D (black curve): Bi/F = 1/3; E (red curve): Bi/F = 1/5; and F (green curve): Bi/F = 1/7. The dotted line stands for the cubic BiF_3 of literature (space group Fm-3m, PDF 00-051-0944).

The different additions of initial Bi/F ratio result in slight shift of the position of the peaks. In both undoped and Yb/Er co-doped BiF_3 compounds, the increase of the initial addition amounts of F^- results in the left shift of the position of the peaks. The position of the peaks moves to a low angle, which means the lattice parameter increase. This change tendency can easily be observed from the two peaks (111) and (200) in the top inset of Figure 3.2.2 and Figure 3.2.3. It is very clear the positions of (111) and (200) peaks move towards low angle with increasing F^- amounts. Large F^-

Chapter 3 Results and discussion

concentrations may provide enough negative ions to allow the sufficient nucleation and growth of BiF_3 lattice.

In summary, in a large range of Bi/F ratios of the initial adding, the cubic BiF_3 samples can be successfully synthesized via a co-precipitation method at room temperature. The mixed solvents of ethylene glycol and deionized water are essential to help obtaining BiF_3 compounds with pure cubic phase structure. The increase of the initial addition of F^- amounts result in the weak shift of the peaks.

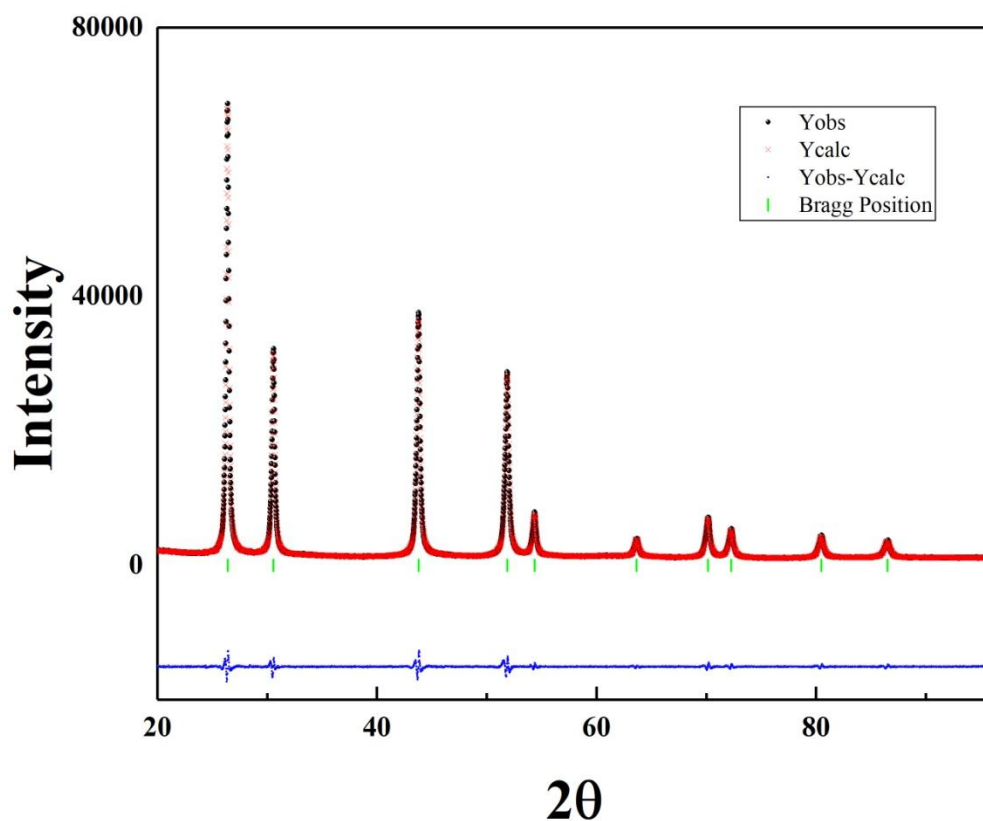


Figure 3.2.4 The profile fitting of X-ray powder diffraction pattern of sample A, which is undoped BiF_3 compound synthesized in a Bi/F = 1/3 ratio, under a slow scanning speed

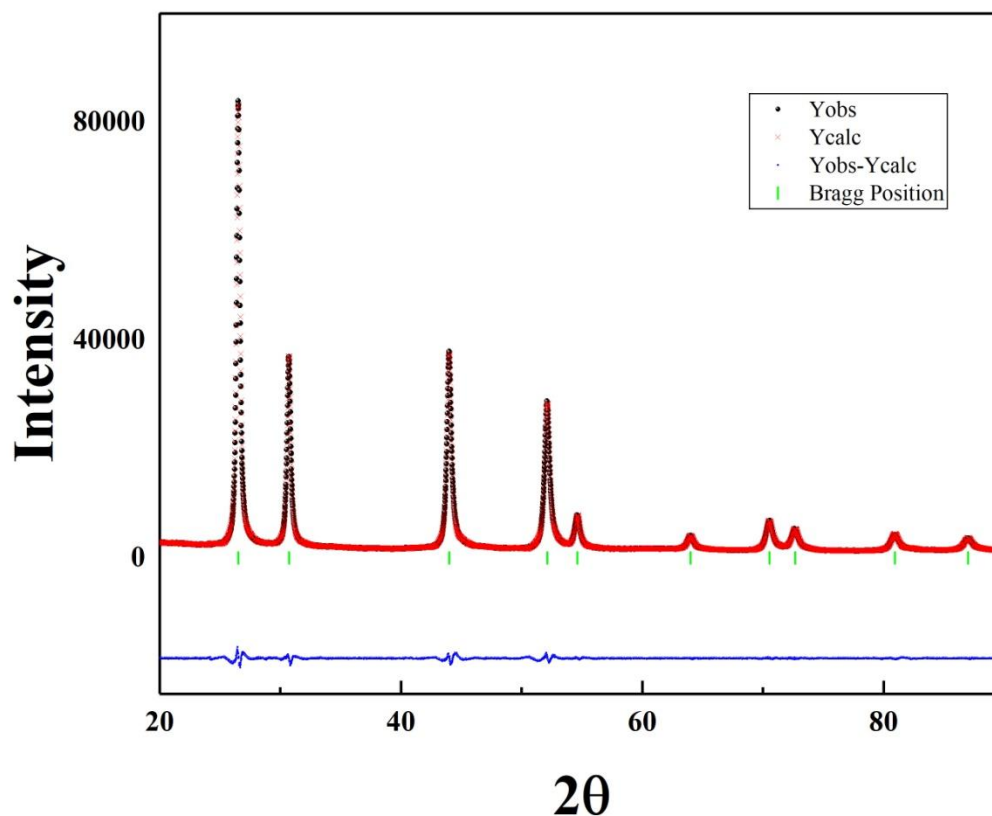


Figure 3.2.5 The profile fitting of the X-ray powder diffraction of sample D, which is Yb/Er co-doped BiF_3 compound prepared in a $\text{Bi}/\text{F} = 1/3$ ratio, under a slow scanning speed.

In order to analyze the change tendency of lattice parameter accurately, the XRD experimental data of sample A and D were fitted to calculate the lattice parameter of matrix BiF_3 with FullProf Suite software. The profile fitting results of A and D are shown in Figure 3.2.4 and Figure 3.2.5, respectively. The obtained X-ray diffraction experimental data of sample A and D, under slow scanning speed, exhibit high accumulating intensity in Figure 3.2.4 and Figure 3.2.5, respectively. They are expected to have a high degree of crystallinity.

It is obvious that the fitting results match well with the experimental curves and the

Chapter 3 Results and discussion

calculated lattice parameter of A and D is 5.8423 Å and 5.8148 Å, respectively. The lattice parameter of sample D is indeed smaller than that of sample A and also than the BiF₃ compounds of literature PDF 00-051-0944 (5.8559 Å). Sample D has a small lattice parameter 5.8148 Å, because some small Yb³⁺ and Er³⁺ ions were introduced into matrix lattice that substitutes the big Bi³⁺ ions. The articles about BiF₃-based UCNs are scarce. The lattice parameter 5.8423 Å of the presented undoped BiF₃ is as well similar to the one of the reported lattice parameter 5.84223 Å.¹³⁴

Chapter 3 Results and discussion

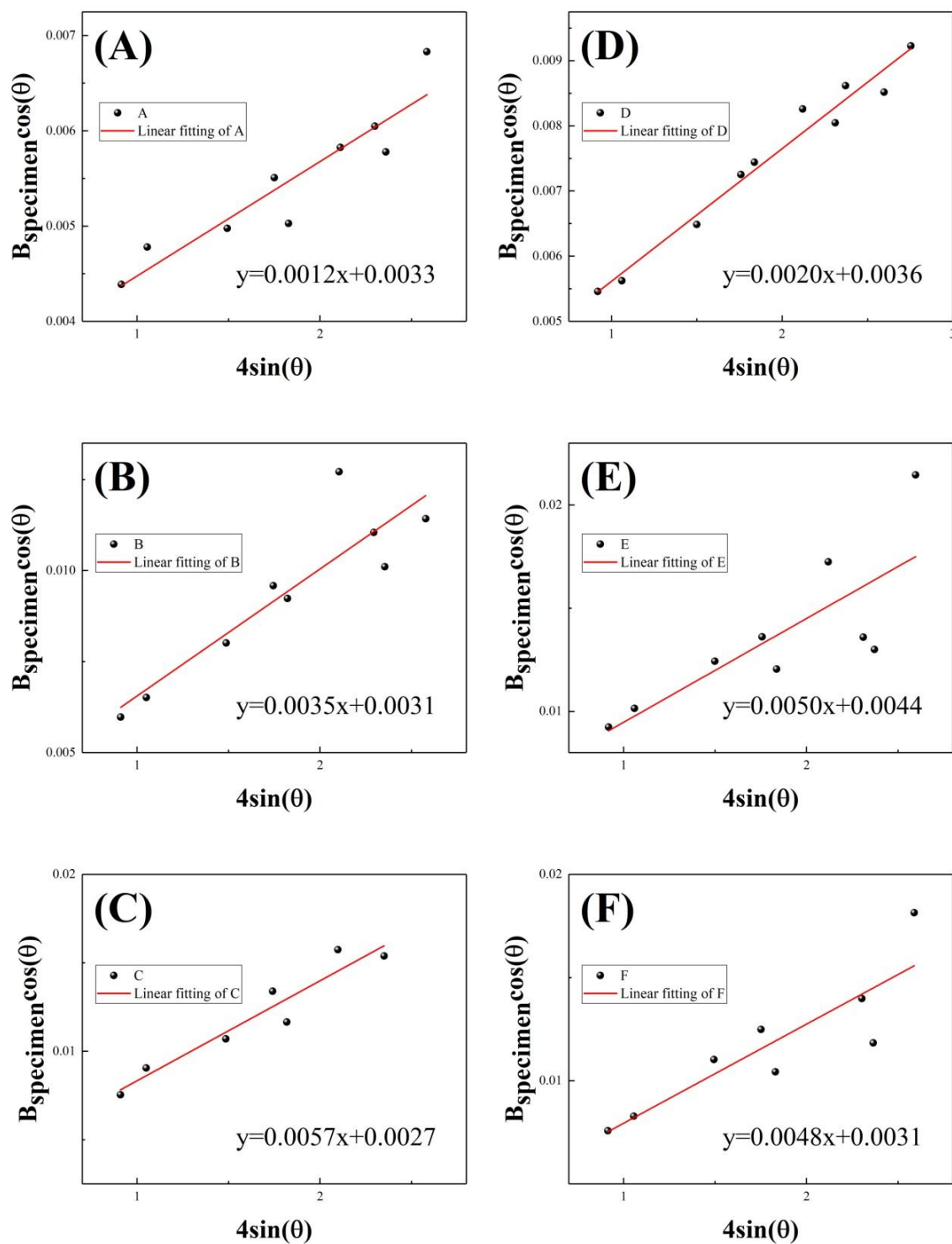


Figure 3.2.6 Linear fitting curves of $B_{\text{sample}} \cos(\theta)$ with respects to $4 \sin(\theta)$ of the sample A, B, C, D, E, and F marked with (A), (B), (C), (D), (E), and (F), respectively.

According to a modified Scherer Equation based on Williamson-Hall methods,

Chapter 3 Results and discussion

Figure 3.2.6 gives the linear fitting curves of $B_{specimen} \cos(\theta)$ with respect to $4 \sin(\theta)$ to calculate the mean crystallite size. The peaks (111), (200), (220), (311), (222), (400), (331), (420), and (422) were used to calculate by the final equation $B_{specimen} \cos(\theta) = 4 \varepsilon \sin(\theta) + k\lambda/D$. The slope and y-intercept of the fitted lines stand for strain effect and size effect, respectively. The results were collected in Table 3.2.1.

Table 3.2.1 The calculated $Y_{intercept}$ (including the standard error), mean crystallite size D , and microstrain ε .

Samples	$Y_{intercept} (\times 10^{-3})$	Mean crystallite size D	Microstrain ε (%)
A	3.3 ± 0.3	43 ± 4 nm	0.12 ± 0.02
B	3.1 ± 1.2	46 ± 13 nm	0.35 ± 0.06
C	2.7 ± 1.3	53 ± 18 nm	0.57 ± 0.07
D	3.6 ± 0.3	40 ± 3 nm	0.20 ± 0.01
E	4.4 ± 2.8	32 ± 12 nm	0.50 ± 0.15
F	3.1 ± 2.0	45 ± 18 nm	0.48 ± 0.11

Table 3.2.1 gathered the calculated $Y_{intercept}$, including the standard error, calculated mean crystallite size D , and microstrain ε . Samples A and D, synthesized under initial Bi/F = 1/3 ratios, exhibit relatively low standard errors (0.34 and 0.25, respectively) that are less than 1.

As predicted, the mean crystallite size of Yb/Er doped BiF₃ is smaller than that of the undoped BiF₃ compound. For example, in comparison of the mean crystallite size of sample A (undoped nanoparticles prepared under Bi/F = 1/3) and sample D (Yb/Er co-doped UCNs prepared under Bi/F = 1/3), the 43 ± 4 nm mean crystallite size of

sample A is larger than that of the sample D 40 ± 3 nm.

3.2.2 Morphology

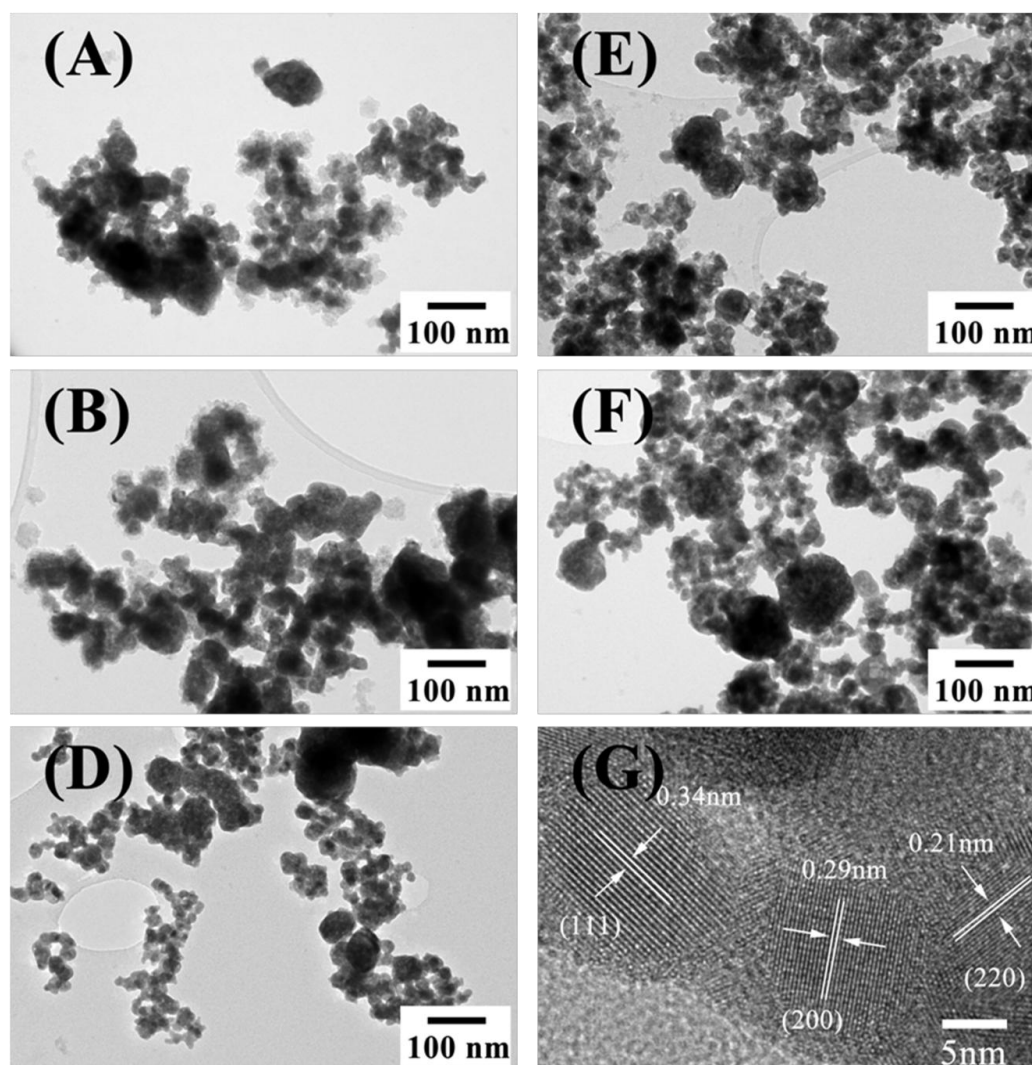


Figure 3.2.7 Transmission electron microscope (TEM) photographs of: (A) sample A, undoped BiF_3 in initial $\text{Bi}/\text{F} = 1/3$ ratio; (B) sample B, undoped BiF_3 in initial $\text{Bi}/\text{F} = 1/5$ ratio; (D) sample D, Yb/Er co-doped BiF_3 in initial $\text{Bi}/\text{F} = 1/3$ ratio; (E) sample E, Yb/Er co-doped BiF_3 in initial $\text{Bi}/\text{F} = 1/5$ ratio; (F) sample F, Yb/Er co-doped BiF_3 in initial $\text{Bi}/\text{F} = 1/7$ ratio; and (G) sample D, undoped BiF_3 in initial $\text{Bi}/\text{F} = 1/3$ ratio in 600,000X.

Chapter 3 Results and discussion

Figure 3.2.7 illustrates the 30,000X transmission electron microscope (TEM) photographs of sample A, B, D, E, and F, recorded as (A), (B), (D), (E), and (F), respectively. Figure 3.2.7(G) shows the 600,000 X microscope photograph of sample D.

Most of the nanoparticles are near to sphere shape. The boundary of all the nanoparticles is indistinct, which is especially worse in Figure 3.2.7(A) and (B). There are some small nanoparticles locate onto the large nanoparticles boundary in sample A and sample B. In comparison to undoped BiF_3 compounds (Figure 3.2.7(A) and (B)), samples (Figure 3.2.7(D), (E), and (F)) co-doped with Yb/Er show relatively clear boundary. Nevertheless, the nanoparticle size distributions of B, C, D, and E samples are very broad (Figure 3.2.8). For example, a few noticeably large nanoparticles are more than 100 nm while the small ones are near to 10 nm in Figure 3.2.7(F). It is due to the drawback of the co-precipitation method at room temperature, for which the size and shape of the nanoparticles is difficult to control. It is not only the drawback of co-precipitation but also other synthesis routes.

Three different lattice fringes are marked in Figure 3.2.7(G), the observed 0.34 nm is corresponding to (111),¹⁷² 0.29 nm is corresponding to (200),¹³⁴ and 0.21 nm is corresponding to (220)¹⁷³ lattice plane of BiF_3 .

Figure 3.2.8 illustrates the statistics histograms of the prepared BiF_3 up-conversion nanoparticles from TEM photographs. Table 3.2.2 collected the nanoparticle size distribution from TEM images and mean crystallite size from XRD patterns. All the standard deviations of the size distribution are large. The range of nanoparticle size distribution of all the prepared samples is large.

Chapter 3 Results and discussion

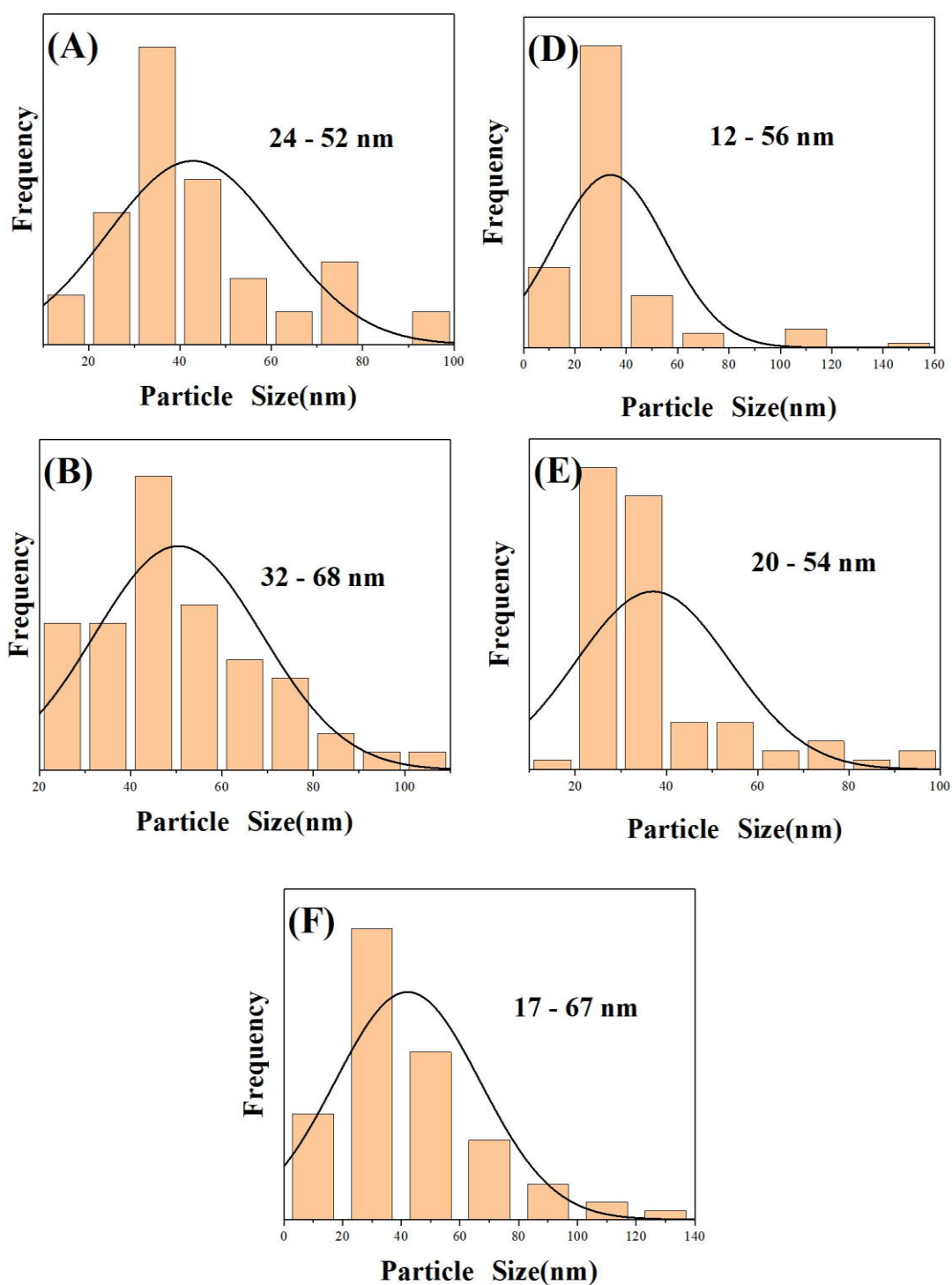


Figure 3.2.8 The statistics histograms of samples A, B, D, E, and F from TEM photographs (80 – 100 nanoparticles).

Chapter 3 Results and discussion

Table 3.2.2 The nanoparticle size distribution from TEM photographs and the calculated mean crystallite size from XRD patterns.

Samples	Nanoparticle size distribution from TEM	Mean crystallite size D from XRD
A	24 - 52 nm	43 ± 4 nm
B	32 - 68 nm	46 ± 13 nm
C	NG	53 ± 18 nm
D	12 - 56 nm	40 ± 3 nm
E	20 - 54 nm	32 ± 12 nm
F	17 - 67 nm	45 ± 18 nm

3.2.3 Photoluminescence properties

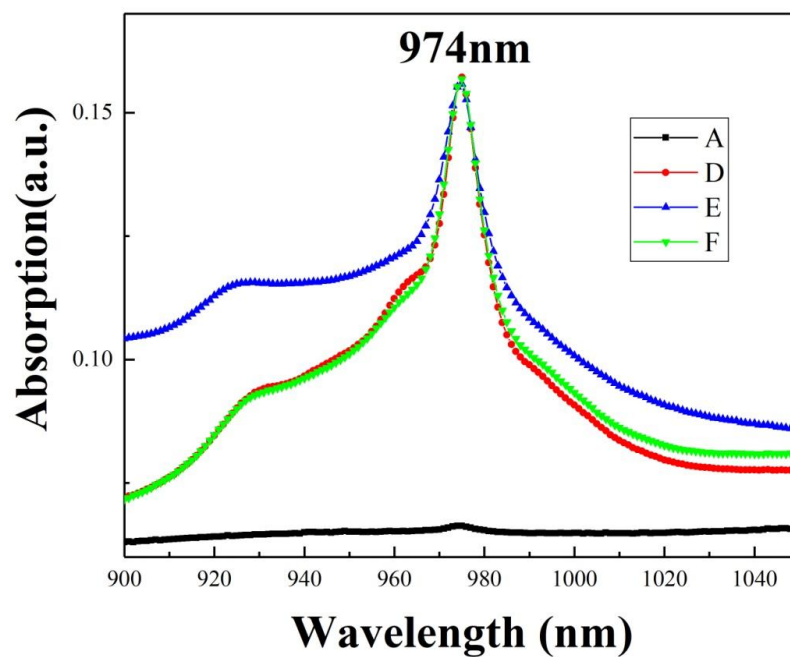


Figure 3.2.9 Absolute absorption spectra of sample A, D, E, and F from 900 nm to

Chapter 3 Results and discussion

1050 nm.

Figure 3.2.9 exhibits the absolute absorption spectra of the prepared samples A, D, E, and F from 900 nm to 1050 nm. As predicted, there is no absorption peak in the absolute absorption spectra of undoped A sample. However, the prepared Yb/Er co-doped samples D, E, and F samples exhibit obvious absorption peaks at 974 nm.

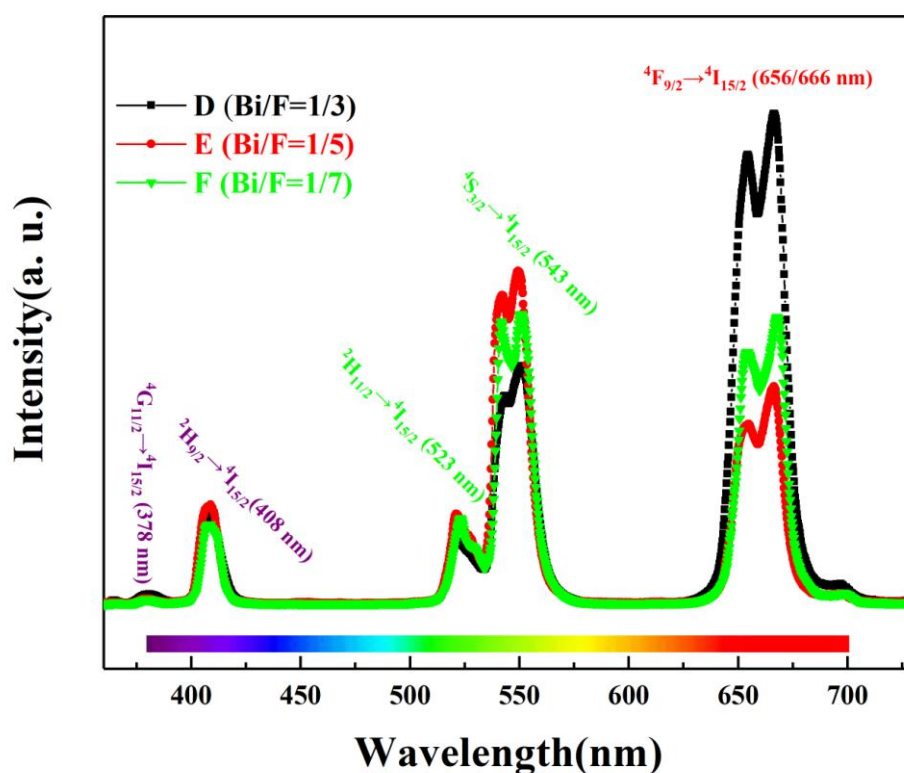


Figure 3.2.10 The emission spectra of the Yb/Er co-doped BiF_3 samples D (Bi/F = 1/3), E (Bi/F = 1/5), and F (Bi/F = 1/7).

Figure 3.2.10 illustrates the emission spectra of Yb/Er co-doped BiF_3 UCNs with different initial Bi/F ratio under 974 nm pulsed laser excitation. The powder samples are directly excited without any further modification. It is obvious that the characteristic emission peaks of Yb/Er at 523 nm, 543 nm, and 656 nm/666 nm which

Chapter 3 Results and discussion

is corresponding to $^2H_{11/2} \rightarrow ^4I_{15/2}$, $^4S_{3/2} \rightarrow ^4I_{15/2}$, and $^4F_{9/2} \rightarrow ^4I_{15/2}$ transitions of Er^{3+} , respectively. Apart from these familiar peaks, the two weak peaks at 378 nm and 408 nm are observed as well, which are corresponding to $^4G_{11/2} \rightarrow ^4I_{15/2}$ and $^2H_{9/2} \rightarrow ^4I_{15/2}$ transition of Er^{3+} , respectively.

Table 3.2.3 The relative emitting intensities at 408 nm, 543 nm and 666 nm of the Yb/Er co-doped BiF_3 : D (Bi/F = 1/3), E (Bi/F = 1/3), and F (Bi/F = 1/3).

Samples	Relative Emitting Intensity at 408 nm	Relative Emitting Intensity at 543 nm	Relative Emitting Intensity at 666 nm
D	1.3	3.2	7.5
E	1.5	4.6	3.3
F	1.2	4.0	4.1

Table 3.2.3 collected the relative emitting intensities at 408 nm, 543 nm, and 666 nm. Sample E has the strongest emitting intensity at 408 nm and 543 nm. However, at 666 nm, D sample shows the highest emitting intensity.

Table 3.2.4 The internal quantum yield of the annealed sample E at 543 nm and at 666 nm.

Sample	Internal quantum yield of green emission light (centred at 543 nm) (%)	Internal quantum yield of red emission light (centred at 666 nm) (%)
E-T	0.13	0.09

Chapter 3 Results and discussion

Table 3.2.4 shows the measured internal quantum yield of annealed E at 543 nm and 666 nm under a ~ 974 nm excitation laser of 1080 mW power. The measured internal QY at 543 nm is 0.13 % and at 666 nm is 0.09 %. The yields are lower than the prepared Yb/Er co-doped KYF₄ UCNs in chapter 3.1.

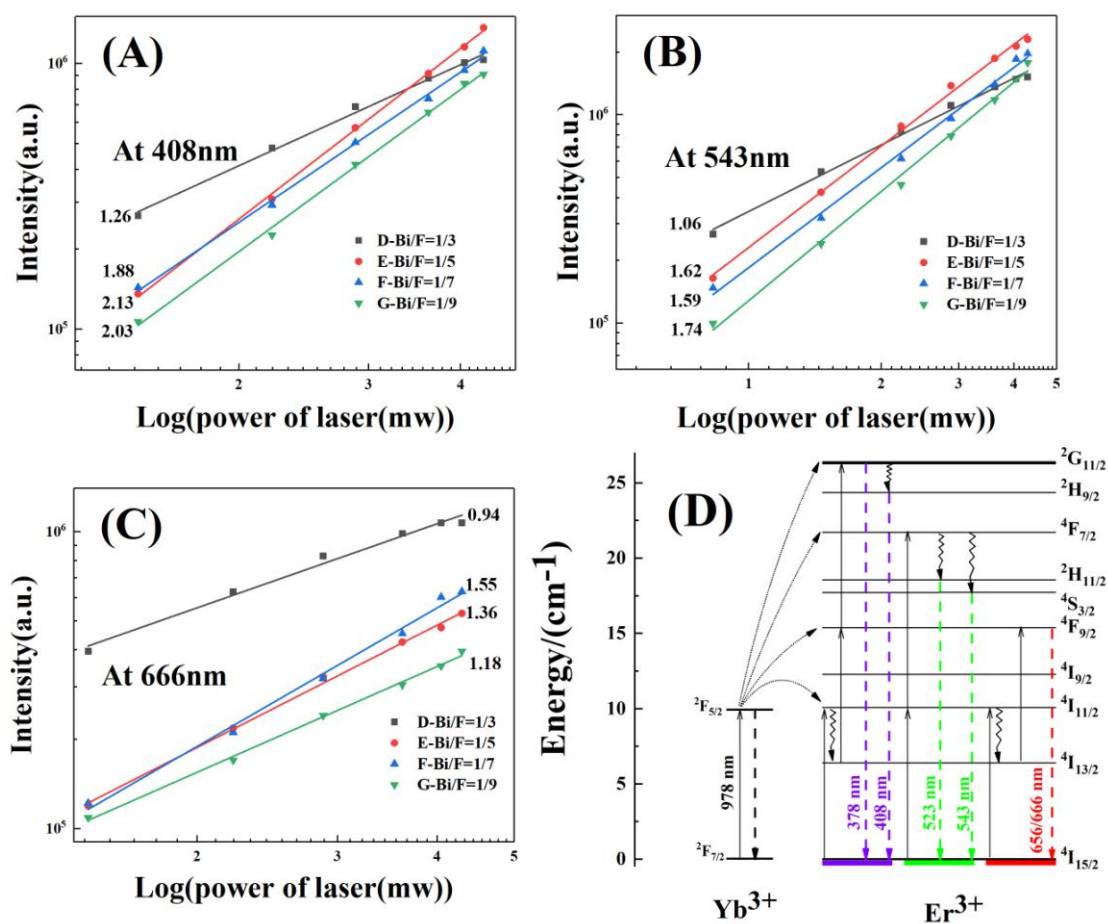


Figure 3.2.11 The log-log fitting plots of emitting light intensity with respect to 974 nm excitation pulsed laser with different energy power of D (Yb/Er co-doped Bi/F₃ under Bi/F = 1/3), E (Yb/Er co-doped Bi/F₃ under Bi/F = 1/5), F (Yb/Er co-doped Bi/F₃ under Bi/F = 1/7), and G (Yb/Er co-doped Bi/F₃ under Bi/F = 1/9) at (A) 408 nm; (B) 543 nm; and (C) 666 nm. (D) The 4f phonon energy levels of Yb³⁺ and Er³⁺.

Chapter 3 Results and discussion

Figure 3.2.11 illustrates the fitted curves of the emission light intensity with respect to the 974 nm exciting pulsed laser with different energy power at 408 nm, 543 nm, and 666 nm.

For 408 nm emitting light, as displayed in Figure 3.2.11(A), the doping Er^{3+} ion on the ground state (Figure 3.2.11(D)) absorbs three 974 nm photons successively to populate the excited $^2\text{H}_{9/2}$ level and then decays to $^4\text{I}_{15/2}$ ground state to emit violet light of 408 nm. With the help of Figure 3.2.11(D), the moving track (in 408 nm emitting) of the Er^{3+} ion can be specified as follows: Firstly, the Er^{3+} ion on ground $^4\text{I}_{15/2}$ state absorbs one photon directly or from transferring by adjacent sensitizer Yb^{3+} to be excited to populate the $^4\text{I}_{11/2}$ level. This ion populating on the $^4\text{I}_{11/2}$ level then decays to the lower $^4\text{I}_{13/2}$ level with a non-radiative relaxation. Afterward, the ion on $^4\text{I}_{13/2}$ level absorbs two photons directly or from Yb^{3+} transferring to populate the $^2\text{G}_{11/2}$ level. And then, it decays to $^2\text{H}_{9/2}$ level with a non-radiative transition.

The above moving track of the Er^{3+} ion reflects the importance of Yb^{3+} ions, which ensures the later photon absorption of Er^{3+} to be further excited on $^2\text{G}_{11/2}$ level. At last, the ion that populating $^2\text{H}_{9/2}$ level sequentially decays to ground state $^4\text{I}_{15/2}$ level in a radiative transition with emission light of 408 nm. The specific energy levels and moving track details can be acquired very clearly from Figure 3.2.11(D), which is marked with arrows.

The processes of generating 543 nm and 666 nm emitting light are different from that of 408 nm. In this case, only two photons were absorbed, which is displayed in the mid and right position of Er^{3+} 4f phonon energy levels in Figure 3.2.11(D), respectively.

The slopes of the fitted curves are supplemental evidence to demonstrate the photon

Chapter 3 Results and discussion

numbers that absorbed by Er^{3+} in the up-conversion process. The slope of the fitted curves 1.26, 2.13, 1.88, and 2.03, in Figure 3.2.11(A) at 408 nm, are all below the theoretical value 3. The slope values of the fitted lines, 1.06, 1.62, 1.59, and 1.62 in Figure 3.2.11(B) at 543 nm and 0.94, 1.55, 1.36, and 1.18 in Figure 3.1.11(C) at 666 nm are all near to theoretical value 2. The gap between the experimental data and the theoretical values is resulted from the competing decay channels depleting the Er^{3+} -state number after the first photon absorption in the $\text{Yb}^{3+}/\text{Er}^{3+}$ couple situation.^{146,162} To be specific, when the ion was excited to populate the $^4\text{I}_{11/2}$ state, it has several possible ways to complete the further UC process for the violet at 408 nm, the green light at 543nm or the red light at 666 nm. It means these three up-conversion processes have a competed relationship about the first-excited ions, which populate the $^4\text{I}_{11/2}$ state.

Chapter 3 Results and discussion

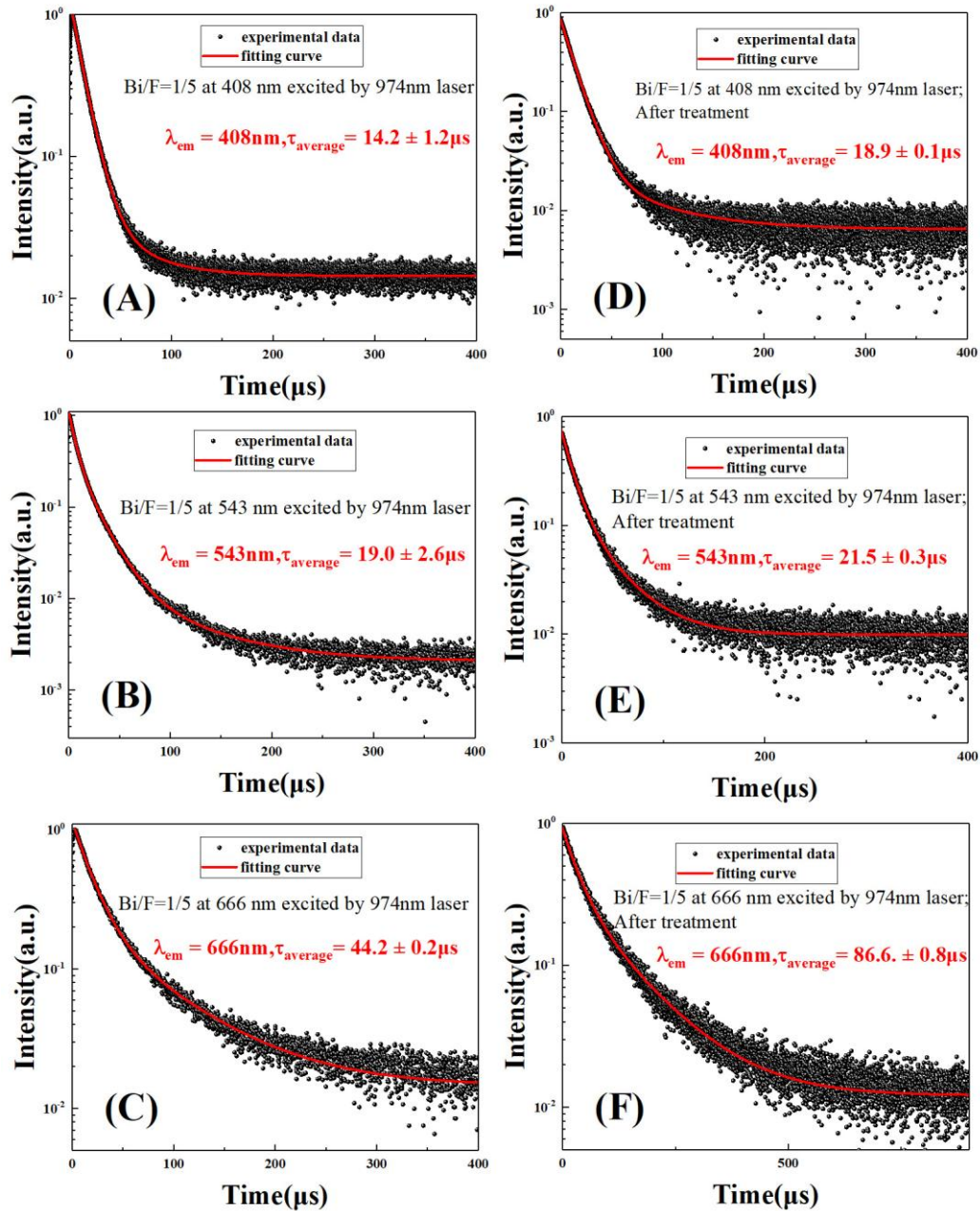


Figure 3.2.12 The decay curves of E sample before and after annealing treatment: (A) at 408 nm before annealing; (B) at 543 nm before annealing; (C) at 666 nm before annealing; (D) at 408 nm after annealing; (E) at 543 nm after annealing; and (F) at 666 nm after annealing.

Figure 3.2.12 exhibits the fitted decay curves of sample E and annealed sample E (Bi/F = 1/5) under 974 nm pulsed excitation laser. The experimental decay data are all

Chapter 3 Results and discussion

fitted well with the double exponential function. The photoluminescence average lifetimes of sample E before annealing at 408 nm, 543 nm, and 666 nm is 14 μ s, 19 μ s, and 44 μ s, respectively. Before annealing, they are longer than that of the prepared Yb/Er co-doped KYF₄ UC compounds in chapter 3.1.

After annealing treatment, the fitted average decay times of sample E increase from 14 to 19 μ s at 408 nm, 19 to 22 μ s at 543 nm, and 44 to 87 μ s at 666 nm. Though the average lifetimes of Yb/Er co-doped BiF₃ is overall longer than that of the prepared Yb/Er co-doped KYF₄ before annealing treatment, the complete average lifetime enhancement of Yb/Er co-doped BiF₃ after annealing treatment is unobvious in comparison with Yb/Er co-doped KYF₄. Only the average lifetime of annealed sample E at 666 nm get a double increase from 44 to 87 μ s. In this case, maybe there are fewer ligands onto the nanoparticles, fewer defects, or less vacancy before the annealing treatment. Therefore, the annealing treatment only removes fewer quenching centers. Or the annealing treatment, used in this compound, needs to be improved to removes more quenching centers. But a suitable reason maybe is the large size distribution and bad morphology.

Chapter 3 Results and discussion

Table 3.2.5 The average lifetimes of prepared sample D (Bi/F = 1/3), E (Bi/F = 1/5), E-T, F (Bi/F = 1/7), and G (Bi/F = 1/9) at 408 nm, 543 nm, and 666 nm.

Samples	Decay time at 408 nm (μ s)	Decay time at 543 nm (μ s)	Decay time at 666 nm (μ s)
D	21.4 ± 0.2	16.1 ± 0.1	62.3 ± 0.1
E	14 ± 1	19 ± 3	44.2 ± 0.2
E-T	18.9 ± 0.1	21.5 ± 0.3	86.6 ± 0.8
F	14.6 ± 0.5	19.1 ± 0.2	42.9 ± 0.2
G	14 ± 1	13.8 ± 0.1	34.3 ± 0.1

Note: E-T stands for the annealed E sample.

Table 3.2.5 gathered the average lifetimes of the prepared sample D, E, E-T, F, and G at 408 nm, 543 nm, and 666 nm. $^4F_{9/2}$ energy state (at 666 nm) has a longer average lifetime than that of $^2H_{9/2}$ (at 408 nm) energy state and $^4S_{3/2}$ energy state (at 666 nm) among all the Yb/Er co-doped samples. Even though the annealing treatment for enhancement of average lifetimes of this compound is unobvious, the overall obtained lifetimes of samples before annealing are still desirable. A suitable treatment method may help remove most of the quench centers to increase the average lifetimes. Some other modifications, such as further research about utilizing of core-shell structure in this compound, may increase its lifetime largely. It is a promising candidate for some application. The size effect on luminescence properties of this compound is unclear due to the broad size distribution.

Chapter 3 Results and discussion

3.2.4 Conclusion

In Chapter 3.2, undoped and 10%Yb/5%Er co-doped cubic BiF₃ nanoparticles were successfully prepared in the mixture medium of ethylene glycol and deionized water. With a fast co-precipitation method at room temperature, different adding amounts of initial Bi/F ratios were designed to synthesize the compounds. However, the prepared samples show a broad nanoparticle size distribution.

The obtained compounds show characteristic emission peaks of Yb/Er co-doped UCNs at 543 nm and 666 nm, excited under a 974 nm pulsed laser. Sample D has the highest efficiency at 666 nm and sample E have relative highest efficiency at 408 nm and 543 nm. Meanwhile, the emitting peaks at 378 nm and 408 nm are also observed. Finally, the average photoluminescence lifetimes were presented. It suggests that sample D have the longest average lifetime at 666 nm and sample E and F show the longest similar lifetime at 408 nm and 543 nm. This result is in agreement with the analysis of emitting intensity. The internal quantum yields of annealed sample E are 0.13 % at 543 nm and 0.09 % at 666 nm.

3.3 $K_{0.3}Bi_{0.7}F_{2.4}:10\%Yb/5\%Er$

As we discussed in Chapter 3.2, bismuth is a “green” element with low cost and non-toxic. Meanwhile, the Shannon ionic radius of Bi^{3+} (1.31 Å, coordination number of VIII) is just slightly greater than many lanthanide ions. If the lanthanide is substituted by bismuth in a matrix of UCNs, it will be an economical and environment-friendly way to prepare UCNs. Besides, the novel bismuth-based matrix of UCNs should have desirable photoluminescence properties.

In some previous reports, the UC luminescence property can be enhanced by Bi^{3+} doping.^{5,174-176} It is a proof for practically using bismuth in the matrix of UCNs. Moreover, we have successfully synthesized Yb/Er co-doped BiF_3 UCNs (in Chapter 3.2). It has been confirmed in the previous work that the BiF_3 nanoparticles are suitable matrix for luminescent ions allowing up-conversion processes.

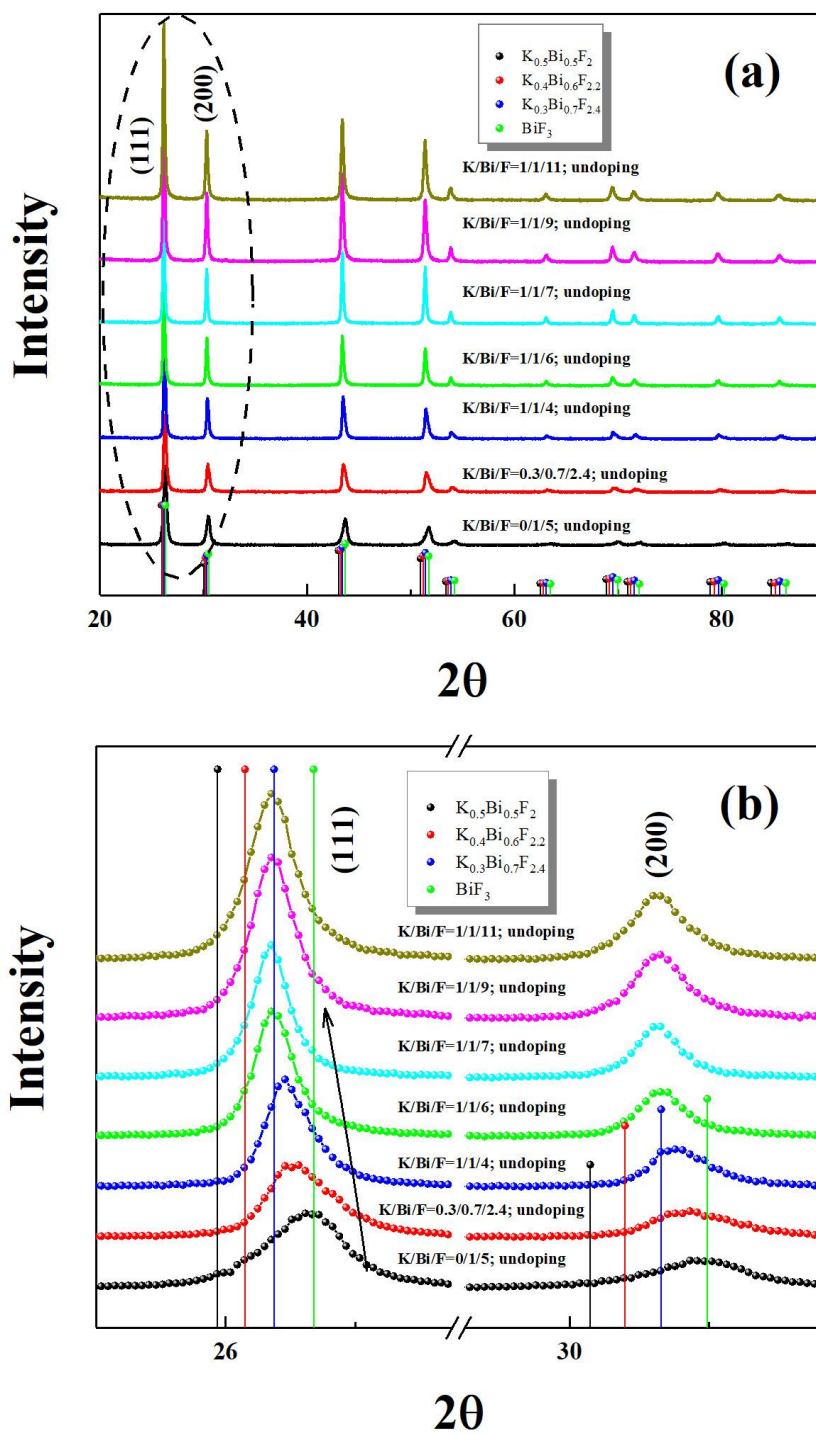
In this chapter, the novel $K_{0.3}Bi_{0.7}F_{2.4}$ nanoparticles and Yb/Er co-doped $K_{0.3}Bi_{0.7}F_{2.4}$ up-conversion nanoparticles will be synthesized. The structure, morphology and photoluminescence properties will be discussed.

3.3.1 Structure

Figure 3.3.1(a) gives the XRD patterns of the prepared undoped $K_{0.3}Bi_{0.7}F_{2.4}$ samples with different initial K/Bi/F ratio, including 0/1/5, 0.3/0.7/2.4, 1/1/4, 1/1/6, 1/1/7, 1/1/9, and 1/1/11. Meanwhile, the literature XRD data of BiF_3 (PDF 04-007-1470), $K_{0.3}Bi_{0.7}F_{2.4}$ (PDF 01-084-0534), $K_{0.4}Bi_{0.6}F_{2.2}$ (PDF 04-012-5861), and $K_{0.5}Bi_{0.5}F_2$ (PDF 04-012-5858) were plotted with the green vertical line, the blue vertical line, the red vertical line, and the black vertical line, respectively. The XRD patterns of cubic

Chapter 3 Results and discussion

BiF_3 and cubic $\text{K}_{1-x}\text{Bi}_x\text{F}_{2x+1}$ family are very close whether in the position of each peak or in the relative intensity of peaks. Therefore, it is necessary to show the cubic BiF_3 XRD patterns of literature to compare and do an accurate analysis of the XRD patterns of the synthesized compounds.



Chapter 3 Results and discussion

Figure 3.3.1 (a) XRD patterns of undoped $K_{1-x}Bi_xF_{2+x}$ nanoparticles prepared with different initial addition of K/Bi/F ratio, including 0/1/5, 0.3/0.7/2/4, 1/1/4, 1/1/6, and 1/1/7; (b) Enlarged photograph of (111) and (200) peaks.

All prepared samples in Figure 3.3.1 (a) belong to the cubic phase without traces of impurity. It seems that all the prepared samples are the same compound according to the XRD patterns. However, the enlarged photograph of the (111) and (200) peaks exhibits a slight shift (Figure 3.3.1(b)). As displayed, the XRD patterns of the prepared BiF_3 compound under $Bi/F = 1/5$ (black curve) is indeed in good accordance with that of the literature BiF_3 data (green vertical line). Afterward, with the increase of the F/K ratio from 4/1 (blue curve) to 6/1 (green curve), the position of the XRD peak moves to a small angle. When $F/K = 6/1$, the position of the prepared compounds matches well with that of literature $K_{0.3}Bi_{0.7}F_{2.4}$ compound. Further increasing the F/K ratio, the position of the peaks is unchanged and still matches well with that of literature $K_{0.3}Bi_{0.7}F_{2.4}$ compound. It is due to the ions participate in the reaction from reagents have reach the limitation.

As a result, in a large K/Bi/F ratio range, from 1/1/6 to 1/1/11, the $K_{0.3}Bi_{0.7}F_{2.4}$ has been successfully synthesized by a co-precipitation method at room temperature in the mixture medium of deionized water and ethylene glycol. Therefore, in the following works, we select 1/1/6 and 1/1/7 as the initial addition of K/Bi/F ratio to prepare the Yb/Er co-doped $K_{0.3}Bi_{0.7}F_{2.4}$ up-conversion nanoparticles.

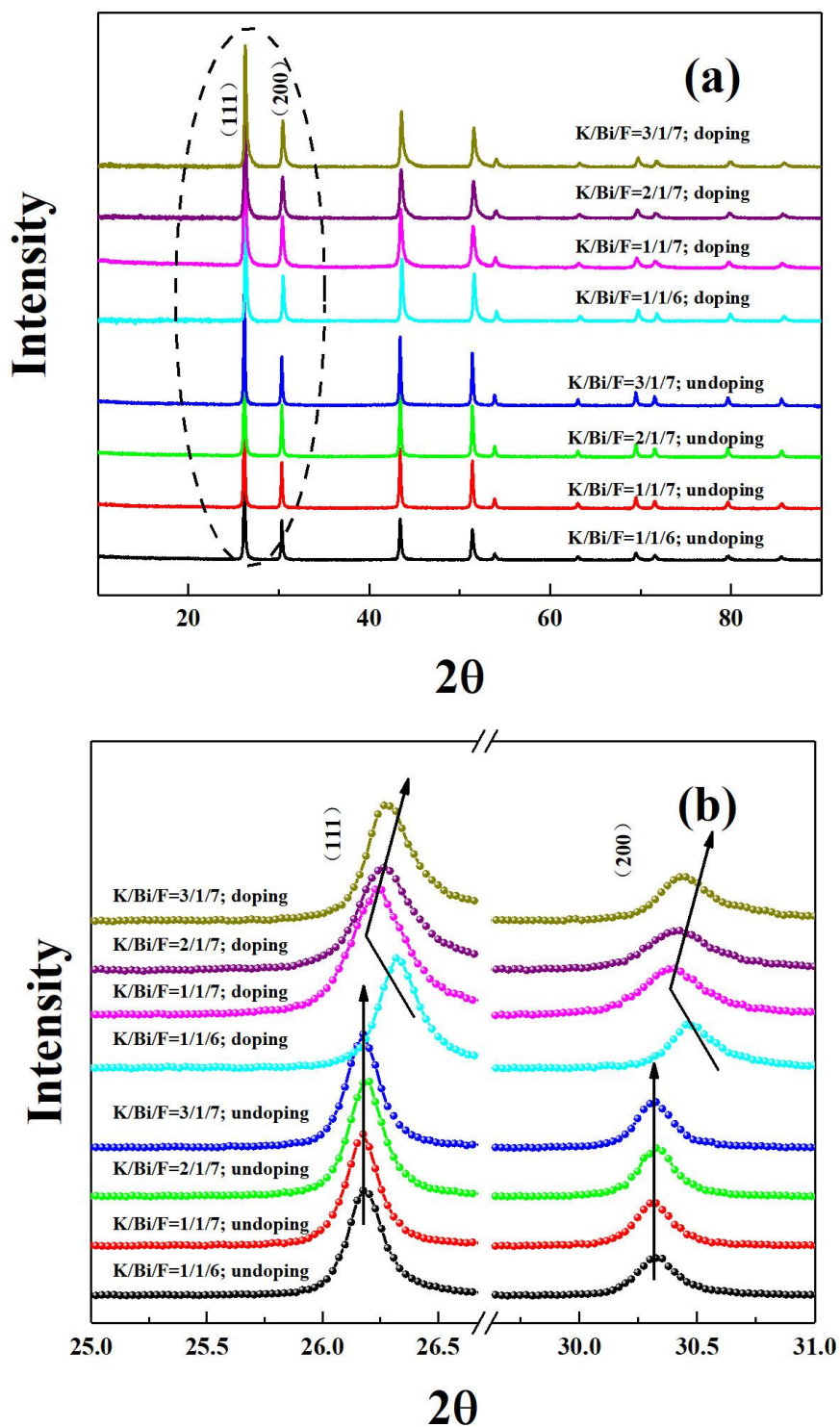


Figure 3.3.2 (a) XRD patterns of undoped and Yb/Er co-doped powder samples prepared with different initial K/Bi/F ratios, including 1/1/6, 1/1/7, 2/1/7, and 3/1/7; (b) enlarged XRD pattern photograph of the (111) and (200) peak.

Chapter 3 Results and discussion

Figure 3.2.2(a) illustrates the XRD patterns of undoped and Yb/Er co-doped $K_{0.3}Bi_{0.7}F_{2.4}$ compounds prepared with different initial addition of K/Bi/F, including 1/1/6, 1/1/7, 2/1/7, and 3/1/7. As displayed in Figure 3.2.2(a), all the prepared samples belong to cubic phase without any trace of impurity. Figure 3.2.2(b) exhibits the enlarged photograph of the peaks (111) and (200). The XRD patterns of the undoped samples are indeed unchanged and in good accordance with that of the literature $K_{0.3}Bi_{0.7}F_{2.4}$. However, the Yb/Er co-doped samples show mild movement with the increase of the initial F^- amounts.

At each same K/Bi/F ratio, the peak position of the Yb/Er co-doped sample slightly moves to high angles compared with that of the undoped sample in Figure 3.3.2(b), owing to the successful doping of Yb/Er into the $K_{0.3}Bi_{0.7}F_{2.4}$ matrix lattice. The Shannon ionic radius of Bi^{3+} (1.31 Å) is larger than that of Yb^{3+} (1.125 Å) and Er^{3+} (1.144 Å) with a VIII coordination number. When Yb^{3+} and Er^{3+} were successfully inserted into the $K_{0.3}Bi_{0.7}F_{2.2}$ lattice, the peaks of XRD patterns will move to high angle. For each prepared sample with different initial K/Bi/F ratio, including 1/1/6, 1/1/7, 2/1/7 and 3/1/7, the peak position indeed move to high angle after Yb/Er co-doping.

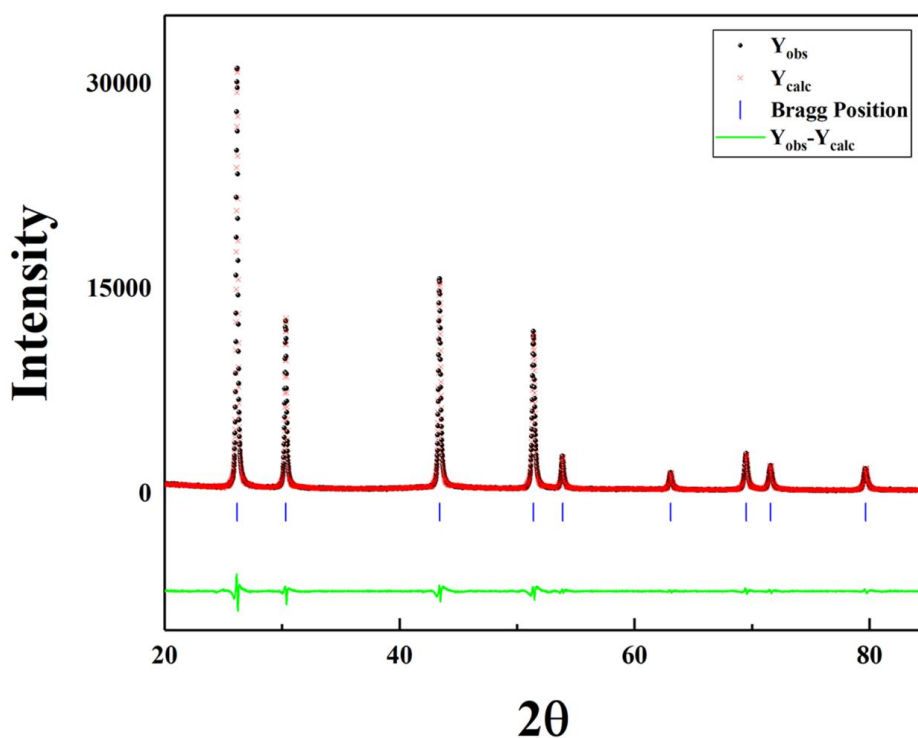


Figure 3.3.3 The profile fitting of X-ray powders diffraction pattern of the undoped sample prepared in K/Bi/F = 1/1/7 ratio under a scanning with slow speed.

Figure 3.3.3 illustrates the profile fitting of undoped K/Bi/F=1/1/7 XRD patterns under a scanning with slow speed. As displayed, the fitted curve is in good agreement with the experimental XRD data. The calculated parameter $a = 5.8902 \text{ \AA}$ is similar to $a = 5.8895 \text{ \AA}$ (PDF 01-084-0534) of the literature $\text{K}_{0.3}\text{Bi}_{0.7}\text{F}_{2.4}$.

Figure 3.3.4 gives the $B_{\text{sample}}\cos(\theta)$ with respect to $4\sin(\theta)$ of Yb/Er co-doped $\text{K}_{0.3}\text{Bi}_{0.7}\text{F}_{2.4}$ nanoparticles prepared under 1/1/7 (marked with B) and 2/1/7 (marked with C) K/Bi/F ratio, by the Williamson-Hall method based on the peaks of the XRD patterns. As displayed, the fitted lines are in good accordance with the experimental data. According to the intercept ($y_{\text{intercept}}=k\lambda/D$) and slope of the fitted lines, we calculated the mean crystallite size D and microstrain ε .

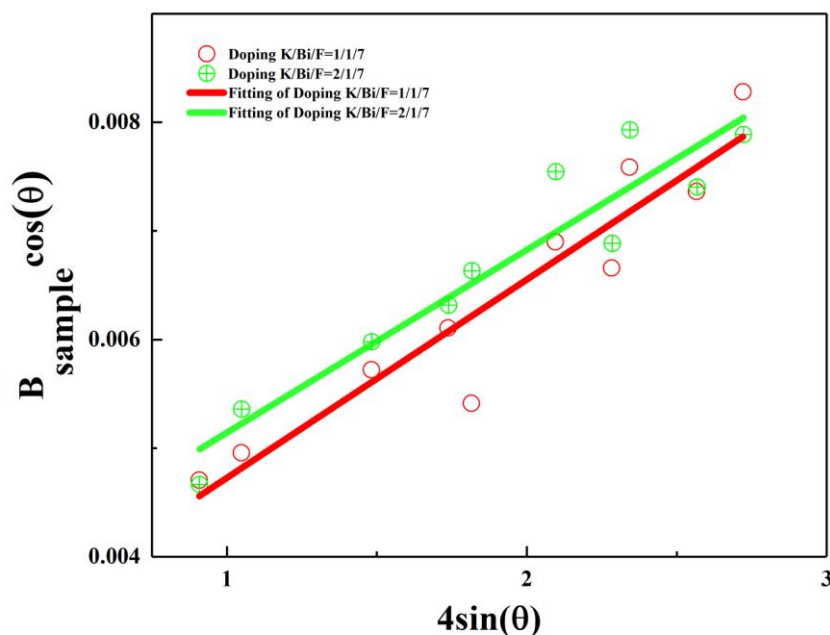


Figure 3.3.4 The $B_{sample} \cos(\theta)$ with respects to $4 \sin(\theta)$ of Yb/Er co-doped $K_{0.3}Bi_{0.7}F_{2.4}$ nanoparticles prepared under 1/1/7 (sample B, red line) and 2/1/7 (sample C, green line) K/Bi/F ratio, by the Williamson-Hall method according to the XRD patterns.

The calculated mean crystallite size and microstrain of sample B and sample C are gathered in Table 3.3.1. The sample B with K/Bi/F = 1/1/7 ratio shows 49 nm mean crystallite size. Sample C with K/Bi/F = 2/1/7 ratio shows 40 nm mean crystallite size.

Table 3.3.1 The calculated mean crystallite size and microstrain.

Samples (K/Bi/F ratio)	$Y_{intercept} (\times 10^{-3})$	Mean crystalite size D	Microstrain ε (%)
B (1/1/7)	2.9 ± 0.4	49 ± 7 nm	0.18 ± 0.03
C (2/1/7)	3.5 ± 0.4	40 ± 3 nm	0.17 ± 0.02

3.3.2 Morphology

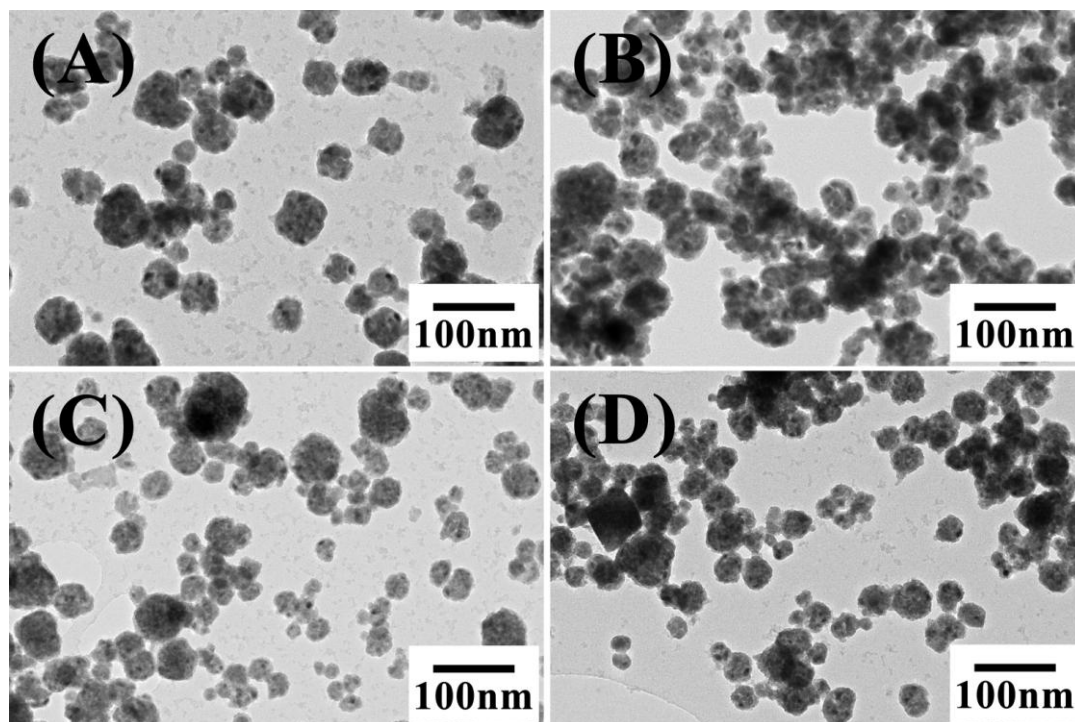


Figure 3.3.5 Transmission electron microscopy (TEM) of Yb/Er co-doped $K_{0.3}Bi_{0.7}F_{2.4}$ nanoparticles under different initial addition of K/Bi/F ratios: (A) 1/1/6; (B) 1/1/7; (C) 2/1/7; and (D) 3/1/7.

Figure 3.3.5 shows the transmission electron microscopy (TEM) of Yb/Er co-doped $K_{0.3}Bi_{0.7}F_{2.4}$ samples that prepared under different initial addition of K/Bi/F ratios, including 1/1/6, 1/1/7, 2/1/7, and 3/1/7, which are marked with (A), (B), (C), and (D), respectively. As displayed, Figure 3.3.5(A), (C), and (D) show a relatively clear grain boundary than that of (B). Meanwhile, they exhibit relatively well-dispersed morphology. Figure 3.3.5(B) includes some aggregate nanoparticles. The observed nanoparticles are all near to sphere shape. However, there are some remarkably large nanoparticles in (A) and (C), which may due to the uneven growth drawback of co-precipitation method at room temperature.

Chapter 3 Results and discussion

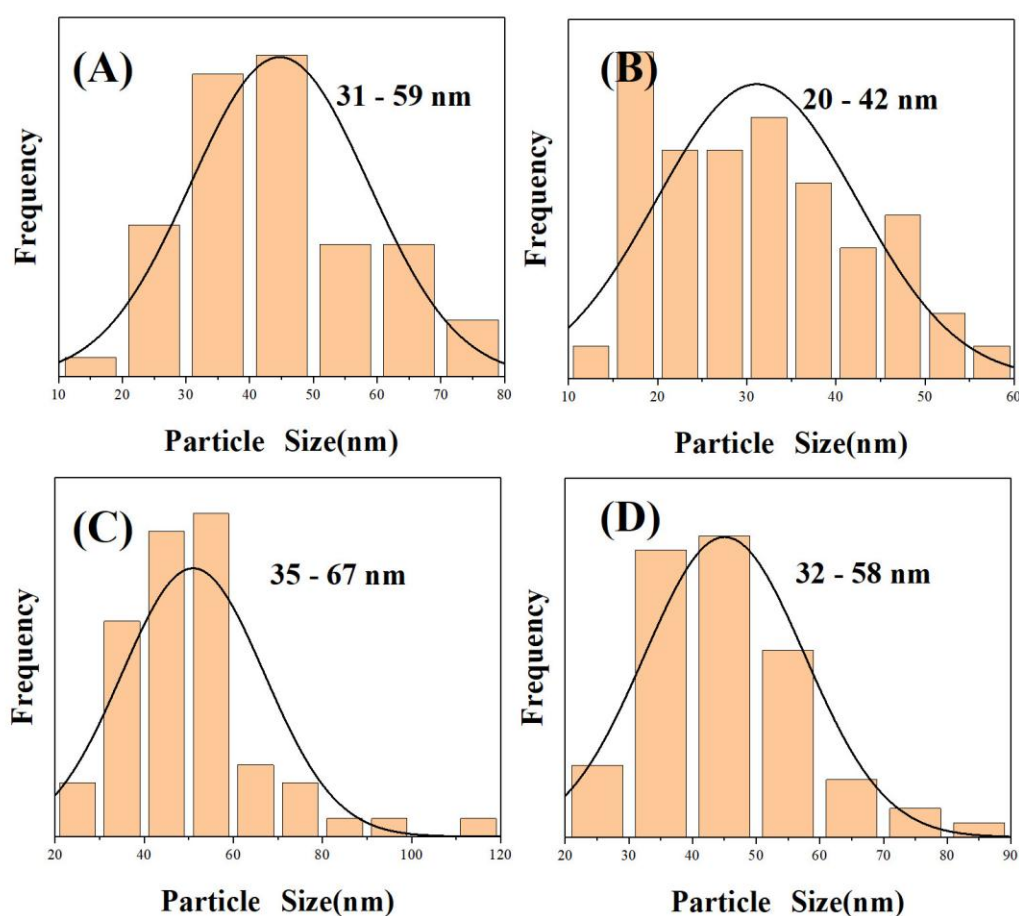


Figure 3.3.6 The histogram of the statistic size distribution of prepared samples with different initial K/Bi/F ratios according to the TEM photographs. (A) K/Bi/F = 1/1/6; (B) K/Bi/F = 1/1/7; (C) K/Bi/F = 2/1/7; and (D) K/Bi/F = 3/1/7.

For accurately comparing the nanoparticle size, the histogram of statistic size distribution was plotted in Figure 3.3.6 according to the TEM photographs. The size distribution histogram of Yb/Er co-doped $K_{0.3}Bi_{0.7}F_{2.4}$ under different initial K/Bi/F ratios, including 1/1/6, 1/1/7, 2/1/7, and 3/1/7, was marked with (A), (B), (C), and (D), respectively. The nanoparticle size distribution of the prepared samples in (A), (B), (C), and (D) is 31 - 59 nm, 20 - 42 nm, 35 - 67 nm, and 32 - 58 nm, respectively. The relatively large standard deviation implies that the size uniformity of the prepared

Chapter 3 Results and discussion

samples needs to be further improved.

Table 3.3.2 The nanoparticle size distribution from TEM photographs and the calculated mean crystallite size from XRD patterns.

Samples	Nanoparticle size from TEM	Mean crystallite size <i>D</i> from XRD
A (1/1/6)	31 - 59 nm	NG
B (1/1/7)	20 - 42 nm	49 ± 7 nm
C (2/1/7)	35 - 67 nm	40 ± 3 nm
D (3/1/7)	32 - 58 nm	NG

Table 3.3.2 collected the nanoparticles size distribution, which is from TEM photographs, and the mean crystallite size, which is calculated from XRD patterns. As displayed, for sample C, the nanoparticle size is slightly larger than the crystallite size. Meanwhile, the sample C has the largest nanoparticle size.

3.3.3 Photoluminescence properties

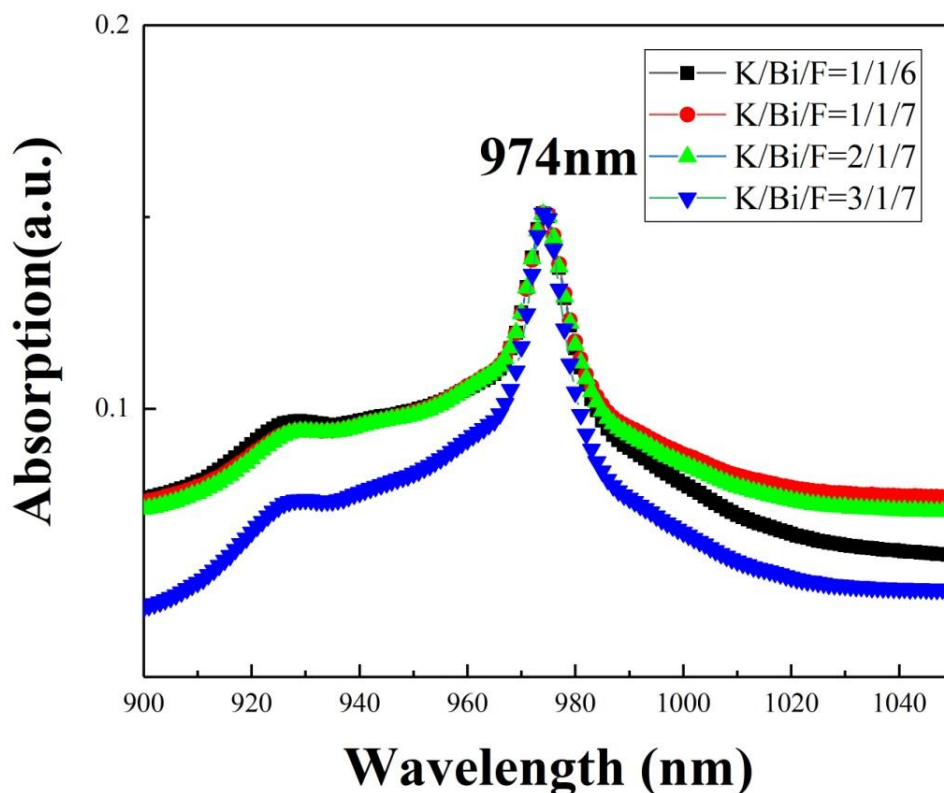


Figure 3.3.7 Absolute absorption spectrum of prepared Yb/Er co-doped $K_{0.3}Bi_{0.7}F_{2.4}$ compounds with different initial addition of K/Bi/F ratios, including 1/1/6, 1/1/7, 2/1/7, and 3/1/7.

Figure 3.3.7 illustrates the absolute absorption spectrum of synthesized Yb/Er co-doped $K_{0.3}Bi_{0.7}F_{2.4}$ compounds from 900 nm to 1050 nm. As displayed in Figure 3.3.7, the absorption spectra of the measured samples show obvious peaks of absorption at 974 nm. It is as well a proof that Yb has been successfully introduced into the $K_{0.3}Bi_{0.7}F_{2.4}$ lattice.

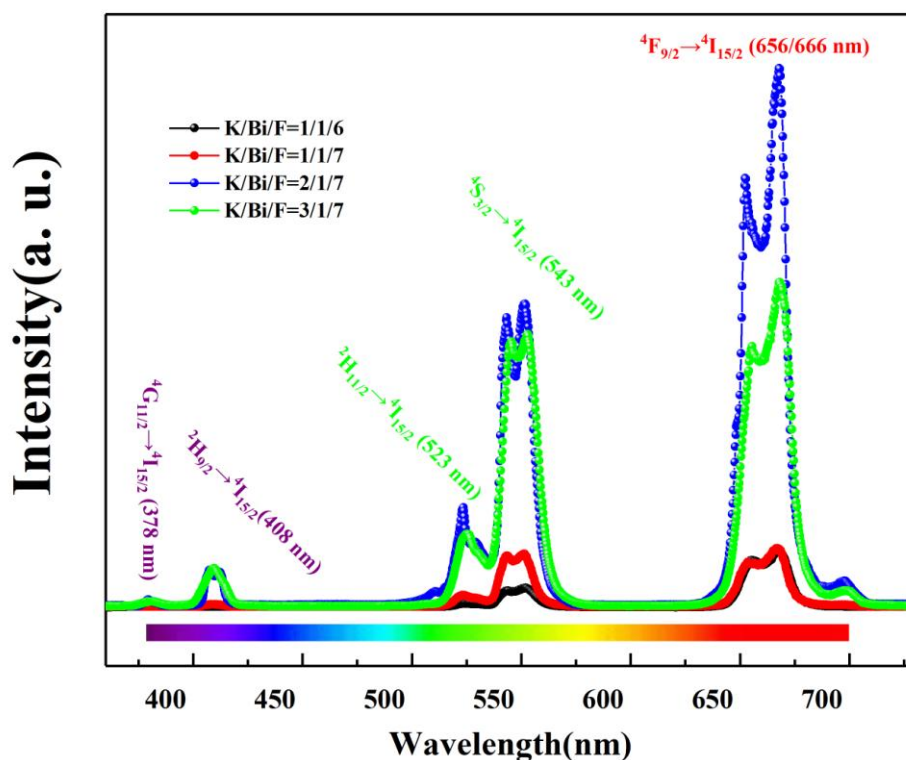


Figure 3.3.8 The emission spectrum of the Yb/Er co-doped $K_{0.3}Bi_{0.7}F_{2.4}$ compounds under different initial addition of K/Bi/F ratios, including 1/1/6, 1/1/7, 2/1/7, and 3/1/7, excited with a 974 nm pulsed laser.

Figure 3.3.8 shows the emission spectrum of the prepared Yb/Er co-doped $K_{0.3}Bi_{0.7}F_{2.4}$ nanoparticles with a 974 nm pulsed laser. As displayed, the characteristic emitting peaks of Yb/Er co-doped UCNs at 523 nm, 543 nm, and 656 nm/666 nm, that are corresponding to ${}^2H_{11/2} \rightarrow {}^4I_{15/2}$, ${}^4S_{3/2} \rightarrow {}^4I_{15/2}$, and ${}^4F_{9/2} \rightarrow {}^4I_{15/2}$ transitions of Er^{3+} , respectively, were observed. The two weak peaks at 378 nm and 408 nm, which are corresponding to ${}^4G_{11/2} \rightarrow {}^4I_{15/2}$ and ${}^2H_{9/2} \rightarrow {}^4I_{15/2}$ transition of Er^{3+} , respectively, were as well observed.

The samples, prepared with 2/1/7 and 3/1/7 ratio, show relatively high

Chapter 3 Results and discussion

luminescence intensity compared with the samples prepared under 1/1/6 and 1/1/7 ratios at 543 nm and 666 nm. The relative emitting intensity at 408 nm, 543 nm, and 666 nm is collected in Table 3.3.3.

Table 3.3.3 The intensity of relative emitting at 408 nm, 543 nm, and 666 nm of the prepared Yb/Er co-doped $K_{0.3}Bi_{0.7}F_{2.4}$ nanocrystal with different K/Bi/F ratios.

Samples	Relative Emitting Intensity at 408 nm	Relative Emitting Intensity at 543 nm	Relative Emitting Intensity at 666 nm
A (1/1/6)	0.0006	0.3	0.9
B (1/1/7)	0.04	0.8	1.0
C (2/1/7)	0.6	4.5	8.2
D (3/1/7)	0.6	3.1	4.8

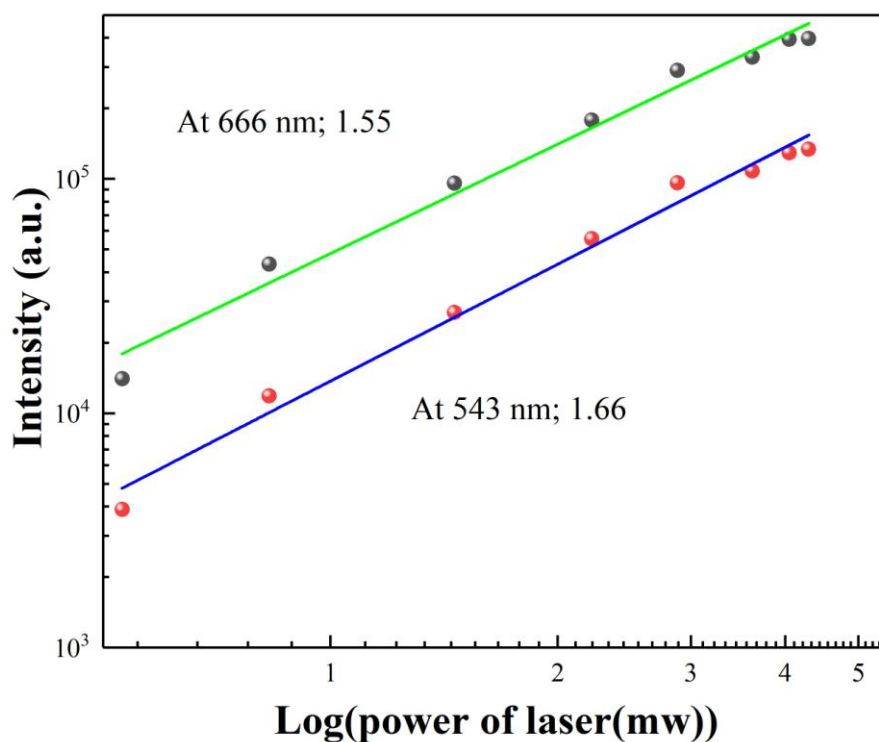
The intensity of relative emitting at 408 nm, which corresponds to ${}^2H_{9/2} \rightarrow {}^4I_{15/2}$ transition of Er^{3+} , is very weak in all the prepared samples. Sample C has the largest relative emitting intensity at 408 nm while sample A nearly has no emitting peak at 408 nm. The prepared Yb/Er co-doped $K_{0.3}Bi_{0.7}F_{2.4}$ UCNs shows the largest relative emitting intensity at 666 nm (${}^4F_{9/2} \rightarrow {}^4I_{15/2}$ transitions of Er^{3+}) compared with that at 543 nm or 408 nm. The sample C, prepared under K/Bi/F = 2/1/7 ratio, shows the highest relative emitting intensity at 408 nm, 543 nm, and 666 nm.

Chapter 3 Results and discussion

Table 3.3.4 The measured internal quantum yield of annealed sample C at 543 nm and 666 nm.

Sample	Internal quantum yield of green emission light (centred at 543 nm) (%)	Internal quantum yield of red emission light (centred at 666 nm) (%)
C-T	0.21	0.28

Table 3.3.4 exhibits the internal QY of annealed sample C at 543 nm and 666 nm. The measured internal QY is 0.21 % at 543 nm. At 666 nm, the internal QY is 0.28 %. These quantum yields are higher than that of the prepared $\text{KYF}_4\text{:Yb/Er}$ UCNs in chapter 3.1 and $\text{BiF}_3\text{:Yb/Er}$ UCNs in chapter 3.2.



Chapter 3 Results and discussion

Figure 3.3.9 The logarithmic intensity with respect to logarithmic laser power plot of sample B.

Figure 3.3.9 exhibits the fitted curves of logarithmic intensity with respect to logarithmic laser power at 543 nm and 666 nm. As displayed, the fitted line is in good agreement with the experimental data. The slope of the fitted line at 543 nm is 1.66 and at 666 nm is 1.55. They are all near to the theoretical value 2. It implies that this two up-conversion process can be described as the absorption of two photons. The difference is resulted from the competing relationships of the ions on the first-excited energy state.

Figure 3.3.10 illustrates the fitted decay curves of Yb/Er co-doped $K_{0.3}Bi_{0.7}F_{2.4}$ UCNs prepared under K/Bi/F = 1/1/7 ratio at 543 nm and 666 nm, excited by a 974 nm pulsed laser. The experimental data was fitted with double exponential function. As displayed, the fitted curves are in good agreement with the experimental data. The mean lifetimes at 543 nm (black points and green curve) and 666 nm (red points and blue curve) is 6 μ s and 14 μ s, respectively.

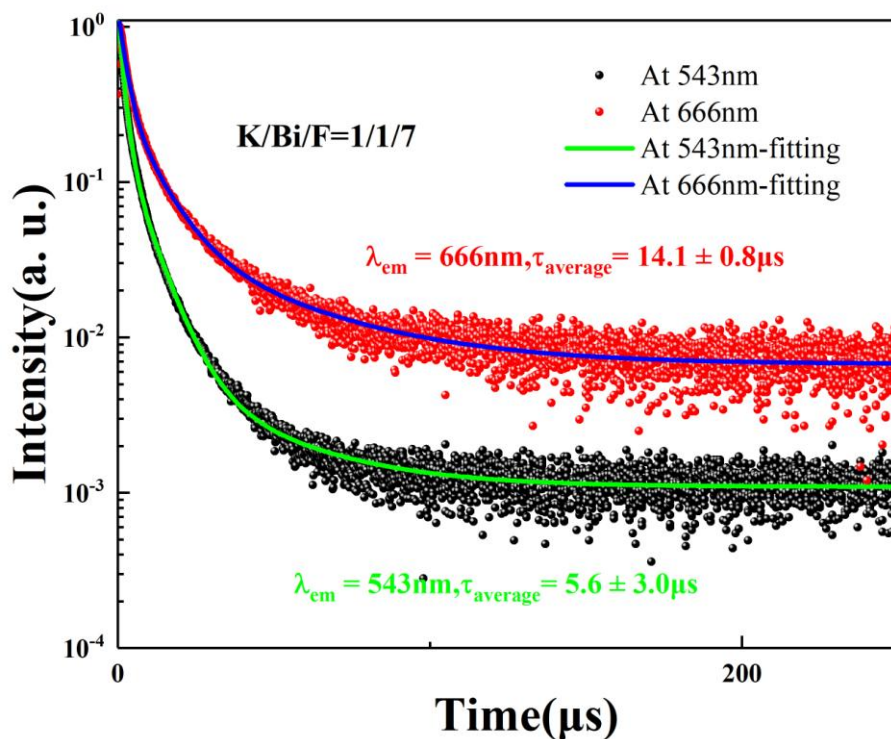
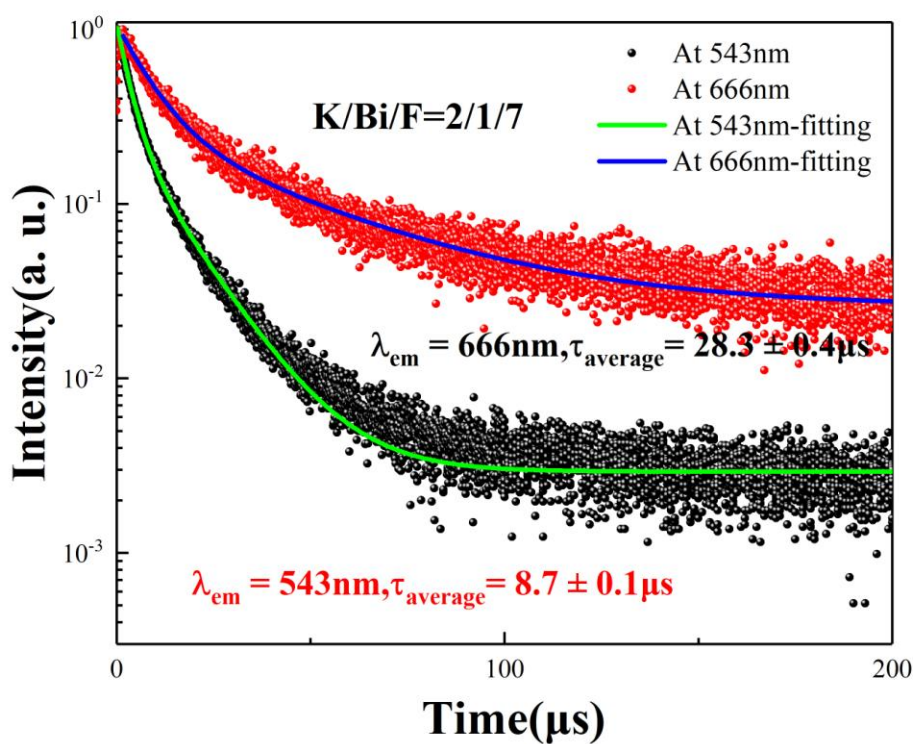


Figure 3.3.10 The fitted decay curves of Yb/Er co-doped $\text{K}_{0.3}\text{Bi}_{0.7}\text{F}_{2.4}$ UCNs prepared under $\text{K/Bi/F} = 1/1/7$ ratio (sample B) at 543 nm and 666 nm, excited by a 974 nm pulsed laser.



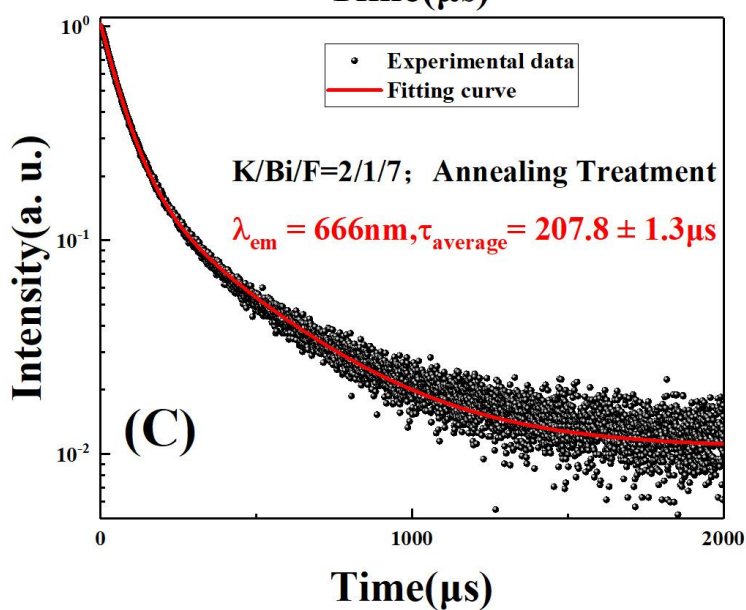
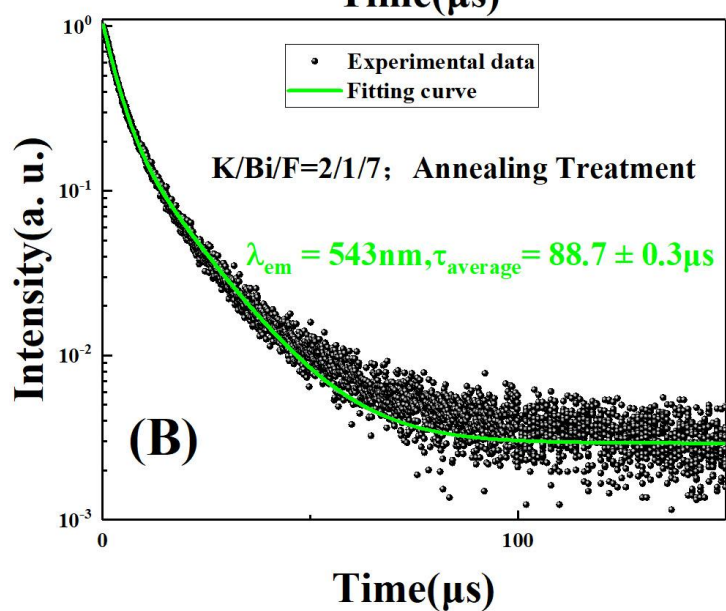
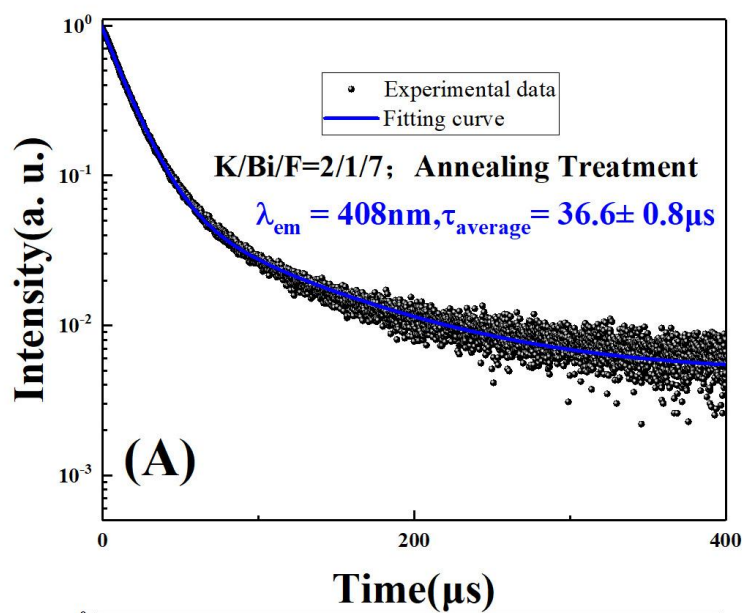
Chapter 3 Results and discussion

Figure 3.3.11 The decay curves of Yb/Er co-doped $K_{0.3}Bi_{0.7}F_{2.4}$ UCNs prepared under K/Bi/F = 2/1/7 ratio (sample C) at 543 nm and 666 nm, excited by a 974 nm pulsed laser.

Figure 3.3.11 exhibits the fitted decay curves of Yb/Er co-doped $K_{0.3}Bi_{0.7}F_{2.4}$ UCNs prepared under K/Bi/F = 2/1/7 ratio (sample C) at 543 nm and 666 nm, excited by a 974 nm pulsed laser. In comparison to the sample B (K/Bi/F = 1/1/7), the sample C (K/Bi/F = 2/1/7) possesses a longer lifetime at 543 nm (9 μ s) and 666 nm (28 μ s).

Figure 3.3.12(A), (B), and (C) illustrates the fitted decay curves of annealed sample C (K/Bi/F = 2/1/7) at 408 nm, 543 nm, and at 666nm, respectively. In comparison with sample C before annealing in Figure 3.3.11, the lifetimes of annealed sample C in Figure 3.3.12 exhibits a very large enhancement. The lifetime at 543 nm is enhanced by near ten times from 9 μ s to 89 μ s. The lifetime at 666 nm is increased from 28 μ s to 208 μ s. After annealing treatment, sample C has desirable lifetimes due to the elimination of quenching centers. The annealing treatment has an obvious effect on the lifetime enhancement of Yb/Er co-doped $K_{0.3}Bi_{0.7}F_{2.4}$ UCNs.

Chapter 3 Results and discussion



Chapter 3 Results and discussion

Figure 3.3.12 The decay curves of annealed Yb/Er co-doped $K_{0.3}Bi_{0.7}F_{2.4}$ UCNs prepared under K/Bi/F = 1/1/7 ratio at (A) 408 nm, (B) 543 nm, and (c) 666 nm, excited by a 974 nm pulsed laser.

Table 3.3.5 The lifetimes of the reported β -NaYF₄:Yb³⁺/Er³⁺ UCNs,⁶³ prepared Yb/Er co-doped $K_{0.3}Bi_{0.7}F_{2.4}$ UCNs under K/Bi/F = 1/1/7 and K/Bi/F = 2/1/7 ratio.

Samples	Decay time at 408 nm (μs)	Decay time at 543 nm (μs)	Decay time at 666nm (μs)
B (1/1/7)	NG	6 ± 3	14.1 ± 0.8
C (2/1/7)	NG	8.7 ± 0.1	28.3 ± 0.4
Annealed C (2/1/7)	36.6 ± 0.8	88.7 ± 0.3	208 ± 1
β-NaYF₄:Yb³⁺/Er³⁺	NG	81	296

Table 3.3.5 collected the decay times of sample B, sample C, and annealed sample C at 408 nm, 543 nm, and 666 nm. The annealing treatment has a remarkable effect on increasing the lifetimes. Especially, the lifetime of annealed sample C at 408 nm was obtained, which is unmeasurable before annealing treatment. The reported β -NaYF₄:Yb³⁺/Er³⁺ UCNs²³ was also presented, which has been recognized as the most efficient UCNs so far. The 89 μs of annealed sample C at 543 nm, which corresponds to $^4S_{3/2} \rightarrow ^4I_{15/2}$ transitions of Er³⁺, is similar to the reported 81 μs of hexagonal NaYF₄:Yb³⁺/Er³⁺ UCNs. At 666 nm, which corresponds to the $^4F_{9/2} \rightarrow ^4I_{15/2}$ transitions of Er³⁺, the 208 μs of sample C is shorter than the reported 296 μs of hexagonal NaYF₄:Yb³⁺/Er³⁺ UCNs.⁶³ Though the lifetimes of present works are shorter than that of the most efficiency ones, for a fast co-precipitation method at

Chapter 3 Results and discussion

room temperature, the lifetimes of prepared Yb/Er co-doped $K_{0.3}Bi_{0.7}F_{2.4}$ UCNs are desirable.

The desirable long lifetimes, high emitting intensity and desirable internal QY indicate this novel $K_{0.3}Bi_{0.7}F_{2.4}$ compounds are a very suitable “green” matrix candidate of UCNs.

3.3.4 Conclusion

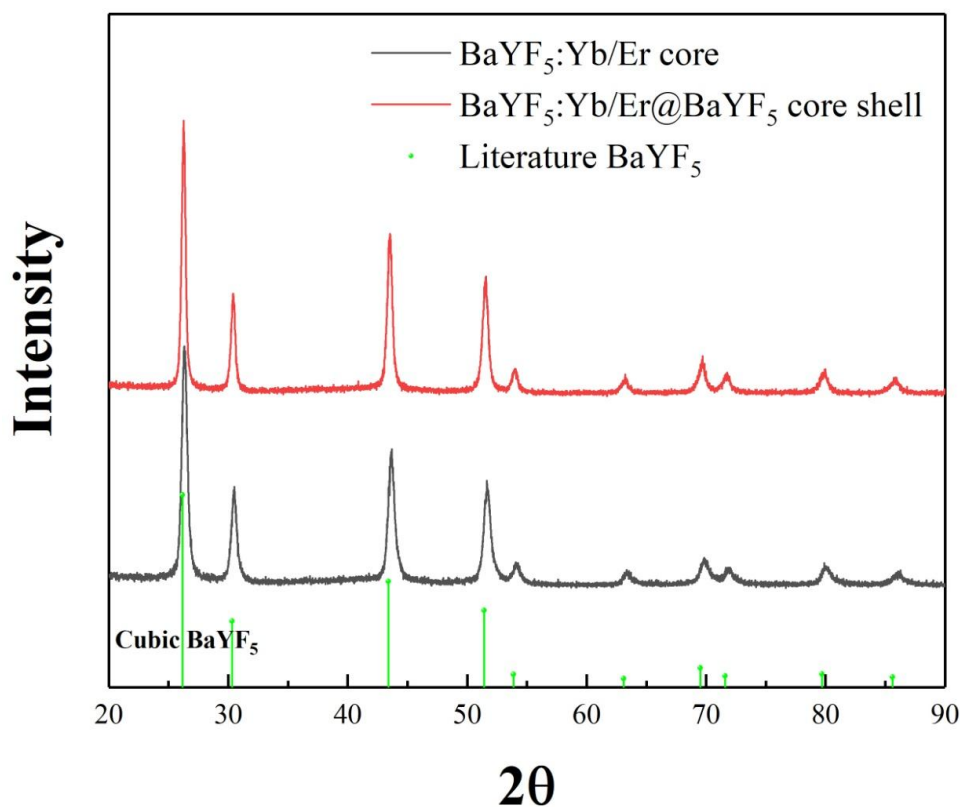
In this chapter, the $K_{0.3}Bi_{0.7}F_{2.4}$ nanoparticles and Yb/Er co-doped $K_{0.3}Bi_{0.7}F_{2.4}$ up-conversion nanoparticles have been successfully synthesized at room temperature via a co-precipitation method with different initial addition of K/Bi/F ratios. The prepared samples are in good agreement with the cubic $K_{0.3}Bi_{0.7}F_{2.4}$ of literature. The calculated mean crystallite size from XRD patterns and statistic mean nanoparticles size from HRTEM were compared and analyzed.

The prepared samples show strong characteristic emitting peaks of Yb/Er co-doped UCNs. The internal quantum yield of sample C is 0.21 % at 543 nm and 0.28 % at 666 nm. Especially, the annealed sample C shows excellent lifetimes at 408 nm, 543 nm, and 666 nm. This novel matrix, with high emitting intensity, desirable luminescence lifetimes and internal QY, provides a candidate of host materials for up-conversion nanoparticles. It has potential application in many fields.

3.4 BaYF₅:20%Yb/2%Er coated with BaYF₅

The researches about finding novel host materials for UC process are necessary. We have presented novel BiF₃- and K_{0.3}Bi_{0.7}F_{2.4}-based UCNs in chapter 3.2 and chapter 3.3, respectively. They have a good performance in photoluminescence properties. The similar cubic BaREF₅ compounds have been reported in some works and have proved to be a suitable host material in photoluminescence field.¹⁷⁷⁻¹⁸⁰ In this chapter, the BaYF₅:20%Yb/2%Er (written as BaYF₅:Yb/Er) up-conversion nanoparticles and BaYF₅:20%Yb/2%Er coated with BaYF₅ (written as BaYF₅:Yb/Er@BaYF₅) will be synthesized by a two-step hydrothermal method. The XRD patterns, morphology and photoluminescence properties of the two compounds will be analyzed and discussed.

3.4.1 Structure



Chapter 3 Results and discussion

Figure 3.4.1 XRD patterns of the prepared BaYF₅:Yb/Er nanoparticles (black curve) and BaYF₅:Yb/Er@BaYF₅ compounds (red curve), compared with cubic BaYF₅ of literature (green vertical lines).

Figure 3.4.1 illustrates the XRD patterns of the prepared BaYF₅:Yb/Er nanoparticles and BaYF₅:Yb/Er@BaYF₅ compounds. The vertical green line represents the cubic BaYF₅ compounds of literature PDF 04-018-2140. As displayed, the XRD patterns of the prepared BaYF₅:Yb/Er and BaYF₅:Yb/Er@BaYF₅ compounds are all in good accordance with that of the cubic BaYF₅ of literature. It demonstrates that the BaYF₅ matrix was successfully synthesized via solvothermal method.

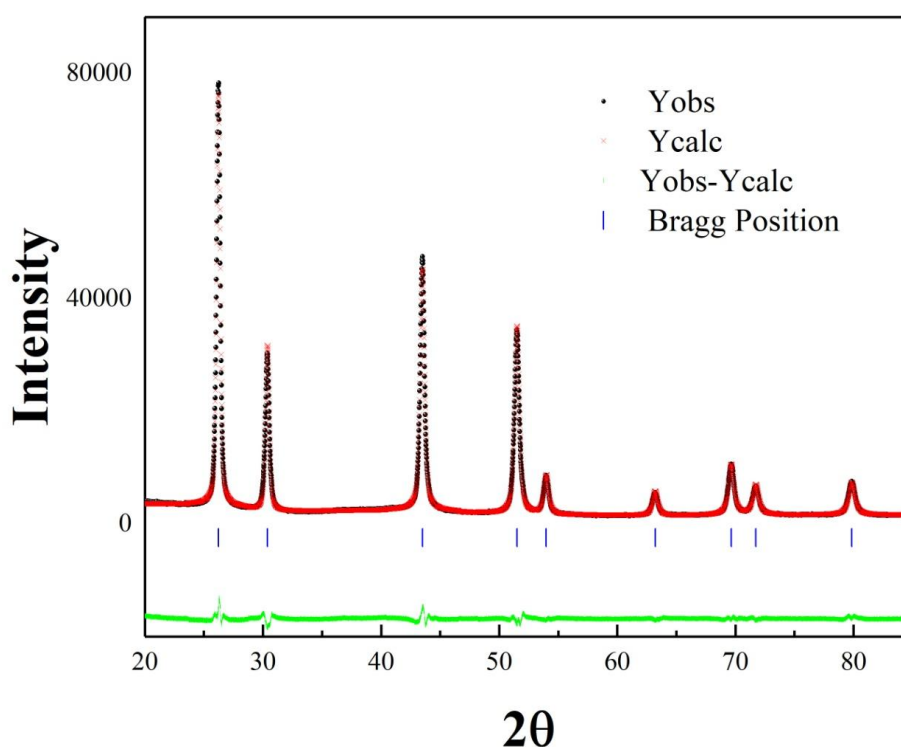


Figure 3.4.2 The profile fitting of the XRD patterns of BaYF₅:Yb/Er nanoparticles.

Figure 3.4.2 illustrates the profile fitting curve of BaYF₅:Yb/Er nanoparticles. The

Chapter 3 Results and discussion

calculated lattice parameter of the BaYF₅:Yb/Er nanoparticles is 5.8795 Å. It is smaller than the 5.8900 Å, which is the lattice parameter of literature BaYF₅ (PDF 04-018-2140). It is a proof that the Yb/Er has been successfully introduced into the BaYF₅ lattice. Because the Shannon ionic radius of Y³⁺, Yb³⁺, and Er³⁺ with VIII coordination number is 1.159 Å, 1.125 Å, and 1.144 Å, respectively.^{115,168} The Y³⁺ has a bigger Shannon ionic radius than that of Yb³⁺ and Er³⁺. On condition that the Yb/Er ions are introduced into the lattice of the BaYF₅ matrix to substitute some Y³⁺ ions, the lattice parameter of the matrix will change smaller.

The crystallite sizes of the two compounds were calculated by Williamson-Hall method. Figure 3.4.3 gives the $B_{sample}\cos(\theta)$ with respect to $4\sin(\theta)$ of BaYF₅:Yb/Er nanoparticles and BaYF₅:Yb/Er@BaYF₅ compounds. As displayed, the fitted lines are in good accordance with the experimental data. Afterward, we calculated the mean crystallite size D and microstrain ε according to the slope $y_{intercept}=k\lambda/D$ and intercept of the fitted lines.

The calculated mean crystallite size D and microstrain ε were collected in Table 3.4.1. The mean crystallite size of the BaYF₅:Yb/Er and BaYF₅:Yb/Er@BaYF₅ compounds is 20 nm and 33 nm, respectively. After deposition of the BaYF₅ onto the BaYF₅:Yb/Er compounds, the mean crystallite size get enhancement.

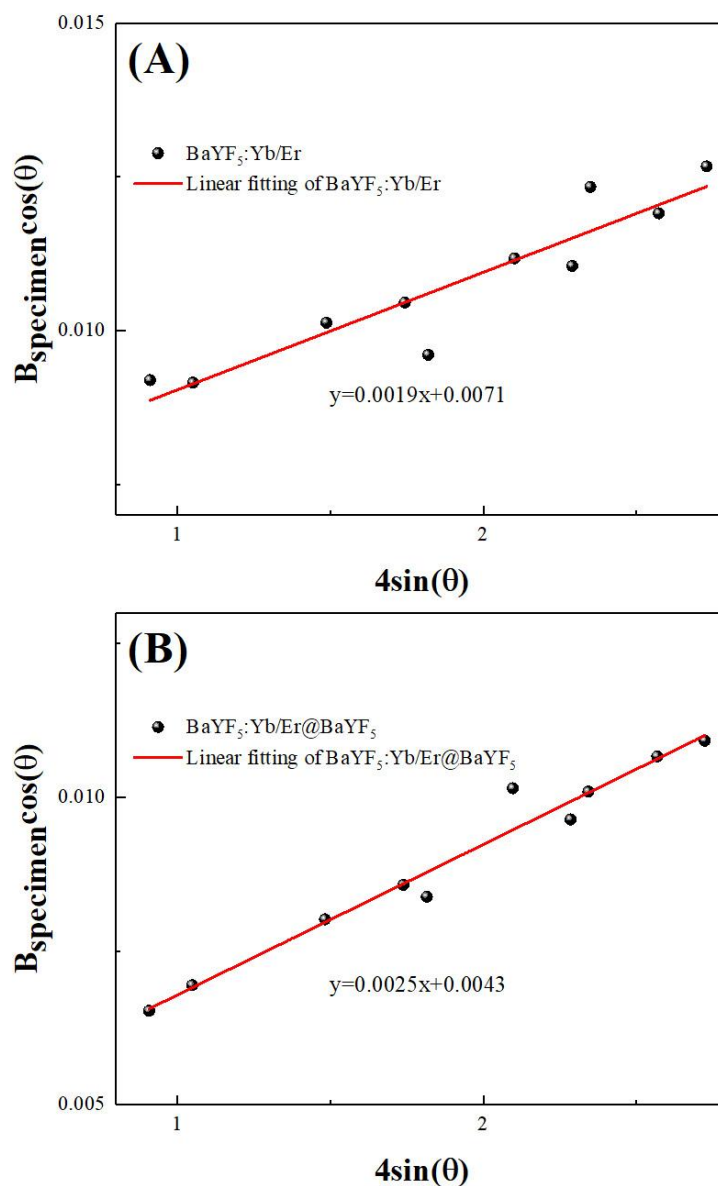


Figure 3.4.3 The fitted line of the $B_{sample} \cos(\theta)$ concerning $4\sin(\theta)$ of (A) BaYF₅:Yb/Er nanoparticles and (B) BaYF₅:Yb/Er@BaYF₅ compounds.

Chapter 3 Results and discussion

Table 3.4.1 The calculated $Y_{\text{intercept}}$, mean crystallite size D , and microstrain ε according to the XRD patterns of the prepared samples.

Samples	$Y_{\text{intercept}} (\times 10^{-3})$	Mean crystallite size D	Microstrain ε (%)
BaYF₅:20%Yb/ 2%Er	7.1 ± 0.5	20 ± 2 nm	0.19 ± 0.03
BaYF₅:20%Yb/ 2%Er@ BaYF₅	4.3 ± 0.3	33 ± 3 nm	0.25 ± 0.02

3.4.2 Morphology

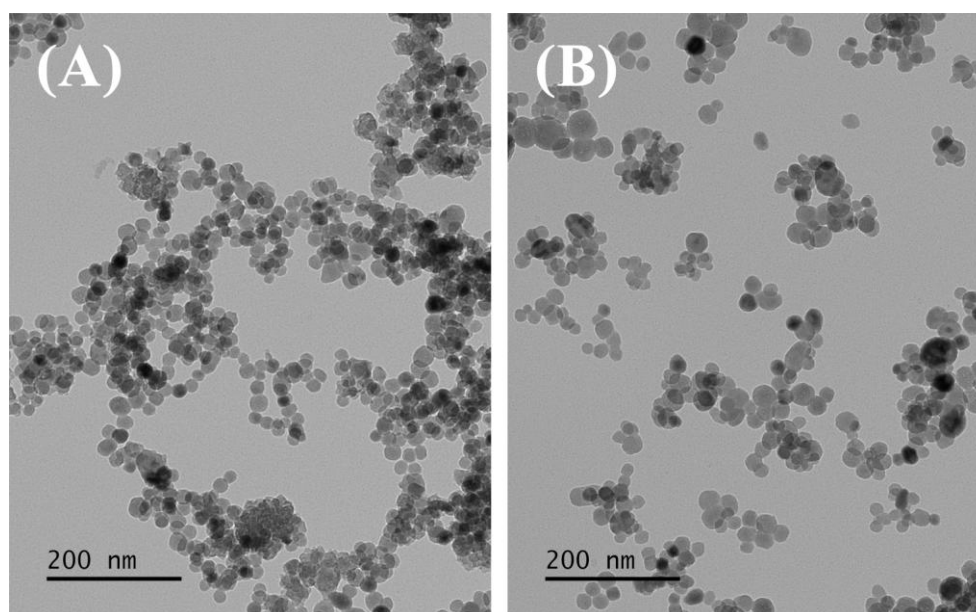


Figure 3.4.4 The transmission electronic microscope (TEM) of (A): the prepared BaYF₅:Yb/Er; and (B): BaYF₅:Yb/Er@BaYF₅ nanoparticles.

Figure 3.4.4 shows the TEM images of the prepared BaYF₅:Yb/Er and BaYF₅:Yb/Er@BaYF₅ nanoparticles. As displayed in Figure 3.4.4(A), most of the

Chapter 3 Results and discussion

nanoparticles are well-dispersed and uniformity. Very few nanoparticles show an aggregation. The nanoparticles in Figure 3.4.4(B) are all uniformity and well-dispersed without aggregation. In addition, all the nanoparticles in Figure 3.4.4 are close to sphere.

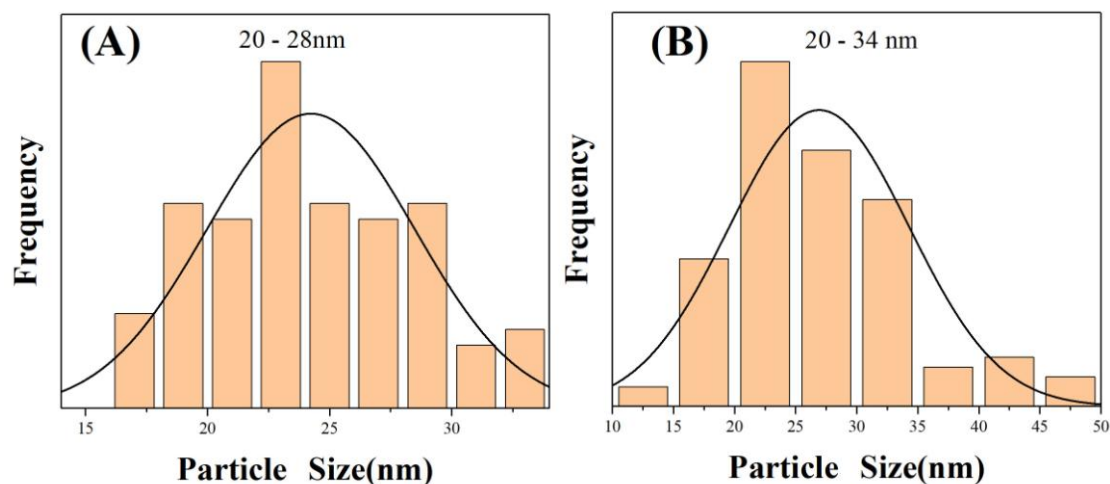


Figure 3.4.5 The size distribution of (A): BaYF₅:Yb/Er; and (B): BaYF₅:Yb/Er@BaYF₅ nanoparticles.

Figure 3.4.5 illustrates the size distribution of the prepared samples based on the TEM images in Figure 3.4.1. The BaYF₅:Yb/Er@BaYF₅ have a slightly larger nanoparticles (20 - 34 nm) than that of the BaYF₅:Yb/Er (20 - 28 nm). The coated BaYF₅ results in the growth of the nanoparticles.

Chapter 3 Results and discussion

Table 3.4.2 The nanoparticles size distribution from TEM and mean crystallite size from XRD patterns of the prepared BaYF₅:Yb/Er; and BaYF₅:Yb/Er@BaYF₅ nanoparticles.

Samples	Nanoparticle size distribution from TEM	Mean crystallite size <i>D</i> from XRD
BaYF₅:20%Yb/2%Er	20 - 28 nm	20 ± 2 nm
BaYF₅:20%Yb/2%Er@ BaYF₅	20 - 34 nm	33 ± 3 nm

The nanoparticle size distribution and mean crystallite size were collected in Table 3.4.2. In comparison of the prepared samples, the nanoparticles size is in good agreement with the mean crystallite size. The size of BaYF₅:Yb/Er@BaYF₅ gets a slight increase due to the coated BaYF₅.

3.4.3 Photoluminescence properties

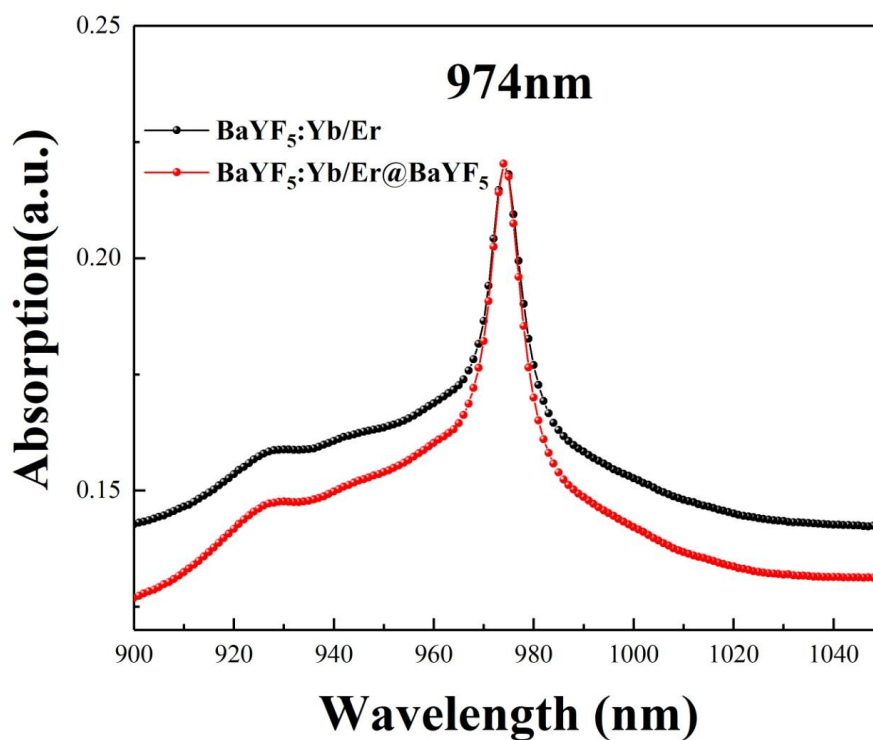


Figure 3.4.6 The absolute absorption spectra of the BaYF₅:Yb/Er and BaYF₅:Yb/Er@BaYF₅ nanoparticles from 900 nm to 1050 nm.

Figure 3.4.6 exhibits the absolute absorption spectra of the prepared BaYF₅:Yb/Er and BaYF₅:Yb/Er@BaYF₅ UCNs from 900 nm to 1050 nm. As displayed, the two samples have an obvious absorption peak at 974 nm.

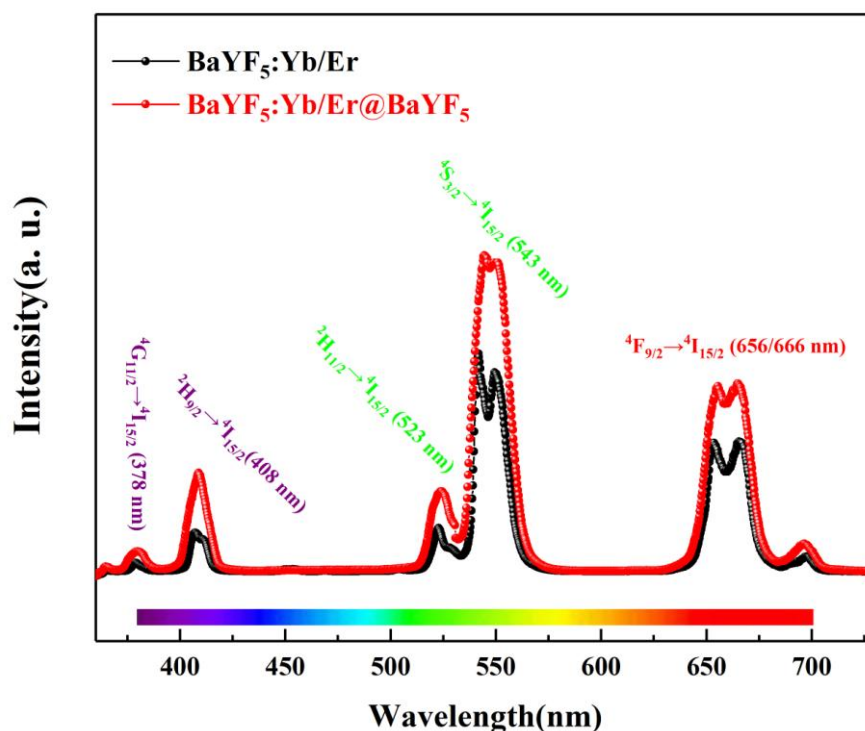


Figure 3.4.7 The emission spectra of the prepared BaYF₅:Yb/Er and BaYF₅:Yb/Er@BaYF₅ UCNs under a pulsed exciting laser of 974 nm.

Figure 3.4.7 illustrates the emission spectra of the prepared BaYF₅:Yb/Er and BaYF₅:Yb/Er@BaYF₅ UCNs excited by a 974 nm pulsed laser. As displayed, the characteristic emitting peaks of Yb/Er co-doped UCNs at green and red were observed. The emitting peaks at 378 nm, 408 nm, 523 nm, 543 nm and 656/666 nm corresponds to the $^4G_{11/2} \rightarrow ^4I_{15/2}$, $^2H_{9/2} \rightarrow ^4I_{15/2}$, $^2H_{11/2} \rightarrow ^4I_{15/2}$, $^4S_{3/2} \rightarrow ^4I_{15/2}$, and $^4F_{9/2} \rightarrow ^4I_{15/2}$ transitions of Er³⁺, respectively. The whole emitting intensity of the BaYF₅:Yb/Er@BaYF₅ UCNs is stronger than that of the BaYF₅:Yb/Er UCNs.

Chapter 3 Results and discussion

Table 3.4.3 The relative emitting intensity at 408 nm, at 543 nm, and at 666 nm of the prepared BaYF₅:Yb/Er and BaYF₅:Yb/Er@ BaYF₅ nanoparticles.

Samples	Relative Emitting Intensity at 408 nm (a. u.)	Relative Emitting Intensity at 543 nm (a. u.)	Relative Emitting Intensity at 666 nm (a. u.)
BaYF₅:Yb/Er	0.5	2.7	1.8
BaYF₅:Yb/Er@ BaYF₅	1.3	4.2	2.6

Table 3.4.3 gathered the relative emitting intensity at 408 nm, 543 nm, and 666 nm. In comparison to the BaYF₅:Yb/Er UCNs, the BaYF₅:Yb/Er coated with BaYF₅ compounds possess stronger relative emitting intensity at each emitting peak. The main problem, which reduces the efficiency of the UC process, is the quenching centres onto the nanoparticles. Because high-frequency modes of ligands onto the nanocrystal surface (e.g. OH⁻ and CH⁻ groups) could activate many non-radiative channels to decrease the UC efficiency.¹⁶⁷ However, the coated BaYF₅ can shield the core from the surrounding ligands and solvents of high phonon energy that quenches the UC process in some degree to enhance the efficiency of UC.¹⁸¹

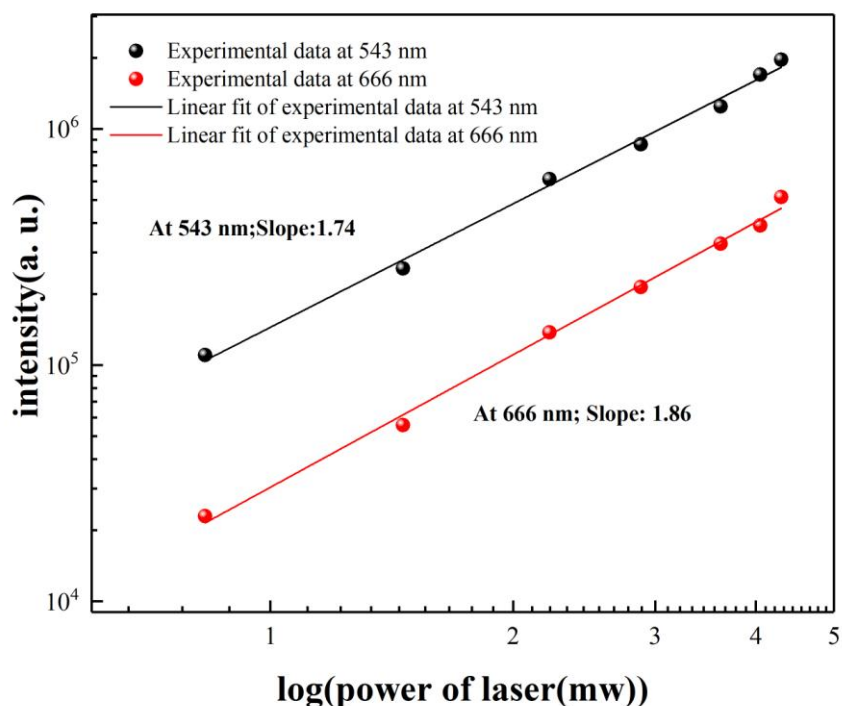


Figure 3.4.8 The log emitting intensity with respect to log energy power of a 974 nm excitation laser of the prepared BaYF₅:Yb/Er UCNs.

Figure 3.4.8 exhibits the log emitting intensity concerning the log energy power of the excitation laser of the prepared BaYF₅:Yb/Er nanoparticles. As displayed, the fitted lines are in good agreement with the experimental data. The fitted slope at 543 nm and 666 nm is 1.74 and 1.86, respectively. They are all close to the theoretical value 2. It indicates that the UC process in this compound indeed successively absorbs two photons.

Figure 3.4.9 exhibits the fitted decay curves of BaYF₅:Yb/Er UCNs at 543 nm and 666 nm. As displayed, the fitted decay curves, which are plotted by a double exponential function, are in good agreement with the experimental data. The

Chapter 3 Results and discussion

calculated mean lifetimes are 23 μs at 543 nm and 44 μs at 666 nm.

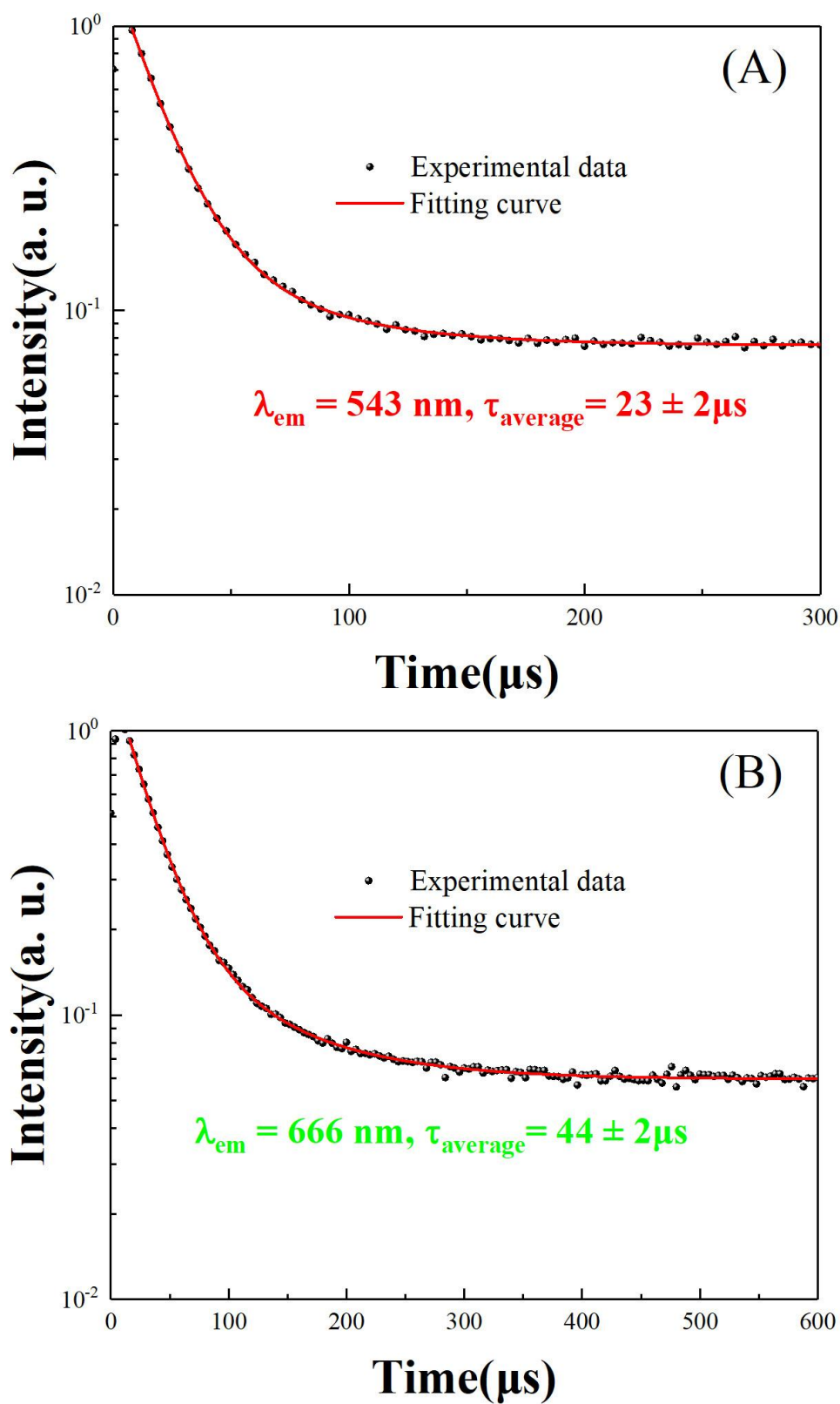
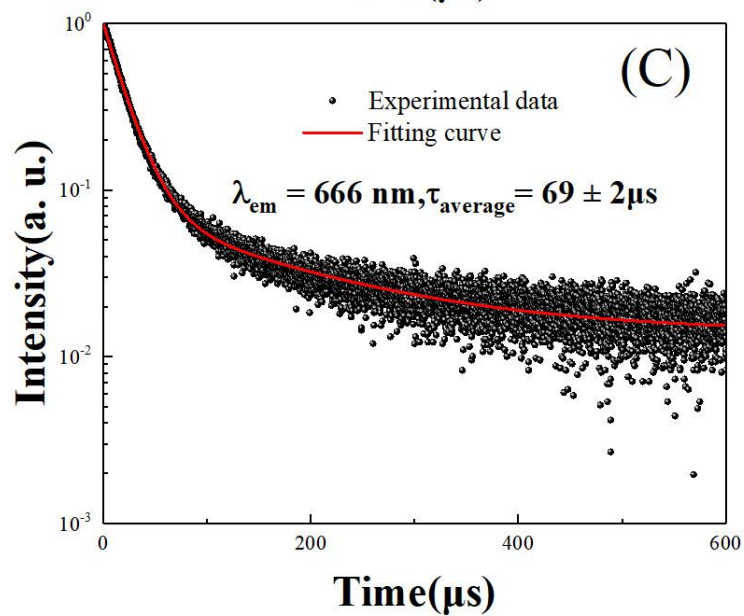
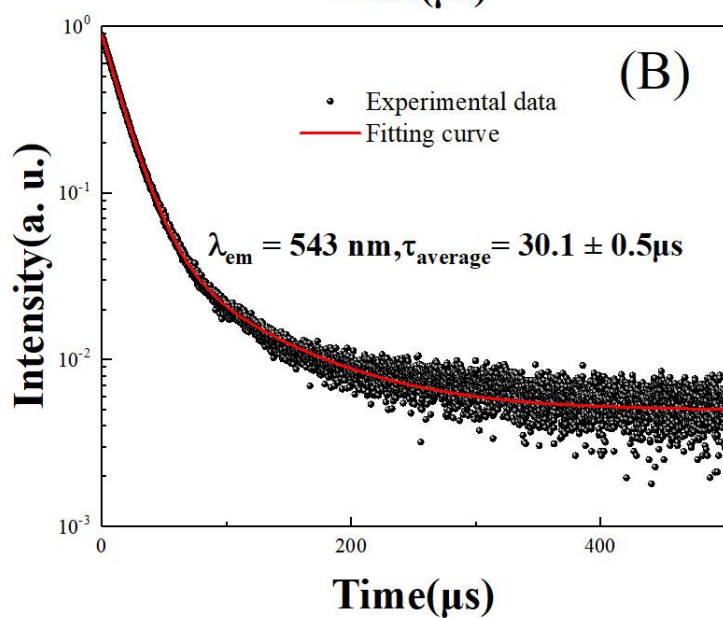
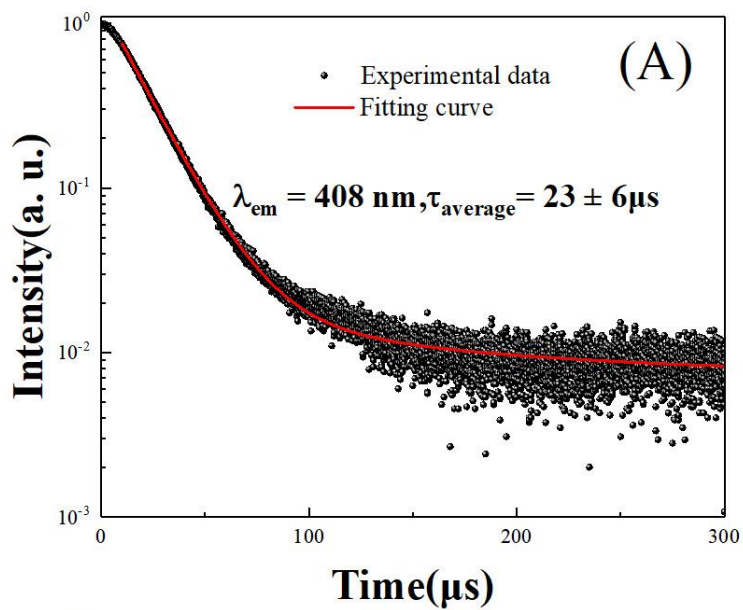


Figure 3.4.9 The fitted decay curves of BaYF₅ UCNs at (A) 543 nm and (B) 666 nm.

Chapter 3 Results and discussion



Chapter 3 Results and discussion

Figure 3.4.10 The fitted decay curves of BaYF₅:Yb/Er@BaYF₅ UCNs at (A) 408 nm, (B) 543 nm, and (C) 666 nm.

Figure 3.4.10 illustrates the fitted decay curves of BaYF₅:Yb/Er@BaYF₅ UCNs. The experimental data are fitted well with the double exponential function curves. After epitaxial growth of the BaYF₅ onto the BaYF₅:Yb/Er compounds, the lifetimes have an obvious enhancement. The lifetime at 543 nm increase from 23 μ s to 30 μ s. The lifetime at 666 nm increase from 44 μ s to 70 μ s.

3.4.4 Conclusion

In Chapter 3.4.4, the BaYF₅:Yb/Er UCNs and BaYF₅:Yb/Er@BaYF₅ UCNs have been successfully prepared via a solvothermal approach. The prepared samples match well with the cubic BaYF₅. The crystallite size and lattice parameter were calculated based on the XRD patterns. The spectrum of the BaYF₅:Yb/Er UCNs and BaYF₅:Yb/Er@BaYF₅ UCNs have been measured. They all show the characteristic emission peaks of Yb/Er co-doped UCNs. The emitting intensity of BaYF₅:Yb/Er@BaYF₅ is stronger than that of the BaYF₅:Yb/Er. The lifetimes get an enhancement after coating the BaYF₅. The lifetime increased from 23 μ s to 30 μ s at 543 nm. At 666 nm, the lifetime increased from 44 μ s to 70 μ s.

Chapter 4 General conclusion and perspective of UCNs

4.1 General conclusion

In this work, four different fluoride-based host materials of UCNs were prepared, including $\text{KYF}_4:10\% \text{Yb}/5\% \text{Er}$, $\text{BiF}_3:10\% \text{Yb}/5\% \text{Er}$, $\text{KBi}_{0.3}\text{F}_{0.7}:10\% \text{Yb}/5\% \text{Er}$, and $\text{BaYF}_5:20\% \text{Yb}/2\% \text{Er}$ @ BaYF_5 compounds.

In Chapter 3.1, the 10% Yb/5%Er co-doped KYF_4 UCNs have been prepared in the water-ethanol mixture solvent. The crystallite size and the lattice parameter were calculated. The mean crystallite sizes are in good accordance with the mean nanoparticles size from TEM images. The B series samples, especially the B_1 , show good morphology and possess the highest photoluminescence intensity at both green or red light. The annealed B_1 sample has excellent lifetimes, 80 μs at 543 nm and 312 μs at 666 nm. The measured internal QY of annealed sample B is 0.20 % at 543 nm and 0.14 % at 666 nm.

In Chapter 3.2, the undoped BiF_3 and 10% Yb/5%Er co-doped cubic BiF_3 up-conversion nanoparticles were successfully prepared in the mixture medium of ethylene glycol and deionized water. The crystallite size and the lattice parameter were calculated according to the XRD patterns. The mean nanoparticle size of the compounds is around 40 – 50 nm. The obtained compounds show characteristic emission peaks of Yb/Er co-doped UCNs. Sample D has the highest efficiency at 666 nm and sample E has the relative highest efficiency at 408 nm and 543 nm. The average photoluminescence lifetimes suggest that the annealed sample E has a

Chapter 3 Results and discussion

relatively desirable average lifetime at 408 nm (14 μ s), at 543 nm (21 μ s), and 666 nm (87 μ s). The measured internal QY of annealed sample B is 0.13 % at 543 nm and 0.09 % at 666 nm.

In Chapter 3.3, the $K_{0.3}Bi_{0.7}F_{2.4}$ nanoparticles and 10%Yb/5%Er co-doped $K_{0.3}Bi_{0.7}F_{2.4}$ up-conversion nanoparticles have been successfully synthesized at RT via a co-precipitation method with different initial addition of K/Bi/F ratios. The prepared samples are in good agreement with the cubic $K_{0.3}Bi_{0.7}F_{2.4}$ of the literature. The calculated mean crystallite size from XRD patterns and statistic mean nanoparticle size from TEM were compared and analyzed. The prepared samples show strong characteristic emitting peaks of Yb/Er co-doped UCNs. Especially, the annealed sample C shows excellent lifetimes at 408 nm (37 μ s), 543 nm (89 μ s), and 666 nm (208 μ s). The measured internal QY of annealed sample C is 0.21 % at 543 nm and 0.28 % at 666 nm.

In Chapter 3.4, the $BaYF_5:20\%Yb/2\%Er$ UCNs and $BaYF_5:Yb/Er@BaYF_5$ UCNs have been successfully prepared via a two-step solvothermal approach. The XRD patterns of the prepared samples match well with that of the cubic $BaYF_5$. The crystallite size and lattice parameter were calculated based on the XRD patterns. The spectrum of the $BaYF_5:Yb/Er$ UCNs and $BaYF_5:Yb/Er@BaYF_5$ UCNs have been measured. They all show the characteristic emission peaks of Yb/Er co-doped UCNs. The emission intensity of $BaYF_5:Yb/Er@BaYF_5$ is stronger than that of the $BaYF_5:Yb/Er$. After coated with $BaYF_5$, the lifetime of $BaYF_5:Yb/Er@BaYF_5$, at 543 nm, increase from 23 μ s to 30 μ s. At 666 nm, the lifetime increases from 44 μ s to 70 μ s.

4.2 Perspective of UCNs

The quantum yield is the main problem that hinders the application of UCNs. For a given UCNs, the internal QY has a strong relationship with the nanoparticle size. For example, the QY of microcrystalline UC materials is 100 times stronger than that of the counterpart UCNs. In addition, the measurements of absolute internal quantum yield still have no standard. Especially for the powders, the recognized measurements by the integrating sphere have limitations for such low QY. The integrating sphere measurements have an accuracy of $\pm 2\%$.¹⁶¹ However, the internal QY of the well known most efficiency UCNs is less than 0.3 % at the green light with a ~ 980 nm excitation laser. It also needs to consider the second absorption from the scatter of the sphere wall for powders. Otherwise, even the intensity of emitting light cannot be compared in different articles. The only parameter that can be compared is the lifetime, which is reported rarely. Currently, the most application on UCNs is the bioimaging, for which the observation of emission visible light by bare eyes is enough. It has not a strict requirement on the lifetimes or internal QY. It is a primary application of UCNs. The deep applications need to be studied.

The most efficient UCNs are hexagonal β -NaYF₄:20% Yb³⁺, 2% Er³⁺, which has a better performance than cubic NaYF₄. The phase-dependent optical property can be ascribed directly to the different crystal fields around the trivalent lanthanide ions in matrices of various symmetries. Low symmetry hosts typically exert a crystal field containing more uneven components around the doped ions compared to the high symmetry counterparts. The uneven components enhance the electronic coupling between the 4f energy levels and higher electronic configuration and subsequently

Chapter 3 Results and discussion

increase f–f transition probabilities of the doping ions. Therefore, future works may focus on preparing the asymmetric phase structure of the novel host materials.

The core-shell structure is also a good way to enhance the luminescence properties. It can shield the core away from the quenching centers, which onto the surface of the nanoparticles. The internal QY of reported 30 nm β -NaYF₄:20%Yb³⁺/2% Er³⁺ is 0.1 % at 540 nm with 980 nm excitation laser. The internal QY of β -NaYF₄:20%Yb³⁺/2%Er³⁺/ β -NaYF₄ core-shell structure UCNs is 0.3 % at 540 nm with 980 nm excitation laser.¹⁸²

Bibliography

1. S. Wen, J. Zhou, K. Zheng, A. Bednarkiewicz, X. Liu, and D. Jin. Advances in highly doped upconversion nanoparticles. *Nat. Commun.*, **9**, 2415 (2018).
2. A. Noculak and A. Podhorodecki. Size and shape effects in β -NaGdF₄:Yb³⁺, Er³⁺ nanocrystals. *Nanotechnology*, **28**, 17 (2017).
3. A. R. Miandashti, M. E. Kordesch, and H. H. Richardson. Effect of temperature and gold nanoparticle interaction on the lifetime and luminescence of NaYF₄:Yb³⁺:Er³⁺ upconverting nanoparticles. *ACS Photonics*, **4**, 1864–1869 (2017).
4. S. Yamini, P. Priya, S. Priya, M. Gunaseelan, and J. Senthilselvan. Structural phase transformations in KYF₄:Er³⁺ nanoparticles synthesized by hydrothermal method for upconversion applications. *AIP Conf. Proc.*, **1832**, 3–6 (2017).
5. R. An, P. Lei, P. Zhang, X. Xu, J. Feng, and H. Zhang. Near-infrared optical and X-ray computed tomography dual-modal imaging probe based on novel lanthanide-doped K_{0.3}Bi_{0.7}F_{2.4} upconversion nanoparticles. *Nanoscale*, **10**, 1394–1402 (2018).
6. W. Feng, C. Han, and F. Li. Upconversion-nanophosphor-based functional nanocomposites. *Adv. Mater.*, **25**, 5287–5303 (2013).
7. A. Bagheri, H. Arandiyani, C. Boyer, and M. Lim. Lanthanide-doped upconversion nanoparticles: emerging intelligent light-activated drug delivery systems. *Adv. Sci.*, **3**, 1500437 (2016).
8. F. E. Auzel. Materials and devices using double-pumped phosphors with energy transfer. *Proc. IEEE*, **61**, 758–786 (1973).

Bibliography

9. X. Huang, S. Han, W. Huang, and X. Liu. Enhancing solar cell efficiency: the search for luminescent materials as spectral converters. *Chem. Soc. Rev.*, **42**, 173–201 (2013).
10. Z. Gu, L. Yan, G. Tian, S. Li, Z. Chai, and Y. Zhao. Recent advances in design and fabrication of upconversion nanoparticles and their safe theranostic applications. *Adv. Mater.*, **25**, 3758–3779 (2013).
11. M. Haase and H. Schäfer. Upconverting nanoparticles. *Angew. Chem. Int. Ed.*, **50**, 5808–5829 (2011).
12. F. Auzel. Upconversion and anti-Stokes processes with f and d ions in solids. *Chem. Rev.*, **104**, 139–173 (2004).
13. F. Auzel. Upconversion processes in coupled ion systems. *J. Lumin.*, **45**, 341–345 (1990).
14. Y. Wang, S. Gai, N. Niu, F. He, and P. Yang. Synthesis of NaYF₄ microcrystals with different morphologies and enhanced up-conversion luminescence properties. *Phys. Chem. Chem. Phys.*, **15**, 16795–16805 (2013).
15. D. J. Gargas, E. M. Chan, A. D. Ostrowski, S. Aloni, M. V. P. Altoe, E. S. Barnard, B. Sani, J. J. Urban, D. J. Million, B. E. Cohen, and P. J. Schuck. Engineering bright sub-10-nm upconverting nanocrystals for single-molecule imaging. *Nat. Nanotechnol.*, **9**, 300–305 (2014).
16. P. P. Nampi, H. Varma, P. R. Biju, T. Kakar, G. Jose, S. Saha, and P. Millner. Sodium yttrium fluoride based upconversion nano phosphors for biosensing. *J. Phys. Conf. Ser.*, **619**, 012043 (2015).
17. J. Zhao, J. A. Piper, J. M. Dawes, D. Jin, and E. M. Goldys. Mechanisms of size-dependent lifetime quenching in luminescent upconverting colloidal

Bibliography

- NaYF₄:Yb, Er nanocrystals. *2011 Int. Quantum Electron. Conf.*, 384–386 (2011).
18. W. Deng, L. Sudheendra, J. Zhao, J. Fu, D. Jin, I. M. Kenedy, and E. M. Goldys. Upconversion in NaYF₄:Yb, Er nanoparticles amplified by metal nanostructures. *Nanotechnology*, **22**, 325604 (2011).
19. Y. Zhu, S. Zhao, B. Zhou, H. Zhu, and Y. Wang. Enhancing upconversion luminescence of LiYF₄:Yb,Er nanocrystals by Cd²⁺ doping and core-shell structure. *J. Phys. Chem. C*, **121**, 18909–18916 (2017).
20. P. Lei, R. An, S. Yao, Q. Wang, L. Dong, X. Xu, K. Du, J. Feng, and H. Zhang. Ultrafast synthesis of novel hexagonal phase NaBiF₄ upconversion nanoparticles at room temperature. *Adv. Mater.*, **29**, 1700505 (2017).
21. F. Wang and X. Liu. Upconversion multicolor fine-tuning: Visible to near-infrared emission from lanthanide-doped NaYF₄ nanoparticles. *J. Am. Chem. Soc.*, **130**, 5642-5643 (2008).
22. A. C. Yanes, A. Santana-Alonso, J. Mendez-Ramos, and J. del-Castillo. Structure and intense UV up-conversion emissions in RE³⁺-doped sol-gel glass-ceramics containing KYF₄ nanocrystals. *Appl. Phys. B Lasers Opt.*, **113**, 589–596 (2013).
23. X. Su, X. Sun, S. Wu, and S. Zhang. Manipulating the emission intensity and lifetime of NaYF₄:Yb³⁺,Er³⁺ simultaneously by embedding it into CdS photonic crystals. *Nanoscale*, **9**, 7666–7673 (2017).
24. S. Mishra, S. Daniele, G. Ledoux, E. Jeanneau, and M. F. Joubert. Heterometallic Na-Y(Ln) trifluoroacetate diglyme complexes as novel single-source precursors for upconverting NaYF₄ nanocrystals co-doped with

Bibliography

- Yb and Er/Tm ions. *Chem. Commun.*, **46**, 3756–3758 (2010).
25. J. C. Goldschmidt and S. Fischer. Upconversion for photovoltaics—a review of materials, devices and concepts for performance enhancement. *Adv. Opt. Mater.*, **3**, 510–535 (2015).
26. G. Liu and B. Jacquier. Spectroscopic properties of rare earths in optical materials. *Materials Science*, **83**, 266-268 (2005).
27. C. K. Hong and L. Mandel. Theory of parametric frequency down conversion of light. *Physical Review A*, **31**, 2409-2418 (1985)
28. N. Bloemberga. Solid state infrared quantum counters. *Phys. Rev. Lett.*, **2**, 84–85 (1959).
29. F. Vetrone. Luminescence spectroscopy of Er³⁺ doped inorganic nanocrystal-An investigation into their upconversion properties. PhD thesis, Canda (2005).
30. Y. Mita, H. Yamamoto, K. Katayanagi, and S. Shionoya. Energy transfer processes in Er³⁺ and Yb³⁺ doped infrared upconversion materials. *J. Appl. Phys.*, **78**, 1219–1223 (1995).
31. G. F. J. Garlick. Infrared to visible light conversion. *Contemp. Phys.*, **17**, 127–144 (1976).
32. J. C. Wright. Radiationless processes in molecules and condensed phases. Springer, Germany (1976).
33. G. L. Wiggins. Up-converted emissions of Er³⁺ doped Gd₂(WO₄)₃ phosphors. master thesis, Georgia (2016).
34. L. Pihlgren. NIR-VIS up-conversion luminescence in the Yb³⁺, Er³⁺ doped Y₂O₂S, ZrO₂, and NaYF₄ nanomaterials. PhD thesis, Finland (2014).

Bibliography

35. F. Wang and X. Liu. Recent advances in the chemistry of lanthanide-doped upconversion nanocrystals. *Chem. Soc. Rev.*, **38**, 976–989 (2009).
36. J. S. Chivian, W. E. Case, and D. D. Eden. The photon avalanche: a new phenomenon in Pr^{3+} based infrared quantum counters. *Appl. Phys. Lett.*, **35**, 124–125 (1979).
37. M. Malinowski. Dynamics of the IR-to-blue wavelength upconversion in Pr^{3+} -doped yttrium aluminum garnet and LiYF_4 crystals. *Phys. Rev. B*, **50**, 367–374 (1994).
38. S. Heer, M. Wermuth, K. Kramer, and H. U. Gudel. Sharp ${}^2\text{E}$ upconversion luminescence of Cr^{3+} in $\text{Y}_3\text{Ga}_5\text{O}_{12}$ codoped with Cr^{3+} and Yb^{3+} . *Phys. Rev. B*, **65**, 125112 (2002).
39. D. Yin, C. Wang, J. Ouyang, K. Song, B. Liu, X. Cao, L. Zhang, Y. Han, X. Long, and M. Wu. Enhancing upconversion luminescence of $\text{NaYF}_4:\text{Yb}/\text{Er}$ nanocrystals by Mo^{3+} doping and their application in bioimaging. *Dalt. Trans.* **43**, 12037–12043 (2014).
40. O. S. Wenger, G. M. Salley, R. Valiente, and H. U. Gudel. Luminescence upconversion under hydrostatic pressure in the 3d-metal systems $\text{Ti}^{2+}:\text{NaCl}$ and $\text{Ni}^{2+}:\text{CsCdCl}_3$. *Phys. Rev. B*, **65**, 212108 (2002).
41. S. Hubert, C. L. Song, and M. Genet. Up conversion process in U^{4+} -doped ThBr_4 and ThCl_4 . *J. Solid. State. Chem.*, **61**, 252–259 (1986).
42. V. M. Lojpur, P. S. Ahrenkiel, and M. D. Dramicain. Color-tunable up-conversion emission in $\text{Y}_2\text{O}_3:\text{Yb}^{3+}, \text{Er}^{3+}$ nanoparticles prepared by polymer complex solution method. *Nanoscale Res. Lett.*, **8**, 2–7 (2013).
43. Y. Onodera, T. Nunokawa, O. Odawara, and H. Wada. Upconversion

Bibliography

- properties of $\text{Y}_2\text{O}_3:\text{Er}$, Yb nanoparticles prepared by laser ablation in water. *J. Lumin.*, **137**, 220–224 (2013).
44. Y. Q. Shenga, J. Liu, L. L. Xu, D. Zhai, Z. G. Zhang, W. W. Cao. Effect of Eu^{3+} codoping on upconversion luminescence in $\text{Y}_2\text{O}_3:\text{Er}^{3+}$, Yb^{3+} nanocrystals. *Solid State Commun.*, **150**, 1048–1051 (2010).
45. A. P. Jadhav, J. H. Oh, S. W. Park, H. Choi, B. K. Moon, B. C. Choi, K. Jang, J. H. Jeong, S. S. Yi, and J. H. Kim. Enhanced down and upconversion emission for Li^+ co-doped $\text{Gd}_2\text{O}_3:\text{Er}^{3+}$ nanostructures. *Curr. Appl. Phys.*, **16**, 1374–1381 (2016).
46. H. Guo, N. Dong, M. Yin, W. Zhang, L. Lou, and S. Xia. Visible upconversion in rare earth ion-doped Gd_2O_3 nanocrystals. *J. Phys. Chem. B*, **108**, 19205–19209 (2004).
47. Y. Wu, S. Lin, J. Liu, Y. Ji, J. Xu, L. Xu, and K. Chen. Efficient up-conversion red emission from $\text{TiO}_2:\text{Yb}$, Er nanocrystals. *Opt. Express.*, **25**, 1736–1741 (2017).
48. Z. Yang, K. Zhu, Z. Song, D. Zhou, Z. Yin, and J. Qiu. Preparation and upconversion emission properties of $\text{TiO}_2:\text{Yb}$, Er inverse opals. *Solid State Commun.*, **151**, 364–367 (2011).
49. F. C. Li, H. Wada, and Y. Kitamoto. NIR-responsive upconversion nanoparticles/anatase TiO_2 composite aerogel. *Jpn. J. Appl. Phys.*, **57**, 02CC03 (2018)
50. V. Singh, V. K. Rai, I. Ledoux-Rak, L. Badie, and H. Y. Kwak. Visible upconversion and infrared luminescence investigations of Al_2O_3 powders doped with Er^{3+} , Yb^{3+} and Zn^{2+} ions. *Appl. Phys. B*, **97**, 805-811 (2009).

Bibliography

51. D. Ramachari, D. Esparza, T. Lopez-Luke, V. H. Romero, L. Perez-Mayen, E. De la Rosa, and C. K. Jayasankar. Synthesis of co-doped $\text{Yb}^{3+}\text{-Er}^{3+}\text{:ZrO}_2$ upconversion nanoparticles and their applications in enhanced photovoltaic properties of quantum dot sensitized solar cells. *J. Alloys Compd.*, **698**, 433-441 (2017).
52. B. A. Rao, Y. R. Rao, K. K. Goud, and M. Srinivas. Upconversion luminescence in $\text{Er}^{3+}/\text{Yb}^{3+}$ codoped $\text{PbO-Bi}_2\text{O}_3\text{-Al}_2\text{O}_3\text{-B}_2\text{O}_3$ glasses. *IOP Conf. Ser. Mater. Sci. Eng.* **73**, 2–6 (2015).
53. L. Li, F. Qin, Y. Zhou, Y. Zheng, H. Zhao and Z. Zhang. Using the upconversion luminescence of the $\text{CaWO}_4\text{:Yb}^{3+}\text{-X}^{3+}$ ($\text{X} = \text{Er/Ho/Tm}$) phosphors for ratiometric thermal sensing. *J. Lumin.*, **202**, 301-308 (2018).
54. M. Liu, S. W. Wang, J. Zhang, L. Q. An, and L. D. Chen. Upconversion luminescence of $\text{Y}_3\text{Al}_5\text{O}_{12}\text{(YAG):Yb}^{3+}, \text{Tm}^{3+}$ nanocrystals. *Opt. Mater.*, **30**, 370–374 (2007).
55. M. Yang, Y. Sui, S. Wang, X. Wang, Y. Sheng, Z. Zhang, T. Lü, and W. Liu. Enhancement of upconversion emission in $\text{Y}_3\text{Al}_5\text{O}_{12}\text{:Er}^{3+}$ induced by Li^+ doping at interstitial sites. *Chem. Phys. Lett.*, **492**, 40–43 (2010).
56. G. Özen, O. Forte, and B. D. Bartolo. Downconversion and upconversion dynamics in Pr-doped $\text{Y}_3\text{Al}_5\text{O}_{12}$ crystals. *J. Appl. Phys.*, **013510**, 20–25 (2006).
57. K. Spariosu, M. Birnbaum, and B. Viana, $\text{Er}^{3+}\text{:Y}_3\text{Al}_5\text{O}_{12}$ laser dynamics: effects of upconversion. *J. Opt. Soc. Am. B*, **11**, 894–900 (1994).
58. S. Heer, M. Wermuth, K. Kramer, and H. U. Gudel. Upconversion excitation of $\text{Cr}^{3+} \text{ } ^2\text{E}$ emission in $\text{Y}_3\text{Ga}_5\text{O}_{12}$ codoped with Cr^{3+} and Yb^{3+} . *Chem. Phys. Lett.*, **334**, 293–297 (2001).

Bibliography

59. J. C. Boyer, F. Vetrone, L. A. Cuccia, and J. A. Capobianco. Synthesis of colloidal upconverting NaYF₄ nanocrystals doped with Er³⁺, Yb³⁺ and Tm³⁺, Yb³⁺ via thermal decomposition of lanthanide trifluoroacetate precursors. *J. Am. Chem. Soc.*, **128**, 7444–7445 (2006).
60. C. Homann, L. Krukewitt, F. Frenzel, B. Grauel, C. Würth, U. Resch-Genger, and M. Haase. NaYF₄:Yb,Er/NaYF₄ core/shell nanocrystals with high upconversion luminescence quantum yield. *Angew. Chemie. Int. Ed.*, **57**, 8765–8769 (2018).
61. L. Liang, Y. Liu, C. Bu, K. Guo, W. Sun, N. Huang, T. Peng, B. Sebo, M. Pan, W. Liu, S. Guo, and X. Z. Zhao. Highly uniform, bifunctional core/double-shell-structured β-NaYF₄:Er³⁺,Yb³⁺@SiO₂@TiO₂ hexagonal sub-micropisms for high-performance dye sensitized solar cells. *Adv. Mater.*, **25**, 2174–2180 (2013).
62. W. Zhang, F. Ding, and S. Y. Chou. Large enhancement of upconversion luminescence of NaYF₄:Yb³⁺/Er³⁺ nanocrystal by 3D plasmonic nano-antennas. *Adv. Mater.*, **24**, 236–241 (2012).
63. R. Arppe, I. Hyppänen, N. Perälä, R. Peltomaa, M. Kaiser, C. Würth, S. Christ, U. Resch-Genger, M. Schäferling, and T. Soukka. Quenching of the upconversion luminescence of NaYF₄:Yb³⁺,Er³⁺ and NaYF₄:Yb³⁺,Tm³⁺ nanophosphors by water: the role of the sensitizer Yb³⁺ in non-radiative relaxation. *Nanoscale*, **7**, 11746–11757 (2015).
64. G. S. Yi and G. M. Chow. Water-soluble NaYF₄:Yb,Er(Tm)/NaYF₄/Polymer core shell/shell nanoparticles with significant enhancement of upconversion fluorescence. *Chem. Mater.*, **19**, 341–343 (2007).

Bibliography

65. J. H. Zeng, J. Su, Z. H. Li, R. X. Yan, and Y. D. Li. Synthesis and upconversion luminescence of hexagonal-phase NaYF₄:Yb, Er³⁺ phosphors of controlled size and morphology. *Adv. Mater.*, **17**, 2119–2123 (2005).
66. W. You, D. Tu, W. Zheng, X. Shang, X. Song, S. Zhou, Y. Liu, R. Li, and X. Chen. Large-scale synthesis of uniform lanthanide-doped NaREF₄ upconversion/downshifting nanoprobe for bioapplication. *Nanoscale*, **10**, 11477–11484 (2018)
67. D. Yang, Y. Dai, P. Ma, X. Kang, Z. Cheng, C. Li and J. Lin. One-step synthesis of small-sized and water-soluble NaREF₄ upconversion nanoparticles for In vitro cell imaging and drug delivery. *Chem. Eur. J.*, **19**, 2685–2694 (2013).
68. X. Liu, Y. Ni, C. Zhu, L. Fang, J. Kou, C. Lu, and Z. Xu. Controllable self-assembly of NaREF₄ upconversion nanoparticles and their distinctive fluorescence properties. *Nanotechnology*, **27**, 295605 (2016)
69. Q. Ju, U. Uddayasankar, and U. Krull. Paper-based DNA detection using lanthanide-doped LiYF₄ upconversion nanocrystals as Bioprobe. *Small*, **10**, 3912–3917 (2014).
70. F. Heine, E. Heumann, T. Danger, T. Schweizer, G. Huber, and B. Chai. Green upconversion continuous wave Er³⁺:LiYF₄ laser at room temperature. *Appl. Phys. Lett.*, **383**, 1993–1995 (1995).
71. G. Chen, T. Y. Ohulchanskyy, A. Kachynski, Hans Agren, and P. N. Prasad. Intense visible and near-infrared upconversion photoluminescence in colloidal LiYF₄:Er³⁺ nanocrystals under excitation at 1490 nm. *ACS Nano.*, **5**, 4981–4986 (2011).

Bibliography

72. V. N. Makhov, A. S. Vanetsev, N. M. Khaidukov, M. Yin, X. T. Wei, A. Kotlov, and A. N. Belsky. Intrinsic and impurity luminescence of rare earth ions doped KYF₄ nanophosphors. *Radiat. Meas.*, **56**, 393–396 (2013).
73. B. Zhou, Y. Wang, and D. Xia. Colloidal β -KYF₄:Yb³⁺, Er³⁺/Tm³⁺ nanocrystals: tunable multicolor up-conversion luminescence from UV to NIR regions. *RSC Adv.*, **5**, 66807–66814 (2015).
74. B. Xu, F. Starecki, D. Pabœuf, P. Camy, J. L. Doualan, Z. P. Cai, A. Braud, R. Moncorgé, P. Goldner, and F. Bretenaker. Red and orange laser operation of Pr:KYF₄ pumped by a Nd:YAG/LBO laser at 469.1 nm and a InGaN laser diode at 444 nm. *Opt. Express*, **21**, 1052–1056 (2013).
75. R. U. Ichikawa, H. S. M. D. Linhares, I. Peral, S. L. Baldochi, I. M. Ranieri, X. Turrillas, and L. G. Martinez. Evidence for a core–shell configuration in Tb-doped KY₃F₁₀ nanoparticles using synchrotron X-ray line profile and pair distribution function analyses. *Mater. Res. Express*, **5**, 015006 (2018).
76. X. Xue, M. Liao, R. N. Tiwari, M. Yoshimura, T. Suzuki, and Y. Ohishi. Intense ultraviolet and blue upconversion emissions in Tb³⁺/Yb³⁺ codoped KY₃F₁₀ nanocrystals. *Appl. Phys. Express*, **5**, 092601 (2012).
77. L. Gomes, H. M. D. S. M. D. Linhares, R. U. Ichikawa, L. G. Martinez, and S. L. Baldochi. Luminescence properties of Yb:Er:KY₃F₁₀ nanophosphor and thermal treatment effects. *Opt. Mater.*, **54**, 57–66 (2016).
78. G. Wang, W. Qin, G. Wei, L. Wang, P. Zhu, R. Kim, D. Zhang, F. Ding, K. Zheng. Synthesis and upconversion luminescence properties of YF₃:Yb³⁺/Tm³⁺ octahedral nanocrystals. *J. Fluor. Chem.*, **130**, 158–161 (2009).
79. G. Wang, W. Qin, J. Zhang, J. Zhang, Y. Wang, C. Cao, L. Wang, G. Wei, P.

Bibliography

- Zhu, and R. Kim, Synthesis, growth mechanism, and tunable upconversion luminescence of Yb³⁺/Tm³⁺-codoped YF₃ nanobundles. *J. Phys. Chem. C.*, **112**, 12161–12167 (2008).
80. H. Shen, F. Wang, X. Fan, and M. Wang. Synthesis of LaF₃:Yb, Ln³⁺ nanoparticles with improved upconversion luminescence. *J. Exp. Nanosci.*, **2**, 303–311 (2007).
81. H. Hu, Z. Chen, T. Cao, Q. Zhang, M. Yu, F. Li, T. Yi, and C. Huang. Hydrothermal synthesis of hexagonal lanthanide-doped LaF₃ nanoplates with bright upconversion luminescence. *Nanotechnology*, **19**, 1–9 (2008).
82. G. S. Yi and G. M. Chow. Colloidal LaF₃:Yb, Er, LaF₃:Yb, Ho and LaF₃:Yb, Tm nanocrystals with multicolor upconversion fluorescence. *J. Mater. Chem.*, **15**, 4460–4464 (2005).
83. G. Wang, Q. Peng, and Y. Li. Upconversion luminescence of monodisperse CaF₂: Yb³⁺/Er³⁺ nanocrystals. *J. Am. Chem. Soc.*, **131**, 14200–14201 (2009).
84. M. Misiak, M. Skowicki, T. Lipiński, A. Kowalczyk, K. Prorok, S. Arabasz, and A. Bednarkiewicz. Biofunctionalized upconverting CaF₂:Yb,Tm nanoparticles for candida albicans detection and imaging. *Nano Res.*, **10**, 3333–3345 (2017).
85. D. Przybylska, A. Ekner-grzyb, B. F. Grześkowiak, and T. Grzyb. Upconverting SrF₂ nanoparticles of synthesis method, structural, spectroscopic and cytotoxicity studies. *Sci. Rep.*, **9**, 8669–8681 (2019).
86. G. Lucchini, A. Speghini, P. Canton, F. Vetrone, and M. Quintanilla. Engineering efficient upconverting. *Nanoscale Adv.*, **1**, 757-764 (2019).
87. O. S. Wenger and H. U. Gudel. Chemical tuning of the photon upconversion

Bibliography

- properties in Ti^{2+} -doped chloride host lattices. *Inorg. Chem.*, **40**, 5747–5753 (2001).
88. Y. Wang and J. Ohwaki. High efficiency infrared to visible upconversion of Er^{3+} in BaCl_2 . *J. Appl. Phys.*, **74**, 1272–1278 (1993).
89. Z. Chen, H. Jia, X. Zhang, J. Liu, S. Zeng, Y. Li, Z. Ma, G. Dong, and J. Qiu. $\text{BaCl}_2:\text{Er}^{3+}$ —a high efficient upconversion phosphor for broadband near-infrared photoresponsive devices. *J. Am. Ceram. Soc.*, **2513**, 2508–2513 (2015).
90. O. S. Wenger, C. Wickleder, K. W. Kramer, and H. U. Gudel. Upconversion in a divalent rare earth ion: optical absorption and luminescence spectroscopy of Tm^{2+} doped SrCl_2 . *J. Lumin.*, **95**, 101–105 (2001).
91. S. Moslemizadeh, V. Z. Mehdi, and J. Hassan. UV-Blue up-conversion phenomena in Nd^{3+} doped CaCl_2 Nano-Crystals. *Chinese J. Phys.*, **51**, 137–142 (2013).
92. J. Grimm, E. Beurer, P. Gerner, and H. U. Gudel. Upconversion between 4f–5d excited states in Tm^{2+} -doped CsCaCl_3 , CsCaBr_3 , and CsCaI_3 . *Chem. A Eur. J.*, **13**, 1152–1157 (2007).
93. R. Valiente, O. S. Wenger, and H. U. Gudel. Near-infrared-to-visible photon upconversion process induced by exchange interactions in Yb^{3+} -doped RbMnCl_3 . *Phys. Rev. B*, **63**, 165102 (2001).
94. E. Beurer, J. Grimm, P. Gerner, and H. U. Gudel. Absorption, light emission, and upconversion properties of Tm^{2+} doped CsCaI_3 and RbCaI_3 . *Inorg. Chem.*, **45**, 9901–9906 (2006).
95. H. Wang, M. Xing, X. Luo, X. Zhou, Y. Fu, T. Jiang, Y. Peng, Y. Ma, and X. Duan. Upconversion emission colour modulation of $\text{Y}_2\text{O}_2\text{S}:\text{Yb},\text{Er}$ under 1.55

Bibliography

- μm and 980 nm excitation. *J. Alloys Compd.*, **587**, 344–348 (2014).
96. Y. Tian, F. Lu, M. Xing, J. Ran, Y. Fu, Y. Peng, and X. Luo. Upconversion luminescence properties of $\text{Y}_2\text{O}_3\text{S}:\text{Er}^{3+}@\text{Y}_2\text{O}_3\text{S}:\text{Yb}^{3+},\text{Tm}^{3+}$ core-shell nanoparticles prepared via homogeneous co-precipitation. *Opt. Mater.*, **64**, 58–63 (2017).
97. G. Ajithkumar, B. Yoo, D. E. Goral, P. J. Hornsby, A. L. Lin, U. Ladiwala, V. P. Dravid and D. K. Sardar. Multimodal bioimaging using a rare earth doped luminescence and magnetic resonance properties. *J. Mater. Chem. B*, **2**, 1561–1572 (2013).
98. F. Wang, B. Yang, X. Chen, W. Ma, and B. Xu. Color-tunable and upconversion luminescence of $\text{Gd}_2\text{O}_3\text{S}:\text{Er},\text{Tb}$ phosphor. *Mater. Chem. Phys.*, **169**, 113–119 (2016).
99. M. Pokhrel, A. K. Gangadharan, and D. K. Sardar. High upconversion quantum yield at low pump threshold in $\text{Er}^{3+}/\text{Yb}^{3+}$ doped $\text{La}_2\text{O}_3\text{S}$ phosphor. *Mater. Lett.*, **99**, 86–89 (2013).
100. N. Hakmeh, C. Chlique, O. Merdrignac-Conanec, B. Fan, F. Cheviré X. Zhang, X. Fan, and X. Qiao. Combustion synthesis and up-conversion luminescence of $\text{La}_2\text{O}_3\text{S}:\text{Er}^{3+}, \text{Yb}^{3+}$ nanophosphors. *J. Solid State Chem.*, **226**, 225-261 (2015).
101. X. Wang, Q. Zhu, J. G. Li, Z. Hu, G. Zhu, and C. Wang. $\text{La}_2\text{O}_3\text{S}:\text{Tm}/\text{Yb}$ as a novel phosphor for highly pure near-infrared upconversion luminescence. *Scr. Mater.*, **149**, 121–124 (2018).
102. R. Anjana, K. M. Kurias, and M. K. Jayaraj. Clean synthesis of $\text{YOF}:\text{Er}^{3+}, \text{Yb}^{3+}$ upconversion colloidal nanoparticles in water through liquid phase pulsed laser ablation for imaging applications. *Opt. Mater.*, **72**, 730–736 (2017).

Bibliography

103. Z. Li, L. Zheng, L. Zhang, and L. Xiong. Synthesis, characterization and upconversion emission properties of $\text{Yb}^{3+}/\text{Er}^{3+}$ -codoped $\text{YF}_3\text{-YOF-Y}_2\text{O}_3$ system. *J. Lumin.*, **126**, 481–486 (2007).
104. L. Tao, W. Xu, Y. Zhu, L. Xu, H. Zhu, Y. Liu, S. Xu, P. Zhou and H. Song. Modulation of upconversion luminescence in Er^{3+} , Yb^{3+} -codoped lanthanide oxyfluoride (YOF, GdOF, LaOF) inverse opals. *J. Mater. Chem. C*, **2**, 4186–4195 (2014).
105. T. Grzyb and A. Tyminski. Up-conversion luminescence of GdOF:Yb^{3+} , Ln^{3+} ($\text{Ln} = \text{Ho, Tm, Er}$) nanocrystals. *J. Alloys Compd.*, **660**, 235–243 (2016).
106. K. Zheng, Y. Liu, Z. Liu, Z. Chen, and W. Qin. Color control and white upconversion luminescence of LaOF:Ln^{3+} ($\text{Ln} = \text{Yb, Er, Tm}$) nanocrystals prepared by the sol-gel Pechini method. *Dalt. Trans.*, **42**, 5159–5166 (2013).
107. J. Li, Z. Yang, Z. Chai, J. Qiu, and Z. Song. Preparation and upconversion emission enhancement of SiO_2 coated $\text{YbPO}_4:\text{Er}^{3+}$ inverse opals with Ag nanoparticles. *Opt. Mater. Express*, **7**, 78–83 (2017).
108. S. Lee, K. Teshima, N. Shikine, and S. Oishi. Fabrication of upconverting $\text{YbPO}_4:\text{Er}$ crystals by naturally-derived gel growth and subsequent thermal treatment. *Cryst. Growth Des.*, **9**, 4078–4083 (2009).
109. Z. Yang, K. Zhu, Z. Song, D. Zhou, Z. Yin, and J. Qiu. Effect of photonic bandgap on upconversion emission in $\text{YbPO}_4:\text{Er}$ inverse opal photonic crystals. *Appl. Opt.*, **50**, 287–290 (2011).
110. S. Heer, O. Lehmann, M. Haase, and H. U. Gudel. Blue, green, and red upconversion emission from lanthanide-doped LuPO_4 and YbPO_4 nanocrystals in a transparent colloidal solution. *Angew. Chem. Int. Ed.*, **42**, 3179–3182

Bibliography

- (2003).
111. Z. Zhang, R. Cao, L. Guo, P. Li, C. Liang, and T. Li. Enhanced upconversion luminescence in $\text{LuPO}_4:\text{Ln}^{3+}$ phosphors via optical-inert ions doping. *New J. Chem.*, **42**, 15215–15220 (2018).
 112. Y. Gao, H. Yu, C. Shi, G. Zhao, Y. Bi, B. Xu, F. Ding, Y. Sun, and Z. Xu. Synthesis and luminescent properties of uniform monodisperse $\text{LuPO}_4:\text{Eu}^{3+}/\text{Tb}^{3+}$ hollow microspheres. *R. Soc. open Sci.*, **4**, 171451 (2017).
 113. P. Ghosh, J. Oliva, E. D. Rosa, K. K. Haldar, D. Solis, and A. Patra. Enhancement of upconversion emission of $\text{LaPO}_4:\text{Er@Yb}$ core-shell nanoparticles/nanorods. *J. Phys. Chem. C*, **112**, 9650–9658 (2008).
 114. L. Yu, H. Song, S. Lu, Z. Liu, L. Yang, and X. Kong. Luminescent properties of $\text{LaPO}_4:\text{Eu}$ nanoparticles and nanowires. *J. Phys. Chem. B*, **108**, 16697–16702 (2004).
 115. R. D. Shannon. Revised effective ionic radii and systematic studies of interatomic distances in halides and chalcogenides. *Acta Cryst.*, **32**, 751–767 (1976).
 116. A. Patra, C. S. Friend, R. Kapoor, and P. N. Prasad. Upconversion in $\text{Er}^{3+}:\text{ZrO}_2$ nanocrystals. *J. Phys. Chem. B*, **106**, 1909–1912 (2002).
 117. P. R. Diamente, M. Raudsepp, and F. C. J. M. V. Veggel. Dispersible Tm^{3+} -doped nanoparticles that exhibit strong 1.47 μm photoluminescence. *Adv. Funct. Mater.*, **17**, 363–368 (2007).
 118. K. Biswas, A. D. Sontakke, J. Ghosh, and K. Annapurna. Enhanced blue emission from transparent oxyfluoride glass-ceramics containing $\text{Pr}^{3+}:\text{BaF}_2$ nanocrystals. *J. Am. Ceram. Soc.*, **93**, 1010–1017 (2010).

Bibliography

119. P. Du, Y. Wu, and J. S. Yu. Synthesis and luminescence properties of Eu^{3+} -activated BiF_3 nanoparticles for optical thermometry and fluorescence imaging in rice root. *RSC Adv.*, **8**, 6419–6424 (2018).
120. S. Heer, K. Kömpe, H. U. Güdel, and M. Haase. Highly efficient multicolour upconversion emission in transparent colloids of lanthanide-doped NaYF_4 nanocrystals. *Adv. Mater.*, **16**, 2102–2105 (2004).
121. K. W. Kramer, D. Biner, G. Frei, H. U. Güdel, M. P. Hehlen, and S. R. Luthi. Hexagonal sodium yttrium fluoride based green and blue emitting upconversion phosphors. *Chem. Mater.*, **16**, 1244–1251 (2004).
122. C. Homann, L. Krukewitt, F. Frenzel, B. Grauel, C. Würth, U. Resch-Genger, M. Haase. $\text{NaYF}_4:\text{Yb,Er}/\text{NaYF}_4$ core/shell nanocrystals with high upconversion luminescence quantum yield. *Angew. Chem. Int. Ed.*, **57**, 8765–8769 (2018).
123. G. Yi, H. Lu, S. Zhao, Y. Ge, W. Yang, D. Chen, and L. H. Guo. Synthesis, characterization, and biological application of size-controlled nanocrystalline $\text{NaYF}_4:\text{Yb, Er}$ phosphors. *Nano Lett.*, **4**, 2191–2196 (2004).
124. G. H. Dieke and H. M. Crosswhite. The spectra of the doubly and triply ionized rare earths. *Appl. Opt.*, **2**, 675–686 (1963).
125. Z. Hou, Y. Zhang, K. Deng, Y. Chen, X. Li, X. Deng, Z. Cheng, H. Lian, C. Li, and J. Lin. UV-emitting upconversion-based TiO_2 photosensitizing nanoplatfrom: near-infrared light mediated in vivo photodynamic therapy via mitochondria-involved apoptosis pathway. *ACS Nano.*, **9**, 2584–2599 (2015).
126. J. M. F. Van Dijk, and M. F. H. Schuurmans. On the nonradiative and radiative decay rates and a modified exponential energy gap law for 4f-4f transitions in rareearth ions. *J. Chem. Phys.*, **78**, 5317–5323 (1983).

Bibliography

127. J. F. Suyver, J. Grimm, M. K. van Veen, D. Biner, K.W. Kramer, and H. U. Gudel. Upconversion spectroscopy and properties of NaYF₄ doped with Er³⁺, Tm³⁺ and/or Yb³⁺. *J. Lumin.*, **117**, 1–12 (2006).
128. Y. Zhang, B. Chen, S. Xu, X. Li, J. Zhang, J. Sun, H. Zheng, L. Tong, G. Sui, H. Zhong, H. Xia, and R. Hua. Dually functioned core-shell NaYF₄:Er³⁺/Yb³⁺@NaYF₄:Tm³⁺/Yb³⁺ nanoparticles as nano-calorifiers and nano-thermometers for advanced photothermal therapy. *Sci. Rep.*, **7**, 1–12 (2017).
129. C. Strohhofer, A. Polman. Absorption and emission spectroscopy in Er³⁺-Yb³⁺ doped aluminum oxide waveguides. *Opt. Mater.*, **21**, 705–712 (2003).
130. J. Ohwaki and Y. Wang. 1.3 μm to visible upconversion in Dy³⁺ and Er³⁺ codoped BaCl₂ phosphor. *Appl. Phys. Lett.*, **129**, 3–6 (2014).
131. J. Ohwaki and M. Otsuka. Efficient 1.3 μm to visible upconversion in Dy³⁺- and Er³⁺- codoped YBr₃ phosphor. *Electron. Lett.*, **31**, 752–753 (1995).
132. S. Sivakumar, F. C. J. M. van Veggel, and P. S. May. Near-infrared (NIR) to red and green up-conversion emission from silica sol-gel thin films made with La_{0.45}Yb_{0.50}Er_{0.05}F₃ nanoparticles, hetero-looping-enhanced energy transfer (Hetero-LEET): a new up-conversion process. *J. Am. Chem. Soc.*, **129**, 620–625 (2007).
133. D. Li, C. Ding, G. Song, S. Lu, Z. Zhang, Y. Shi, H. Shen, Y. Zhang, H. Ouyang, and H. Wang. Controlling the morphology of erbium-doped yttrium fluoride using acids as surface modifiers: employing adsorbed chlorine ions to inhibit the quenching of upconversion fluorescence. *J. Phys. Chem. C*, **114**, 21378–21384 (2010).

Bibliography

134. P. Du, and J. S. Yu. Synthesis of Er(III)/Yb(III)-doped BiF₃ upconversion nanoparticles for use in optical thermometry. *Microchim. Acta*, **185**, 237 (2018).
135. S. Sarkar, A. Dash, and V. Mahalingam. Strong Stokes and upconversion luminescence from ultrasmall Ln³⁺-doped BiF₃ (Ln=Eu³⁺, Yb³⁺/Er³⁺) nanoparticles confined in a polymer matrix. *Chem. - An Asian J.* **9**, 447–451 (2014).
136. A. Boccolini, E. Favilla, M. Tonelli, B. S. Richards, and R. R. Thomson. Highly efficient upconversion in Er³⁺ doped BaY₂F₈ single crystals: dependence of quantum yield on excitation wavelength and thickness. *Opt. Express*, **23**, 16715–16721 (2015).
137. T. Soukka, K. Kuningas, T. Rantanen, V. Haaslahti, and T. Lovgren. Photochemical characterization of up-converting inorganic lanthanide phosphors as potential labels. *J. Fluoresc.*, **15**, 513-528 (2005).
138. K. Kuningas, T. Rantanen, T. Ukonaho, T. Lovgren, and T. Soukka. Homogeneous assay technology based on upconverting phosphors. *Anal. Chem.*, **77**, 7348–7355 (2005).
139. J. Vuojola. Luminescent lanthanide reporters: new concepts for use in bioanalytical applications. PhD thesis, Finland (2013).
140. T. Soukka, H. Harma, J. Paukkunen, and T. Lovgren. Utilization of kinetically enhanced monovalent binding affinity by immunoassays based on multivalent nanoparticle-antibody bioconjugates. *Anal. Chem.* **73**, 2254–2260 (2001).
141. H. J. M. A. A. Zijlmans, J. Bonnet, J. Burton, K. Kardos, T. Vail, R. S. Niedbala, and H. J. Tanke. Detection of cell and tissue surface antigens using

Bibliography

- up-converting phosphors : a new reporter technology. *Anal. Biochem.*, **267**, 30–36 (1999).
142. A. Sedlmeier, D. E. Achatz, L. H. Fischer, H. H. Gorris, and O. S. Wolfbeis. Photon upconverting nanoparticles for luminescent sensing of temperature. *Nanoscale*, **4**, 7090–7096 (2012).
143. H. S. Mader and O. S. Wolfbeis. Letters to analytical chemistry optical ammonia sensor based on upconverting luminescent nanoparticles. *Anal. Chem.*, **82**, 5002–5004 (2010).
144. D. E. Achatz, R. J. Meier, L. H. Fischer, and O. S. Wolfbeis. Luminescent sensing of oxygen using a quenchable probe and upconverting nanoparticles. *Angew. Chem. Int. Ed.*, **50**, 260–263 (2011).
145. J. Zhou, M. Yu, Y. Sun, X. Zhang, X. Zhu, Z. Wu, D. Wu and F. Li. Biomaterials fluorine-18-labeled $Gd^{3+}/Yb^{3+}/Er^{3+}$ co-doped $NaYF_4$ nanophosphors for multimodality PET/MR/UCL imaging. *Biomaterials*, **32**, 1148–1156 (2011).
146. M. Pollnau, D. R. Gamelin, S. R. Lüthi, and H. U. Güdel. Power dependence of upconversion luminescence in lanthanide and transition-metal-ion systems. *Phys. Rev. B.*, **61**, 3337–3346 (2000).
147. M. Polinau, W. Luthy, H. P. Weber, K. Kramer, H. U. Güdel, and R. A. McFarlane. Excited-state absorption in $Er:BaY_2F_8$ and $Cs_3Er_2Br_9$ and comparison with $Er:LiYF_4$. *Appl. Phys. B.*, **62**, 339–344 (1996).
148. Y. Mita, K. Hirama, N. Ando, H. Yamamoto, and S. Shionoya. Luminescence processes in Tm^{3+} and Er^{3+} ionactivated, Yb^{3+} ion sensitized infrared upconversion devices. *J. Appl. Phys.*, **74**, 4703–4709 (1993).

Bibliography

149. E. Downing, L. Hesselink, J. Ralston and R. Rojer. A three-color, solid-state, three-dimensional display. *Science*, **273**, 1185–1190 (1996).
150. S. Xie, G. Gong, Y. Song, H. Tan, C. Zhang, N. Li, Y. Zhang, L. Xu, J. Xu, J. Zheng. Design of novel lanthanide-doped core-shell nanocrystals with dual up-conversion and down-conversion luminescence for anti-counterfeiting printing. *Dalt. Trans.*, **48**, 6971–6983 (2019).
151. J. M. Meruga, A. Baride, W. Cross, J. J. Kellar, and P. S. May. Red-green-blue printing using luminescence-upconversion inks. *J. Mater. Chem. B*, **2**, 2221–2227 (2014).
152. Y. Shang, S. Hao, C. Yang, and G. Chen. Enhancing solar cell efficiency using photon upconversion materials. *Nanomaterials*, **5**, 1782–1809 (2015).
153. T. Saga. Advances in crystalline silicon solar cell technology for industrial mass production. *NPG Asia Mater.*, **2**, 96–102 (2010).
154. G. Chen, J. Seo, C. Yang and P. N. Prasad. Nanochemistry and nanomaterials for photovoltaics. *Chem. Soc. Rev.*, **42**, 8304–8338 (2013).
155. W. G. Van Sark, J. de Wild, J. K. Rath, A. Meijerink, and R. E. Schropp. Upconversion in solar cells. *Nano Res. Lett.*, **8**, 1–10 (2013).
156. S. Asahi¹, H. Teranishi¹, K. Kusaki¹, T. Kaizu¹ and T. Kital. Two-step photon up-conversion solar cells. *Nat. Commun.*, **8**, 14962 (2017).
157. P. Ramasamy, P. Manivasakan, and J. Kim. Upconversion nanophosphors for solar cell applications. *RSC Adv.*, **4**, 34873–34895 (2014).
158. Y. Y. Cheng, A. Nattestad, T. F. Schulze, R. W. MacQueen, B. Fockel, K. L. G. Wallace, T. Khoury, M. J. Crossley, and T. W. Schmidt. Increased upconversion performance for thin film solar cells: a tri-molecular composition.

Bibliography

- Chem. Sci.*, **7**, 559–568 (2016).
159. J. F. Suyver, A. Aebischer, D. Biner, P. Gerner, J. Grimm, S. Heer, K.W. Kramer, C. Reinhard, and H. U. Gudel. Novel materials doped with trivalent lanthanides and transition metal ions showing near-infrared to visible photon upconversion. *Opt. Mater.*, **27**, 1111–1130 (2005).
160. Y. T. Prabhu, K. V. Rao, V. S. S. Kumar, and B. S. Kumari. X-Ray analysis by Williamson-hall and size-strain plot methods of ZnO nanoparticles with fuel variation. *World J. Nano Sci. Eng.*, **04**, 21–28 (2014).
161. J. C. de Mello, H. F. Wittmann, and R. H. Friend. An improved experimental determination of external photoluminescence quantum efficiency. *Adv. Mater.*, **09**, 230–232 (1997)
162. H. Schäfer, P. Ptacek, O. Zerzouf, and M. Haase. Synthesis and optical properties of KYF₄/Yb, Er nanocrystals, and their surface modification with undoped KYF₄. *Adv. Funct. Mater.*, **18**, 2913–2918 (2008).
163. Y. L. Fur, N. M. Khaidukov and S. Aléonard. Structure of KYF₄. *Acta Crystallogr.*, **48**, 978–982 (1992).
164. E. V. Samsonova, A. V. Popov, A. S. Vanetsev, K. Keevend, K. Kaldvee, L. Puust, A. E. Baranchikov, A. V. Ryabova, S. G. Fedorenko, V. Kiisk, I. Sildos, J. Kikas, R. Steiner, V. B. Loschenov, and Y. V. Orlovskii. Fluorescence quenching mechanism for water-dispersible Nd³⁺:KYF₄ nanoparticles synthesized by microwave-hydrothermal technique. *J. Lumin.*, **169**, 722–727 (2016).
165. S. Guo, C. Cao, and R. Cao. Synthesis and optical properties of Eu³⁺ doped NaYF₄ and KYF₄ micro/nanocrystals. *J. Nanosci. Nanotechnol.*, **16**,

Bibliography

- 3857–3860 (2016).
166. Y. Wang, Y. Liu, Q. Xiao, H. Zhu, R. Li. and X. Chen. Eu^{3+} doped KYF_4 nanocrystals: synthesis, electronic structure, and optical properties. *Nanoscale*, **3**, 3164–3169 (2011).
167. J. Maixner and V. Bartuneek. X-ray powder diffraction data for potassium erbium fluoride. *Powder Diffr.*, **28**, 305–306 (2013).
168. Y. Q. Jia. Crystal radii and effective ionic radii of the rare earth ions. *J. Solid State Chem.*, **95**, 184–187 (1991).
169. L. Huang, T. Yamashita, R. Jose, Y. Arai, T. Suzuki, and Y. Ohishi. Intense ultraviolet emission from Tb^{3+} and Yb^{3+} co-doped glass ceramic containing CaF_2 nanocrystals. *Appl. Phys. Lett.*, **91**, 1–3 (2007).
170. J. Zhao, Z. Lu, Y. Yin, C. McRae, J. A. Piper, J. M. Dawes, D. Jin, and E. M. Goldys. Upconversion luminescence with tunable lifetime in $\text{NaYF}_4:\text{Yb},\text{Er}$ nanocrystals: role of nanocrystal size. *Nanoscale*, **5**, 944–952 (2013).
171. A. Escudero, E. Moretti, and M. Ocaña. Synthesis and luminescence of uniform europium-doped bismuth fluoride and bismuth oxyfluoride particles with different morphologies. *Cryst. Eng. Comm.*, **16**, 3274–3283 (2014).
172. M. F. Oszajca, K. V. Kravchyk, M. Walter, F. Krieg, M. I. Bodnarchuk and M. V. Kovalenko. Colloidal BiF_3 nanocrystals: a bottom-up approach to conversion-type Li-ion cathodes. *Nanoscale*, **7**, 16601–16605 (2015).
173. C. Feng, F. Teng, Z. Liu, C. Chang, Y. Zhao, S. Wang, M. Chen, W. Yao, and Y. Zhu. A newly discovered BiF_3 photocatalyst with a high positive valence band. *J. Mol. Catal. A Chem.*, **401**, 35–40 (2015)
174. P. Lei, P. Zhang, S. Yao, S. Song, L. Dong, X. Xu, X. Liu, K. Du, J. Feng, and

Bibliography

- H. Zhang. Optimization of Bi^{3+} in upconversion nanoparticles induced simultaneous enhancement of near-infrared optical and X-ray computed tomography imaging capability. *ACS Appl. Mater. Interfaces*, **8**, 27490–27497 (2016).
175. N. Niu, F. He, S. Gai, C. Li, X. Zhang, S. Huang and P. Yang. Rapid microwave reflux process for the synthesis of pure hexagonal $\text{NaYF}_4:\text{Yb}^{3+}$, Ln^{3+} , Bi^{3+} ($\text{Ln}^{3+} = \text{Er}^{3+}$, Tm^{3+} , Ho^{3+}) and its enhanced UC luminescence. *J. Mater. Chem.*, **22**, 21613–21623 (2012).
176. L. Jiang, S. Xiao, X. Yang, J. Ding, and K. Dong. Enhancement of up-conversion luminescence in $\text{Zn}_2\text{SiO}_4:\text{Yb}^{3+}$, Er^{3+} by co-doping with Li^+ or Bi^{3+} . *Appl. Phys. B Lasers Opt.*, **107**, 477–481 (2012)
177. J. Del-Castillo, A. C. Yanes, S. Abe, and P. E. Smet. Site selective spectroscopy in $\text{BaYF}_5:\text{RE}^{3+}$ ($\text{RE} = \text{Eu}$, Sm) nano-glass-ceramics. *J. Alloys Compd*, **635**, 136–141 (2015).
178. H. Du, W. Zhang and J. Sun. Structure and upconversion luminescence properties of $\text{BaYF}_5:\text{Yb}^{3+}$, Er^{3+} nanoparticles prepared by different methods. *J. Alloys Compd*, **509**, 3413–3418 (2011).
179. W. Zhang, S. Ouyang, Z. Zhang, Y. Zhang, and H. Xia. Luminescent properties of Eu^{3+} -doped glass ceramics containing BaGdF_5 nanocrystals under NUV-excitation for W-LEDs. *Ceram. Int.*, **41**, 14035–14040 (2015).
180. J. Yao, F. Zhao, C. Pan, and J. Zhuang. Controlled synthesis of $\text{BaYF}_5:\text{Er}^{3+}$, Yb^{3+} with different morphology for the enhancement of upconversion luminescence. *Nanoscale Res. Lett.*, **12**, 1–6 (2017).
181. G. Chen, H. Agren, T. Y. Ohulchansky, and P. N. Prasad. Light upconverting

Bibliography

- core-shell nanostructures: nanophotonic control for emerging applications. *Chem. Soc. Rev.*, **44**, 1680–1713 (2015).
182. J.-C. Boyer and F. C. J. M. van Veggel. Absolute quantum yield measurements of colloidal $\text{NaYF}_4:\text{Er}^{3+},\text{Yb}^{3+}$ upconverting nanoparticles. *Nanoscale*, **2** 1417-1419 (2017)

Appendix

List of abbreviations

NIR	near infrared
VIS	visible
UCNs	up-conversion nanoparticles
ESA	excited-state absorption
ETU	energy-transfer up-conversion
PA	photon avalanche
IR	infrared
IRQC	infrared quantum counter
APTE	addition de photons par transferts d'énergie
Ln	lanthanide
Hetero-LEET	hetero-looping-enhanced-energy-transfe -r
PET	positron emission tomography
UCL	up-conversion luminescence
LD	laser diodes
LED	light-emitting diodes
CSNPs	core-shell nanoparticles
PV	photovoltaic
RE	rear earth
RT	room temperature

Appendix

EG	ethylene glycol
DW	deionized water
XRD	X-ray diffraction
FWHM	full-widths at half-maximum
TEM	transmission electron microscope
QY	quantum yield
UCQY	up-conversion quantum yield

Synthèse et Caractérisation de Différentes Nanoparticules Up-conversion à Base de Fluorures Cubiques Dopés Yb/Er dans le NIR au VIS

Remerciements

Ce travail a été réalisé à l'Institut de Recherche de Chimie Paris (IRCP), Chimie-Paristech CNRS de l'Université Paris-Sciences-et-Lettres (PSL), sous la direction des Professeurs Michel Mortier et Patrick Gredin.

Tout d'abord, je voudrais exprimer mes profonds et sincères remerciements à mes superviseurs, les Professeurs Michel Mortier et Patrick Gredin, pour leur aide et leurs conseils continus.

Par ailleurs, je tiens également à exprimer mes sincères remerciements aux Professeurs Géraldine Dantelle, Nathalie Dupond et Souad Ammar pour la révision de la thèse et pour leurs précieux commentaires. Je tiens à remercier Karmel de Oliveira Lima pour son aide et ses conseils pour ce travail de thèse. Je tiens à remercier le Prof. Gerard Aka pour son attention et son aide.

Je remercie Patrick Aschehoug pour son aide dans le domaine des spectres de photoluminescence et de la caractérisation de la durée de vie de la luminescence. J'exprime ma gratitude à Patricia Beaunier et Philippe Vermaut pour leur aide dans l'acquisition et l'analyse d'images obtenues par microscopie électronique à transmission (TEM). Professeurs Zhuoying Chen et Dr. Hengyang Xiang de l'ESPCI pour leur aide dans la mesure du rendement quantique interne.

Je remercie les collègues et le personnel de l'IRCP pour la bonne ambiance de travail. Je remercie le China Scholar Council d'avoir financé et soutenu ce travail de thèse pendant les trois ans. Je tiens également à remercier vivement mes parents pour leur soutien et leur encouragement sans faille tout au long de ce travail.

Content

Introduction.....	3
Chapitre 1 État de l'art de la conversion ascendante dans les solides dopés par des terres rares.....	5
1.1 Historique et évolution de la conversion ascendante dans les solides dopés par des terres rares.....	5
1.2 Nanoparticules de conversion ascendante à base de fluorure.....	6
Chapitre 2 Section expérimentale.....	8
2.1 Réactifs et matrices.....	8
2.2 Expérience de caractérisation.....	8
Chapitre 3 Résultats et discussion.....	10
3.1 KYF ₄ :10% Yb/5%Er.....	10
3.2 BiF ₃ :10% Yb/5%Er.....	10
3.3 K _{0.3} Bi _{0.7} F _{2.4} :10% Yb/5%Er.....	11
3.4 particules cœur – coquille BaYF ₅ :20% Yb/2%Er/ BaYF ₅	12
Chapitre 4 Perspective des UCNs.....	13

Introduction

La conversion ascendante est un procédé d'émission de type anti-Stokes où les ions activateurs dopés absorbent deux photons ou plus d'une source de faible énergie pour émettre une lumière de haute énergie.¹⁻¹⁴ Elle a été découverte et développée par le Dr Auzel en 1966. Puis, il a présenté les principes et l'application de la conversion ascendante de façon indépendante.^{8,13}

Les nanoparticules de conversion ascendante (UCNs) ont fait l'objet d'une attention considérable ces dernières années en raison de leurs nombreux avantages. Parmi la multitude de matériaux hôtes signalés, les nanoparticules de fluorure en particulier obtiennent des attentions croissantes principalement pour leur faible énergie phononique de réseau qui peut réduire les pertes non radiatives et donc améliorer l'efficacité de la photoluminescence.¹⁵ Bien que de nombreux efforts aient été consacrés à l'étude des matériaux de conversion ascendante, on est encore loin des applications profondes pour les raisons suivantes. Tout d'abord, les méthodes de synthèse actuellement largement utilisées sont lourdes et contraignantes en terme de matériel et de contrôle des paramètres de synthèse (atmosphère, présence d'eau, etc...)^{4,16} Deuxièmement, l'emploi de solvants organiques complexes fréquemment utilisés peut présenter des dangers potentiels lorsqu'ils sont utilisés à haute température¹⁷.

Le premier objectif de cette thèse est de synthétiser et de caractériser quelques nouveaux UCNs à base de fluorure co-dopés avec des paires Yb/Er pour réaliser la conversion du proche infrarouge en lumière visible. Après avoir réalisé le premier objectif, le second objectif est de sélectionner des UCNs optimaux à partir des composés préparés, qui devraient posséder une forte émission, une longue durée de vie de luminescence, et un rendement quantique élevé de conversion ascendante. Ces

UCNs ont des applications potentielles en imagerie biologique, qui nécessite de petites nanoparticules, et dans les cellules solaires, qui ont besoin d'une longue durée de vie.

Cette thèse a été organisée comme suit : Après une introduction, le chapitre 1 a résumé le développement et l'état de l'art de la conversion ascendante dans les solides dopés à l'erbium. Le contexte historique et le développement de la conversion ascendante ont été exposés. Les trois mécanismes classiques normaux de l'ESA (absorption à l'état excité), de l'ETU (up-conversion par transfert d'énergie) et de la PA (avalanche de photons) ont été présentés. La constitution des matériaux usuels de conversion ascendante, y compris les matrices hôtes, les activateurs et les sensibilisateurs ont été présentés, respectivement. Par ailleurs, certaines applications potentielles des UCNs ont été présentées.

Le chapitre 2 a décrit les détails des réactifs et composés utilisés, les méthodes de synthèse et les approches de caractérisation expérimentale dans ce travail de thèse.

Le chapitre 3 discute spécifiquement les résultats obtenus pour les quatre séries des UCN préparées, c'est-à-dire $\text{KYF}_4:\text{Yb/Er}$, $\text{BiF}_3:\text{Yb/Er}$, $\text{K}_{0.3}\text{Bi}_{0.7}\text{F}_{2.4}:\text{Yb/Er}$, et $\text{BaYF}_5:\text{Yb/Er}@\text{BaYF}_5$. La structure de la phase nanocristalline, la taille moyenne calculée des cristallites, la morphologie, la distribution de taille des nanoparticules, les spectres d'absorption, le rendement quantique interne, les spectres d'émission et les temps de décroissance ont été analysés et discutés. Par ailleurs, les effets de la taille des nanoparticules sur la photoluminescence ont été analysés.

Le chapitre 4 donne une conclusion générale sur l'ensemble du travail et la perspective d'utilisation des UCNs.

Chapitre 1 État de l'art de la conversion ascendante dans les solides dopés aux terres rares

1.1 Historique et évolution de la conversion ascendante dans les solides dopés aux terres rares

Pour les émetteurs de lumière à fluorescence, les solides dopés aux terres rares suivent généralement le principe bien connu de la loi de Stokes qui stipule simplement que les photons d'excitation sont à une énergie supérieure à celle des photons émis.¹⁸

Néanmoins, la conversion ascendante est un processus d'émission de type anti-Stokes dans lequel les photons émis sont à une énergie plus élevée que les photons excitants.^{6,10-12} Le concept d'émission de conversion ascendante est parti de l'idée que les photons infrarouges (IR) pouvaient être détectés et comptés par absorption séquentielle dans les niveaux d'énergie des ions donnés par Bloembergen en 1959.¹⁹ Cependant, il était assez difficile de réaliser une absorption séquentielle des photons avec un unique ion dopant pendant la durée de vie limitée du premier état excité^{12,13}

En 1966, Auzel a découvert que l'intensité de la luminescence des ions Er^{3+} , Ho^{3+} et Tm^{3+} était presque augmentée de deux ordres de grandeur avec un co-dopage Yb^{3+} dans la matrice hôte sous excitation de lumière proche infrarouge.¹²⁻¹⁴ Jusqu'alors, Auzel a proposé que le transfert d'énergie puisse se produire entre deux ions et a fait reconnaître le rôle du transfert d'énergie. On a constaté que les énergies émises dépassent les énergies d'excitation de 10 à 100 fois kT dans le processus de conversion ascendante.

1.2 Nanoparticules à conversion ascendante fluorées

En comparaison avec les sulfures, les oxydes et les phosphures, les nanoparticules fluorées sont particulièrement intéressantes en raison de la faible énergie des phonons des fluorures, qui se situe généralement entre 300 et 400 cm^{-1} .^{11,20} La faible énergie de phonons des fluorures peut réduire les pertes non radiatives et donc améliorer l'efficacité de la luminescence.¹⁵ En combinaison avec une grande stabilité chimique et thermique et des raies d'émission étroites, les fluorures sont particulièrement adaptés à la conversion NIR/visible.

De nombreux types de nanoparticules fluorées à conversion ascendante ont été développés, les nanoparticules de fluorure de type NaREF_4 ont fait l'objet du plus grand nombre de recherches et NaYF_4 hexagonal co-dopé Yb/Er s'est avéré être le matériau à conversion ascendante le plus efficace jusqu'à présent.^{21,22} Par exemple, le rendement quantique de conversion ascendante interne des nanoparticules les plus efficaces $\beta\text{-NaYF}_4:20\% \text{Yb}/2\% \text{Er}$ à 540 nm est de 0.3 % avec un laser sous excitation à 980 nm.²³

Par conséquent, les nanoparticules à conversion ascendante nécessitent des études plus nombreuses et plus approfondies pour optimiser les propriétés de photoluminescence, comme l'augmentation de la durée de vie de la luminescence et l'amélioration de l'efficacité de conversion. Cependant, les types de matrices hôtes possibles sont nombreuses et variées, même en ce qui concerne les matériaux fluorés. C'est pourquoi il faudrait concentrer davantage de recherches sur la synthèse et le développement de nouvelles matrices hôtes. Cela pourrait aider à surmonter les limites actuelles auxquelles font face les UCNs et à accélérer le développement pour obtenir des matrices hôtes idéales.

Au cours des dernières années, de nombreuses nouvelles matrices hôtes ont fait

l'objet de recherches et de rapports. Dans ce travail, le premier objectif de cette thèse est de préparer plusieurs nouvelles matrices hôtes. Les nanoparticules à conversion ascendante KYF_4 , BiF_3 , $\text{K}_{0.3}\text{Bi}_{0.7}\text{F}_{2.4}$, et BaYF_5 co-dopées avec Yb et Er seront synthétisées dans cette thèse.

Chapitre 2 Section expérimentale

2.1 Réactifs et matériaux

La pureté des réactifs $\text{KNO}_3 \cdot 6\text{H}_2\text{O}$, $\text{Y}(\text{NO}_3)_3 \cdot 6\text{H}_2\text{O}$, $\text{Er}(\text{NO}_3)_3 \cdot 6\text{H}_2\text{O}$, $\text{Yb}(\text{NO}_3)_3 \cdot 6\text{H}_2\text{O}$, $\text{Bi}(\text{NO}_3)_3 \cdot 6\text{H}_2\text{O}$ et NH_4F est de 99,99 %. $\text{Ba}(\text{NO}_3)_2 \cdot 6\text{H}_2\text{O}$ a une pureté de 99,999 %. L'éthanol et l'éthylène glycol sont de pureté ≥ 99 %. L'acide oléique a une pureté de 90 %. Le cyclohexane est pur à 100 % (anhydre). L'éthanol anhydre absolu présente une pureté de 99.9 %.

2.2 Expérience de caractérisation

Les diagrammes de diffraction des rayons X (XRD) sur poudres ont été enregistrés sur un diffractomètre X'Pert Pro (Panalytical) avec un rayonnement $\text{Cu K}\alpha$ ($\lambda = 1.5406 \text{ \AA}$) (40 kV, 45 mA). Le programme Fullprof Suite a été utilisé pour affiner le profil des diagrammes de diffraction des rayons X.

La méthode Williamson-Hall a été utilisée pour calculer la taille moyenne des cristallites.²⁴

Les images du microscope électronique à transmission (TEM) ont été réalisées sur un microscope JEOL JEM 2100Plus (équipé d'un filament LaB_6) fonctionnant à 200 kV. Les images ont été enregistrées à l'aide d'une caméra CCD de 4008×2672 pixels (Gatan Orius SC1000). L'histogramme de distribution de taille a été tracé à partir des images TEM avec le logiciel ImageJ. Les spectres d'absorption ont été mesurés avec un spectrophotomètre Cary 6000i UV-Vis-NIR.

Les rendements quantiques internes (QY) des poudres préparées ont été calculés à partir des spectres d'émission enregistrés sur un spectrophotomètre Cary 6000i équipé d'une sphère d'intégration. La source laser d'excitation de $\sim 974 \text{ nm}$ avec une

puissance de 1080 mA provenait d'une diode laser stabilisée en température à l'aide d'un contrôleur de température de la technologie laser en mode unique. Un spectromètre Ocean Optics HR 4000 (200 - 1100 nm) a été utilisé pour enregistrer les spectres d'émission.

Les spectres d'émission utilisés pour les mesures des temps de vie de fluorescence, ont tous été excités à l'aide d'un laser OPO Ekspla NT342B accordable avec une durée d'impulsion de 7 ns. Une caméra CCD (Princeton Instruments) équipée d'un monochromateur (Acton Research, 300 lignes/mm) a été utilisée pour enregistrer les spectres de fluorescence. Un photomultiplicateur RCA 8850 a été utilisé pour les mesures de décroissance de fluorescence. Toutes les mesures ont été effectuées à la température ambiante.

Chapitre 3 Résultats et discussion

3.1 KYF₄:10%Yb/5%Er

Dans cette partie, les résultats et l'analyse des UCNs KYF₄ codopés en Yb/Er ont été présentés. Dans un premier temps, on a constaté que une synthèse dans un mélange de solvants eau-éthanol était nécessaire pour obtenir la phase KYF₄ cubique pure. Les tailles moyennes calculées des cristallites sont en bonne concordance avec la distribution des tailles obtenues d'après les images TEM. Les échantillons de la série B, en particulier le B₁, présentent une bonne morphologie. L'échantillon B₁ s'est avéré posséder la plus haute intensité de photoluminescence dans les raies d'émission verte (543 nm) ou rouge (666 nm). Les excellentes durées de vie, 79 μ s à 543 nm et 312 μ s à 666 nm, appartenaient à l'échantillon B₁ recuit. Ces propriétés souhaitables font que le composé B₁ a un potentiel prometteur dans les applications candidates. La QY interne des échantillons B₁ est de 0.20 % à 543 nm et de 0.14 % à 666 nm. Les effets de la taille des nanoparticules sur la durée de vie ont également été discutés.

3.2 BiF₃:10%Yb/5%Er

Dans le chapitre 3.2, des nanoparticules cubiques de BiF₃ non dopées et codopées à 10%Yb/5%Er ont été préparées avec succès dans un milieu constitué d'un mélange d'éthylène glycol et d'eau déionisée. Avec une méthode de coprécipitation rapide à température ambiante, des synthèses avec des rapports Bi/F différents ont été testées. Cependant, les échantillons préparés montrent une large distribution de taille de nanoparticules.

Les composés obtenus présentent des pics d'émission caractéristiques des UCNs

codopés Yb/Er à 543 nm et 666 nm, excités sous un laser pulsé de 974 nm. L'échantillon D a la plus grande efficacité à 666 nm et l'échantillon E a la plus grande efficacité relative à 408 nm et 543 nm. Par ailleurs, les pics d'émission à 378 nm et 408 nm sont également observés. Enfin, les durées de vie moyennes de la photoluminescence ont été présentées. Elle suggère que l'échantillon D a la durée de vie moyenne la plus longue à 666 nm et que les échantillons E et F ont la durée de vie similaire la plus longue à 408 nm et 543 nm. Ce résultat est en accord avec l'analyse de l'intensité d'émission. Les rendements quantiques internes de l'échantillon E recuit sont de 0.13 % à 543 nm et de 0.09 % à 666 nm.

3.3 $K_{0.3}Bi_{0.7}F_{2.4}:10\%Yb/5\%Er$

Dans ce chapitre, les nanoparticules $K_{0.3}Bi_{0.7}F_{2.4}$ et les nanoparticules $K_{0.3}Bi_{0.7}F_{2.4}$ co-dopées Yb/Er ont été synthétisées avec succès à température ambiante par une méthode de coprécipitation avec différents rapports d'addition initiale K/Bi/F. Les échantillons préparés sont en bon accord avec $K_{0.3}Bi_{0.7}F_{2.4}$ cubique décrit dans la littérature. La taille moyenne des cristallites calculée à partir des diagrammes de diffraction X et la taille moyenne statistique des nanoparticules obtenues par TEM ont été comparées et analysées.

Les échantillons préparés montrent des pics d'émission caractéristiques des UCNs co-dopés Yb/Er. Le rendement quantique interne de l'échantillon C est de 0.21 % à 543 nm et de 0.28 % à 666 nm. En particulier, l'échantillon C recuit présente d'excellentes durées de vie à 408 nm, 543 nm et 666 nm. Cette nouvelle matrice, avec une intensité d'émission élevée, des durées de vie de luminescence souhaitables et un QY interne, constitue un candidat de matrices hôtes pour les nanoparticules à conversion ascendante. Elle a des applications potentielles dans de nombreux

domaines.

3.4 BaYF₅:20%Yb/2%Er revêtu de BaYF₅

Au chapitre 3.4, les UCN BaYF₅:Yb/Er et les UCN BaYF₅:Yb/Er@BaYF₅ ont été préparés avec succès par synthèse solvothermale. Les échantillons préparés correspondent bien à BaYF₅ de forme cubique. La taille des cristallites et les paramètres de maille ont été calculés à partir des diagrammes de rayons X. Les spectres de fluorescence des UCNs BaYF₅:Yb/Er et des UCNs BaYF₅:Yb/Er@BaYF₅ ont été mesurés. Ils montrent tous les pics d'émission caractéristiques des UCNs co-dopés Yb/Er. L'intensité d'émission de BaYF₅:Yb/Er@BaYF₅ est plus forte que celle de BaYF₅:Yb/Er. Les durées de vie sont améliorées par le revêtement constitué de BaYF₅ non dopé. La durée de vie est passée de 23 μs à 30 μs à 543 nm. A 666 nm, la durée de vie est passée de 44 μs à 70 μs.

Chapitre 4 Perspective des UCNs

Le rendement quantique est le principal problème qui limite les applications des UCNs. Pour un UCN donné, le QY interne a une forte relation avec la taille des nanoparticules. Par exemple, le QY des matériaux microcristallins pour la conversion ascendante est 100 fois plus fort que celui des UCNs de même composition. De plus, les mesures du rendement quantique interne absolu sont difficilement comparables. En particulier pour les poudres, les mesures par la sphère d'intégration ont des limites pour un QY aussi faible. Les mesures par sphère intégrante ont une précision de $\pm 2\%$.²⁵ Cependant, le QY interne des UCNs les plus usuels excités par le rayonnement à 980 nm d'un laser est inférieur à 0.3 % dans la raie d'émission verte. Il faut aussi tenir compte de la seconde absorption provenant de la diffusion de la paroi de la sphère pour les poudres. Sinon, même l'intensité de la lumière émise ne peut pas être comparée dans différents articles. Le seul paramètre qui peut être comparé est la durée de vie, qui est rarement rapportée. Actuellement, la plus grande application sur les UCN est la bio-imagerie, pour laquelle l'observation de l'émission de lumière visible à l'œil nu suffit. Il n'y a pas d'exigence stricte sur la durée de vie ou le QY interne. C'est une des principales applications des UCNs. Les applications nécessitant des valeurs précises d'intensité de fluorescence devront être étudiées ultérieurement.

Les UCNs les plus efficaces sont β -NaYF₄ : 20% Yb³⁺, 2% Er³⁺ de structure cristalline hexagonale, qui a une meilleure performance que le NaYF₄ de forme cristalline cubique. Ces propriétés optiques dépendent de la structure cristalline peuvent être attribuées directement à des champs cristallins différents s'exerçant autour des ions lanthanides trivalents dans ces matrices. Les hôtes à faible symétrie exercent typiquement un champ cristallin contenant des composantes plus inégales autour des ions dopés par rapport aux homologues à symétrie élevée. Les

composantes inégales améliorent le couplage électronique entre les niveaux d'énergie 4f et la configuration électronique supérieure et augmentent par la suite les probabilités de transition f-f des ions dopants.

La structure cœur-coquille est également un bon moyen d'améliorer les propriétés de luminescence. Elle peut protéger le cœur de la particule contre les défauts de surface et les molécules adsorbées, qui se trouvent à la surface des nanoparticules. Le QY interne de l'échantillon constituée de nanoparticules $\beta\text{-NaYF}_4:20\% \text{Yb}^{3+}/2\% \text{Er}^{3+}$ de taille moyenne de 30 nm excitées par le rayonnement à 980 nm d'un laser est de 0.1 % à 540 nm. Le QY interne des UCN à structure cœur-coquille de nanoparticules $\beta\text{-NaYF}_4:20\% \text{Yb}^{3+}/2\% \text{Er}^{3+}/\beta\text{-NaYF}_4$ excitées par le rayonnement à 980 nm d'un laser est de 0.3 % à 540 nm.²⁶

Bibliographie

1. S. Wen, J. Zhou, K. Zheng, A. Bednarkiewicz, X. Liu, and D. Jin. Advances in highly doped upconversion nanoparticles. *Nat. Commun.*, **09**, 2415 (2018).
2. A. Noculak and A. Podhorodecki. Size and shape effects in β -NaGdF₄:Yb³⁺, Er³⁺ nanocrystals. *Nanotechnology*, **28**, 17 (2017).
3. A. R. Miandashti, M. E. Kordesch, and H. H. Richardson. Effect of temperature and gold nanoparticle interaction on the lifetime and luminescence of NaYF₄:Yb³⁺:Er³⁺ upconverting nanoparticles. *ACS Photonics*, **04**, 1864–1869 (2017).
4. S. Yamini, P. Priya, S. Priya, M. Gunaseelan, and J. Senthilselvan. Structural phase transformations in KYF₄:Er³⁺ nanoparticles synthesized by hydrothermal method for upconversion applications. *AIP Conf. Proc.*, **1832**, 3–6 (2017).
5. R. An, P. Lei, P. Zhang, X. Xu, J. Feng, and H. Zhang. Near-infrared optical and X-ray computed tomography dual-modal imaging probe based on novel lanthanide-doped K_{0.3}Bi_{0.7}F_{2.4} upconversion nanoparticles. *Nanoscale*, **10**, 1394–1402 (2018).
6. W. Feng, C. Han, and F. Li. Upconversion-nanophosphor-based functional nanocomposites. *Adv. Mater.*, **25**, 5287–5303 (2013).
7. A. Bagheri, H. Arandiyani, C. Boyer, and M. Lim. Lanthanide-doped upconversion nanoparticles: emerging intelligent light-activated drug delivery systems. *Adv. Sci.*, **03**, 1500437 (2016).
8. F. E. Auzel. Materials and devices using double-pumped phosphors with energy transfer. *Proc. IEEE*, **61**, 758–786 (1973).
9. X. Huang, S. Han, W. Huang, and X. Liu. Enhancing solar cell efficiency: the search for luminescent materials as spectral converters. *Chem. Soc. Rev.*, **42**, 173–201 (2013).

10. Z. Gu, L. Yan, G. Tian, S. Li, Z. Chai, and Y. Zhao. Recent advances in design and fabrication of upconversion nanoparticles and their safe theranostic applications. *Adv. Mater.*, **25**, 3758–3779 (2013).
11. M. Haase and H. Sch äfer. Upconverting nanoparticles. *Angew. Chem. Int. Ed.*, **50**, 5808–5829 (2011).
12. F. Auzel. Upconversion and anti-Stokes processes with f and d ions in solids. *Chem. Rev.*, **104**, 139–173 (2004).
13. F. Auzel. Upconversion processes in coupled ion systems. *J. Lumin.*, **45**, 341–345 (1990).
14. Y. Wang, S. Gai, N. Niu, F. He, and P. Yang. Synthesis of NaYF₄ microcrystals with different morphologies and enhanced up-conversion luminescence properties. *Phys. Chem. Chem. Phys.*, **15**, 16795–16805 (2013).
15. A. C. Yanes, A. Santana-Alonso, J. Mendez-Ramos, and J. del-Castillo. Structure and intense UV up-conversion emissions in RE³⁺-doped sol-gel glass-ceramics containing KYF₄ nanocrystals. *Appl. Phys. B Lasers Opt.*, **113**, 589–596 (2013).
16. S. Mishra, S. Daniele, G. Ledoux, E. Jeanneau, and M. F. Joubert. Heterometallic Na-Y(Ln) trifluoroacetate diglyme complexes as novel single-source precursors for upconverting NaYF₄ nanocrystals co-doped with Yb and Er/Tm ions. *Chem. Commun.*, **46**, 3756–3758 (2010).
17. P. Lei, R. An, S. Yao, Q. Wang, L. Dong, X. Xu, K. Du, J. Feng, and H. Zhang. Ultrafast synthesis of novel hexagonal phase NaBiF₄ upconversion nanoparticles at room temperature. *Adv. Mater.*, **29**, 1700505 (2017).
18. G. Liu and B. Jacquier. Spectroscopic properties of rare earths in optical materials. *Materials Science*, **83**, 266-268 (2005).

19. N. Bloembergen. Solid state infrared quantum counters. *Phys. Rev. Lett.*, **02**, 84–85 (1959).
20. K. Biswas, A. D. Sontakke, J. Ghosh, and K. Annapurna. Enhanced blue emission from transparent oxyfluoride glass-ceramics containing $\text{Pr}^{3+}:\text{BaF}_2$ nanocrystals. *J. Am. Ceram. Soc.*, **93**, 1010–1017 (2010).
21. X. Su, X. Sun, S. Wu, and S. Zhang. Manipulating the emission intensity and lifetime of $\text{NaYF}_4:\text{Yb}^{3+},\text{Er}^{3+}$ simultaneously by embedding it into CdS photonic crystals. *Nanoscale*, **09**, 7666–7673 (2017).
22. L. Liang, Y. Liu, C. Bu, K. Guo, W. Sun, N. Huang, T. Peng, B. Sebo, M. Pan, W. Liu, S. Guo, and X. Z. Zhao. Highly uniform, bifunctional core/double-shell-structured $\beta\text{-NaYF}_4:\text{Er}^{3+},\text{Yb}^{3+}@\text{SiO}_2@\text{TiO}_2$ hexagonal sub-micropisms for high-performance dye sensitized solar cells. *Adv. Mater.*, **25**, 2174–2180 (2013).
23. J. C. Goldschmidt and S. Fischer. Upconversion for photovoltaics—a review of materials, devices and concepts for performance enhancement. *Adv. Opt. Mater.*, **3**, 510–535 (2015).
24. Y. T. Prabhu, K. V. Rao, V. S. S. Kumar, and B. S. Kumari. X-Ray analysis by Williamson-hall and size-strain plot methods of ZnO nanoparticles with fuel variation. *World J. Nano Sci. Eng.*, **04**, 21–28 (2014).
25. J. C. de Mello, H. F. Wittmann, and R. H. Friend. An improved experimental determination of external photoluminescence quantum efficiency. *Adv. Mater.*, **09**, 230–232 (1997)
26. J.-C. Boyer and F. C. J. M. van Veggel. Absolute quantum yield measurements of colloidal $\text{NaYF}_4:\text{Er}^{3+},\text{Yb}^{3+}$ upconverting nanoparticles. *Nanoscale*, **02**, 1417–1419 (2017)

RÉSUMÉ

L'up-conversion est un procédé d'émission de type anti-Stokes. Le premier objectif de cette thèse est de synthétiser et de caractériser de nouveaux UCNs à base de fluorure codopés avec des paires Yb/Er pour réaliser la conversion du proche infrarouge en lumière visible. La seconde est de choisir quelques UCNs optimaux des composés préparés, qui devraient posséder une forte émission, une longue durée de vie de luminescence, et un rendement quantique élevé de conversion vers le haut. La discussion spécifique sur les résultats des quatre séries d'UCN préparés, y compris KYF₄:Yb/Er, BiF₃:Yb/Er, K_{0.3}Bi_{0.7}F_{2.4}:Yb/Er, et BaYF₅:Yb/Er@BaYF₅, est présentée. La structure de la phase nanocristalline, la taille moyenne calculée des cristallites, la morphologie, la distribution de la taille des nanoparticules, les spectres d'absorption, le rendement quantique interne, les spectres d'émission et les temps de décroissance ont été analysés et examinés.

MOTS CLÉS

synthèse et caractérisation, nouvelles nanoparticules à base de fluorure, propriété de photoluminescence

ABSTRACT

Up-conversion is an anti-Stokes type emission process where the doped activators ions absorb two or more photons from a low energy source to emit a high energy light. The first aim of this thesis is to synthesize and characterize some novel fluoride-based UCNs co-doped with Yb/Er pairs to realize the near-infrared to visible light conversion. The second is to pick some optimal UCNs from the prepared compounds, which should possess strong emission, long luminescence lifetime, and high up-conversion quantum yield. The specific discussion on the results of the four series of the prepared UCNs, including KYF₄:Yb/Er, BiF₃:Yb/Er, K_{0.3}Bi_{0.7}F_{2.4}:Yb/Er, and BaYF₅:Yb/Er@BaYF₅, was presented. The nanocrystal phase structure, calculated average crystallite size, morphology, nanoparticle size distribution, absorption spectra, internal quantum yield, emission spectra, and the decay times were analyzed and discussed.

KEYWORDS

synthesis and characterization, novel fluoride based nanoparticles, photoluminescence property